UNIVERSITY OF CALIFORNIA
RIVERSIDE

Control and Modeling of Imbibition in Paper-Based Microfluidic Devices

A Dissertation submitted in partial satisfaction
of the requirements for the degree of

Doctor of Philosophy

in

Bioengineering

by

Sidharth Modha

March 2022

Dissertation Committee:
Dr. Hideaki Tsutsui, Chairperson
Dr. Bhargav Rallabandi
Dr. Ashok Mulchandani

The Dissertation of Sidharth Modha is approved:

Committee Chairperson

University of California, Riverside

ACKNOWLEDGMENTS

I would like to acknowledge my advisor, Dr. Hideaki Tsutsui for his support, mentorship, and teaching throughout my graduate career. Thank you for the encouragement and patience during the numerous failures and successes experienced during my graduate school tenure. I also extend my gratitude to my committee members Dr. Bhargav Rallabandi and Dr. Ashok Mulchandani for their guidance throughout my Ph.D.

I would like to thank all my colleagues that I worked with in the Regenerative Microengineering Laboratory, including Dr. Daniel Nampe, Dr. Carlos Castro, Dr. Brent Kalish, Carys Layton, Jenna Roper, Chia-Wei Liu, and Jianho Zhang for their mentorship and friendship developed over the years. Special thanks to my undergraduate student Hussein Chamouni for his hard work and persistence.

I would also like to thank Dr. Robert McKee for making my teaching experience at UCR a thoroughly enjoyable one.

I would like to thank the National Science Foundation under Grant No. CBET-1601681 for their financial support during my tenure at UCR.

I would like to thank my parents for their love and support throughout my life and especially during my graduate school career.

Finally, I would like to acknowledge the inclusion of previously published material in this dissertation from the following sources:

Modha, S., Shen, Y., Chamouni, H., Mulchandani, A., Tsutsui, H., 2021. Biosensors and Bioelectronics 180, 113090

The above source was adapted in its entirety (without being rewritten) in Chapter 2 and in Appendices A-G.

Modha, S., Castro, C., Tsutsui, H., 2021. Biosensors and Bioelectronics 178, 113026.

The above source was adapted in its entirety (without being rewritten) in Chapter 1 and in Chapter 3.2-3.3

DEDICATION

To my parents

ABSTRACT OF THE DISSERTATION

Control and Modeling of Imbibition
in Paper-Based Microfluidic Devices

by

Sidharth Modha

Doctor of Philosophy, Graduate Program in Bioengineering
University of California, Riverside, March 2022
Dr. Hideaki Tsutsui, Chairperson

Access to medical care is a significant challenge facing developing countries. The World Health Organization developed the ASSURED criteria, which specifies requirements for the ideal diagnostic. ASSURED stands for Affordable, Sensitive, Specific, Rapid/Robust, Equipment-free and Deliverable. Traditional microfluidic diagnostics (comprised of glass/PDMS) require expensive fabrication procedures and user-intervention to manipulate fluids on the device. For those reasons, paper shows great promise as a substrate for an ASSURED microfluidic diagnostic. It is affordable and does not require external pumping to move fluids. Initially, microfluidic paper-based analytical devices (μPADs) performed simple, colorimetric assays. However, the field has evolved rapidly. Modern μPADs have been developed for a plethora of applications such as nucleic acid amplification.

Wider adaptation of μPADs relies on the incorporation of more complicated assays (i.e. involving multiple fluids), which would allow μPADs to replace more expensive benchtop equipment. This requires more robust fluid control. Typically, fluid control on μPADs has been achieved by slowing fluid down to create delays between

different channels. However, adding delays increases overall assay time and creates other complications such as fluid loss due to evaporation. Instead, creating ‘delays’ by accelerating wicking (relative to native paper) is being investigated. Previous approaches include sandwiching the paper between polymer films or creating ‘macro capillaries’ within the paper for the liquid to flow through. Of particular interest is the etching of grooves onto paper channels using either a plotter or a CO2 laser. These grooves create hollow regions in the paper which lead to faster wicking speeds. This study aims to characterize the behavior of grooved channels in paper and assess their performance as ‘delay’ mechanisms for a multi-fluid paper-based sensor.

Typically, μPAD designs evolve in a trial-and-error basis, where devices are fabricated, tested and updated. Having accurate models that characterize the imbibition process could streamline development by allowing direct translation of *in-silico* designs to fully-functioning paper-based tools. Current imbibition models do not adequately describe the complex transport phenomena occurring within the paper matrix. This study also aims to develop an *in-silico* simulation that can reliably predict imbibition in both native paper and grooved channels.

TABLE OF CONTENTS

LIST OF FIGURES

LIST OF TABLES

LIST OF SYMBOLS

A cross-sectional area (m^2)
A_p total pore area (m^2)
B inertial resistance factor (m^{-1})
b fitted absorbance coefficient
C/C_1 geometry constant
C_a capillary number
c_g gas molar concentration (mol/m^3)
c_l liquid molar concentration (mol/m^3)
d fiber diameter (m)
D static pore diameter (m)
D_e effective pore diameter (m)
D_f fractal dimension for pore size distribution
D_h hydrodynamic diameter (m)
D_T tortuosity fractal factor
D_{va} diffusion coef. of vapor in air (m^2/s)
g accel. due to gravity (m/s^2)
G geometry factor
h distanced wicked by the liquid front (m)
h_r capillary-rise height (m)
H height of porous medium (m)
j molar evaporative flux ($mol/(m^2 \cdot s)$)
K permeability (m^2)
L capillary length (m)
$\dot{m}_e$ evaporation rate ($kg/m^2 \cdot s$)
P pressure (Pa)
P_c capillary pressure (Pa)
Q volumetric flow rate (m^3/s)
R pore radius (m)
t time (s)
t_g half-gap height (m)
t_h substrate thickness (m)
u velocity (m/s)
v average liquid velocity (m/s)
W width of substrate (m)
X_a mole frac. of gas at top of porous medium
X_i mole frac. of gas at the liquid-air interface
β fitting constant (rate of constriction)
γ surface tension (N/m)
ϵ const. function of substrate geometry
Θ saturation
θ contact angle (deg)
θ_d dynamic contact angle (deg)
θ_s static contact angle (deg)
θ_w volumetric water content
μ dynamic viscosity ($Pa \cdot s$)
ρ density (kg/m^3)

τ tortuosity
ϕ porosity of the medium
ϕ_c critical value of porosity (percolation threshold)
Ψ pressure head (m)

1. FLUID-CONTROL IN PAPER DEVICES: AN OVERVIEW

1.1. Introduction

A significant challenge facing the world is the continuous improvement of global health, which includes factors such as disease diagnosis and detection, adequate food safety and regulation of environmental pollution. Improvements in global health are necessary to drive continued economic growth and prosperity, especially in developing nations. Microfluidic devices show great promise as a platform for affordable diagnostics. These devices are capable of handling microliter sample volumes with high precision. This allows laboratory-grade analysis at a much lower cost compared to traditional laboratory methods. Historically, these devices were made from glass or silicon. However, more modern devices utilize polydimethylsiloxane (PDMS) and other polymers. Such microfluidic devices have been developed for myriad uses, such as immunosensing and filtration of biological fluids on chip (Chiem and Harrison 1998; Kim and Park 2005; Yung et al. 2009; Li et al. 2014). More advanced devices are capable of polymerase chain reaction (PCR) through built-in heating elements and chromatographic separations (Malmstadt et al. 2003; Lazar et al. 2006; Zhang et al. 2007; Tachibana et al. 2015). While these devices are effective, they require an external pump to drive fluids as well as properly trained personnel.

The World Health Organization developed a series of requirements for the ideal diagnostic. Known as the ASSURED criteria, it states that a diagnostic device should be Affordable, Sensitive, Specific, Rapid/Robust, Equipment-free and Deliverable (Kettler et al. 2004). In the last 10 years, there has been renewed interest in paper as a substrate for

an ASSURED diagnostic. Paper has several desirable properties such as high affinity for water, swelling during liquid uptake, biocompatibility, and biodegradability. Paper-based devices can utilize paper's inherent wicking ability to drive fluid flow, thus eliminating the need for external pumping. Fabricating paper devices is also more simple compared to traditional microfluidic devices, as channels can be formed easily by selectively removing sections of the paper using high-precision CO_2 laser-cutting (Fu et al. 2010; Chitnis et al. 2011) or craft cutting (Fenton et al. 2009) . Alternatively, channel boundaries can be created by patterning a hydrophobic material. This can be achieved via photolithography (Martinez et al. 2008) or even using commercially available inkjet printers (Abe et al. 2010) or solid-ink printers (Carrilho et al. 2009). The use of paper as a diagnostic tool was first reported in the early 1900s (Dieterich 1902; Yetisen et al. 2013). However, the introduction of the lateral flow assay (LFA) in the 1950s paved the way for modern paper-based diagnostics (Yetisen et al. 2013). Originally used for home-pregnancy tests, modern LFAs are used for numerous applications such as the detection of viral/bacterial nucleic acids and other biomarkers from human samples (Fu et al. 2016; Van Hooij et al. 2016; Wang et al. 2017; Zhang et al. 2018). In 2007, Martinez *et al.* developed the first microfluidic paper-based analytical device (μPAD) by patterning fluidic circuits on paper using lithographic techniques (Martinez et al. 2007). Since then, μPADs have been developed for a plethora of applications, such as disease detection in human samples, plants/crops and other food sources (Li and Steckl 2018).

Initially, μPADs were used for simple, colorimetric assays, such as detection of glucose or heavy-metal ions, which typically only require single fluid types (sample)

spotted or wicked onto the paper (Dungchai et al. 2010; Hossain and Brennan 2011; Ratnarathorn et al. 2012). However, recent developments in paper-based devices have seen the adaptation of more complicated, multi-step procedures (Park and Park 2017; Verma et al. 2018). Several recently published articles provide additional review of the paper-microfluidics field (Lim et al. 2019; Kim et al. 2020; Ozer et al. 2020). To accommodate these more complicated assays, μPADs must control multiple fluids in an automated fashion. That is, the user should not have to manually add fluids at specific intervals.

In this section, recent flow-control strategies that have been used in paper devices are discussed, including a brief summary of companies that are commercializing paper-based devices and the challenges they face. Control strategies are classified by mechanism of action. Despite limited theoretical understanding of flow behavior in paper, researchers have developed a plethora of different fluid-control strategies for paper-based devices using experimental techniques. These controls range from different methods to regulate flow in paper to novel techniques for creating hydrophobic boundaries within the paper. These methods can be classified into geometric, mechanical, chemical electrical, magnetic and thermal control techniques. This chapter contains material adopted from one of our previous publications(Modha et al. 2021).

1.1.1. Geometric Flow Control

Geometric control strategies change the dimensions of the paper itself to achieve different wicking behaviors. The simplest geometric control is a distance-based delay, which uses different length channels to control wicking times (Fu et al. 2010; Fu et al. 2011) (Fig. 1.1a). Apilux *et al.* demonstrated a simple distance-delay for use in a lateral flow ELISA (Apilux et al. 2013). The group printed baffles on the paper to create a serpentine channel, which increases the wicking length for that channel and slows it down. A similar approach was used by Preechakasedkit *et al.* ,whereby wax printing was used to create serpentine channels that delayed flow in specific regions (Preechakasedkit et al. 2018) (Fig. 1.1b). Delays can also be generated by changing the paper shape to create flow patterns that deviate from Lucas-Washburn flow. Mendez *et al.* demonstrated quasi-linear flow profiles using different fan-shaped outlets on porous membranes (Mendez et al. 2010). Cummins *et al.* developed a detachable "hydraulic battery" that is connected to the outlet of a microfluidic channel that can pump fluid at precise flow rates. The pump facilitates step changes to pumping speeds as well as oscillating flows (Cummins et al. 2017). Another recent development is the use of kirigami and quilling to create different fluidic channels in paper (Fig. 1.1c). Kirigami involves cutting and folding paper to create unique shapes and structures. Quilling involves rolling and gluing paper together to create different designs. Gao *et al.* used these techniques to create paper devices from rolled strips of paper (Gao et al. 2017). Each paper channel was sandwiched between two layers of hydrophobic tape, which was then folded onto itself and rolled about a central pivot. This was repeated with several strips of paper to create a set of tightly wound but independent channels.

However, these techniques are limited by the footprint of the device. Other efforts include adding dissolvable barriers onto the paper, providing additional wicking material (known as a shunt) that the fluid must pass through, and reducing the available wicking area through geometry changes (Toley et al. 2013; Shin et al. 2014). Park *et al.* engineered delay in a vertical flow device by pressing the paper region with a load cell (Park and Park 2017) (Fig. 1.1d). Compressing the fibers reduces the cross-sectional area available for wicking and slows down fluid. Delays up to 180 seconds were achieved using different amounts of pressure.

While effective, delay mechanisms can increase overall assay time. Furthermore, slowing down flow can exacerbate other issues, such as fluid loss to evaporation or reduced mixing between reagents. Native paper is a slow wicking material, due to the complex network of pores that create a highly tortuous path for fluid to follow (Elizalde et al. 2015; Castro et al. 2017). Efforts to accelerate flow in paper channels have generally involved driving fluid outside of the paper where it can flow more quickly. These include sandwiching the paper between polymer films (Jahanshahi-Anbuhi et al. 2014; da Silva et al. 2015). The gap between the film and the paper acts as a capillary, allowing fluid to flow in-between the film and the paper rather than inside the paper. Additionally, other groups created two-ply channels (Fig. 1.1e) (Camplisson et al. 2015; Channon et al. 2018) in paper by sandwiching two paper strips between a hollow layer of double-sided tape. The hollow region in the center of the channel has a much lower flow resistance compared to the paper around it. Other groups created faster-wicking channels by removing regions of the paper to create ‘macro capillaries’ for the liquid to flow through. (Renault et al. 2013;

Giokas et al. 2014; Shin et al. 2016; Liu et al. 2017b) (Fig. 1.1f). Of interest is the work of Giokas *et al.* and Liu *et al.*, who etched grooves into paper channels to speed up flow. Giokas *et al.* used a craft-plotter to carve channels into paper, while Liu *et al.* used a CO_2 laser cutter to achieve the same effect. The grooves allow fluid to bypass the paper and flow more quickly. Sealing the channels with tape further improves wicking speeds. Kalish et al. used a CO_2 laser to etch the surfaces of paper channels, increasing the effective diameter, thereby the wicking speed (Kalish et al. 2020).

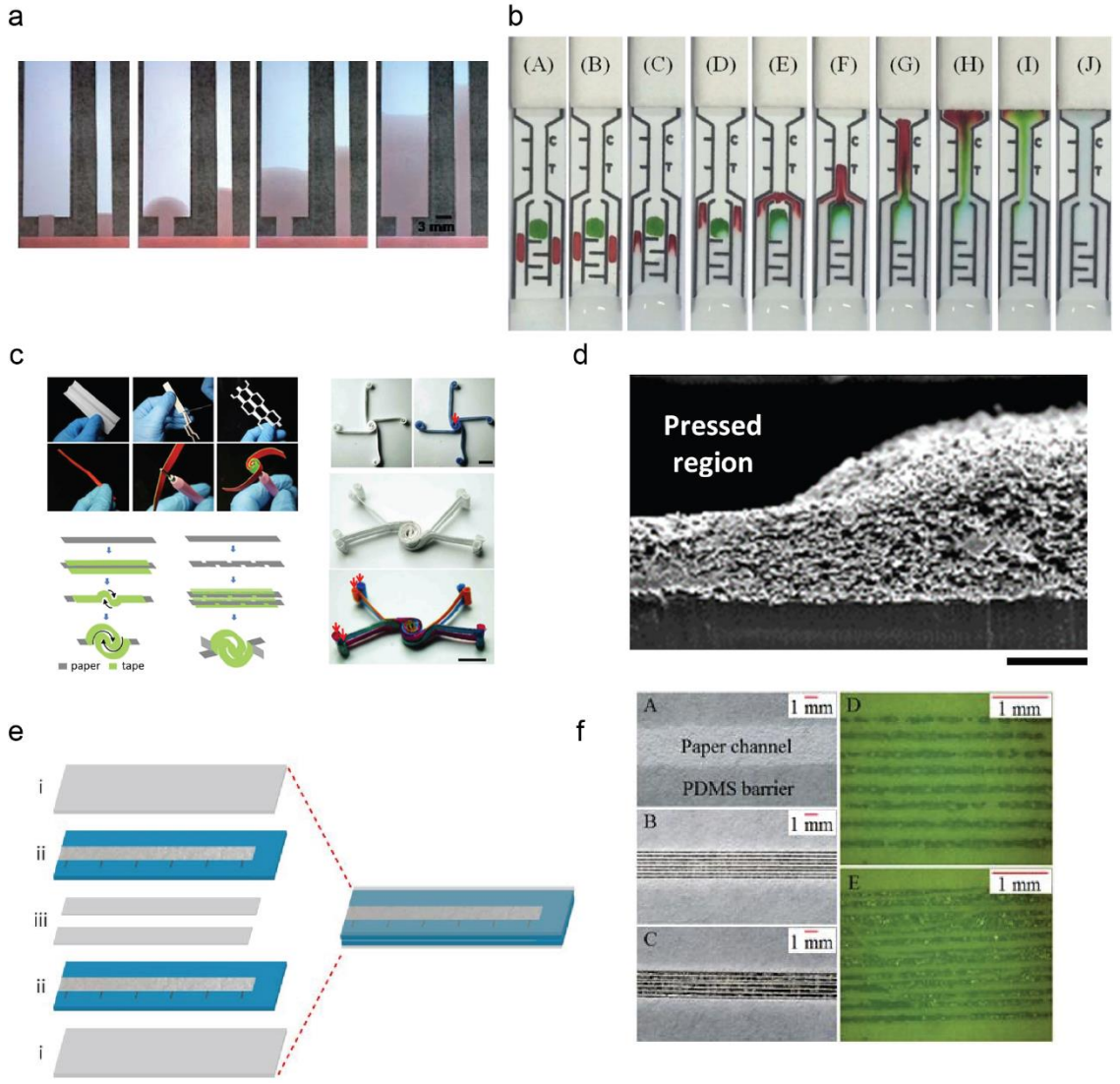

Fig. 1.1 Geometric flow control methods in paper-based analytical devices. (a) Manipulating flow rate by varying the width of the paper channel. Adapted from (Fu et al. 2010) with permission from The Royal Society of Chemistry. (b) Creating serpentine channels using wax printing for distance-based delays. Adapted from (Preechakasedkit et al. 2018) with permission from Elsevier. (c) Creating individual paper channels using kirigami and quilling. Each channel is separated with a layer of hydrophobic tape. Adapted from (Gao et al. 2017). (d) Delays generated in paper channels by compressing specific regions of the paper, reducing cross-sectional area. Adapted from (Park et al. 2016). (e) Rapid-flow paper channels created by sandwiching double-sided tape between two paper layers. Adapted from (Channon et al. 2018) with permission from The Royal Society of Chemistry. (f) Etching grooves in paper using a CO_2 laser to create rapid-flow channels. Adapted from (Liu et al. 2017b) with permission from Elsevier.

1.1.2. Mechanical Flow Control

Mechanical flow control involves physical manipulation of specific regions of a μPAD in order to move fluids. Mechanical control can act either as a switch (turning flow on/off) or as a valve (diverting fluid between different fluidic circuits). Toley *et al.* were among the first to develop mechanically actuated switches using the principle of swelling (Toley et al. 2015). A metering pad placed under a channel swelled as fluid imbibed into it. This swelling pushed the channel above it into contact with another channel, allowing flow between the two. Kong *et al.* used a similar technique (Kong et al. 2017) (Fig. 1.2a). A strip of chromatography paper placed underneath a channel would actuate during imbibition, pushing the channel above to open or close a fluidic circuit. The group demonstrated response times within 2 seconds using only 4 μL of fluid.

An alternative to swelling-based actuation is manually actuating the device by hand. Verma *et al.* developed a novel 'sliding strip' paper device for colorimetric ELISA. The device consists of multiple layers of wax-printed paper stacked together (Verma et al. 2018) (Fig. 1.2b). The third layer contains several inlets, each spotted with different reagents. The layer below ('docking layer') is what moves around. This layer contains the Control and Tests zones for the experiment. As liquid is added to each inlet in the top layer, the docking layer is moved downwards, introducing different reagents into the reaction zones. Therefore, the user would add liquid, slide the docking layer down and repeat the process for all the inlets. Han *et al.* developed a simple device for colorimetric detection of metal ions (Han et al. 2018). The device resembled a binder with a square paper base and several strips attached to it using plastic binding splines (Fig. 1.2c). When folded onto

the base, the strips act as bridges between regions on the base, allowing fluid to pass from one region to another. A similar design was implemented by Li *et al.* A hollow rivet was used to fix two strips of paper together, allowing them to pivot (Li et al. 2017a) (Fig. 1.2d). This allowed the user to rotate the paper strip as a bridge, connecting it to other regions of the paper. Sun *et al*. developed an electrochemiluminescence sensor comprised of three stacked circular disks of paper. Connections between layers are established by rotating each disk so that their hydrophilic zones are vertically aligned (Sun et al. 2018) (Fig. 1.2e). Wang *et al.* developed a 'pop-up' hydroxybutyrate sensor that is compatible with a blood glucose sensor. After adding a sample, the device is folded, bringing the sample inlet into contact with the sensor array (Wang et al. 2016) (Fig. 1.2f). Chou *et al.* implemented a three-layer origami device to create a paper-based ion preconcentrator (Chou et al. 2017). Folding the device connects the channels in all three layers. Kalish *et al.* demonstrated adhesive patterning and origami to create complex, 3D fluid circuits on a single, wax-patterned paper layer (Kalish and Tsutsui 2014, 2016).

Mechanical control on μPADs can also be achieved using external devices. Kim *et al.* demonstrated a pressure-driven valve system using a linear solenoid (Kim et al. 2018). The solenoid pressed down on a region of paper, compressing the fibers and stopping flow. After the solenoid is raised, the pressed region regains original flow properties. Li *et al.* designed a 'sample-in, answer-out' sensor intended to be used with a pipette (Li et al. 2017c). The paper test strips are placed inside a micropipette tip. The pipette then aspirates the test solution, producing a colorimetric readout on the test strip.

An interesting development is the use of absorbable materials to drive flow in specific directions. Akyazi *et al.* demonstrated the use of negative passive pumps on paper using ionic hydrogels (Akyazi et al. 2017; Akyazi et al. 2018) (Fig. 1.2g). Hydrogels are deposited onto specific regions of the paper (at either end of a channel). The hydrogel will absorb fluid very quickly, driving fluid towards it. The hydrogels can swell up to 12x their original size. Only after the hydrogel is fully saturated will liquid flow in the opposite direction. Channels were fabricated using wax printing and ionogel was deposited into specific locations using a cyclic olefin copolymer/pressure sensitive adhesive (COP/PSA) gasket, then UV crosslinked. Hydrogels can reverse flow on paper even after the paper is completely saturated.

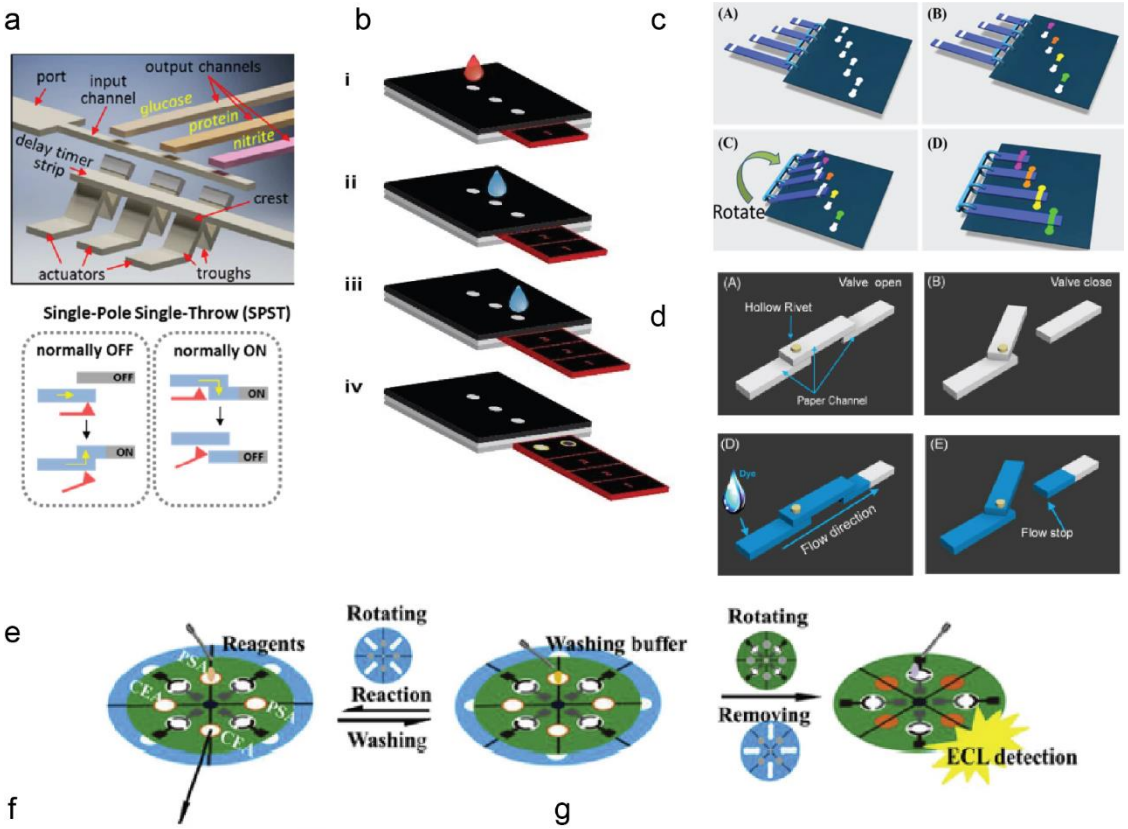
a
port
input channel
output channels
glucose
protein
nitrite
delay timer strip
crest
actuators
troughs
Single-Pole Single-Throw (SPST)
normally OFF
normally ON
OFF
ON
ON
OFF
b
i
ii
iii
iv
c
(A)
(B)
(C)
(D)
Rotate
d
(A) Valve open
Hollow Rivet
Paper Channel
(B) Valve close
(D)
Dye
Flow direction
(E)
Flow stop
e
Reagents
PSA
CEA
PSA
CEA
Rotating
Reaction
Washing
Washing buffer
Rotating
Removing
ECL detection
f
Glucometer
Blood Analytes
Pop-up Paper Based Device
g
hydrogel
FLOW direction

Fig. 1.2 Flow control in paper using mechanical approaches. (a) Paper-based valve system based on unfolding of paper actuator strips. Swelling of the actuator strips causes them to push different paper channels together, creating a fluidic circuit. Adapted from (Kong et al. 2017) with permission from The Royal Society of Chemistry. (b) ELISA test-strip. The user moves the test strip and adds water to hydrate reagents in each zone. Adapted from (Verma et al. 2018). (c) Valving system that uses paper layers secured to a binder spline. Fluidic connections are made by rotating different paper strips onto the main paper base. Adapted with permission from (Han et al. 2018). Copyright (2018) American Chemical Society. (d) Valve system based on physical movement of paper strips to block and allow fluid flow between different layers. Adapted with permission from (Li et al. 2017a). Copyright (2017) American Chemical Society. (e) 'Rotating disk' device where fluidic circuits are connected by rotating the top layer of the device. Adapted from (Sun et al. 2018) with permission from Elsevier. (f) 'Origami' style hydroxybutyrate sensor. After sample addition, the device is folded so that measurements can be taken. Adapted with permission from (Wang et al. 2016). Copyright (2016) American Chemical Society. (g) Directional imbibition achieved using ionic hydrogels. Adapted from (Akyazi et al. 2018) with permission from Elsevier.

1.1.3. Chemical Flow Control

Chemical control of fluids on paper involves adding chemicals/additives onto the paper that change its imbibition properties. These techniques have been used extensively to pattern hydrophobic materials onto paper, which is used to create fluidic circuits. Wax printing has been commonly used for this purpose. Wax is applied onto the surface of paper and melted. As it melts, the wax penetrates the thickness of the paper, creating a hydrophobic boundary (Carrilho et al. 2009; Renault et al. 2013). Typically, the wax is deposited onto the paper using a solid-ink wax printer (Lu et al. 2009; Nie et al. 2010; Jang and Song 2015). Most wax printers have been manufactured by Xerox. Unfortunately, the company discontinued their solid-ink printers several years ago. Therefore, as these printers phase out, it is important to explore alternative methods.

Other techniques such as screen-printing (Dungchai et al. 2011; Wang et al. 2012; Liu et al. 2015) and wax dipping have been demonstrated previously (Songjaroen et al. 2011). Chiang *et al.* developed a modified printer with a heating element to dispense and melt wax onto a paper substrate. This process allowed rapid fabrication of devices

within a few minutes (Chiang et al. 2019). A new area of interest is the ability to draw wax boundaries directly on paper without printing and heating. Li *et al.* developed a pen that is capable of depositing wax onto paper (Fig. 1.3a). A ball-point was modified to accept liquid wax ink. The pen also contained a built-in heating element to melt the wax. This allows the user to draw barriers onto paper with relative ease (Li et al. 2017d). To achieve higher throughput for batch fabrication, Liu *et al.* designed a custom roll printing machine that can print and melt wax patterns into paper (Liu et al. 2020).

Nargang *et al.* attempted to create flexible lithographic structures on paper (Nargang et al. 2018). They rendered Whatman 1 chromatography paper hydrophobic via optical exposure of a silane mixture soaked into the paper, successfully fabricating features down to 350μm. Hydrophobic barriers withstood 50+ folding cycles (Fig. 1.3b). Michael *et al.* utilized a similar procedure. They treated filter paper with BSA before irradiating it with UV for 3 minutes. This treatment rendered the paper hydrophobic and prevented non-specific binding without reducing its porosity (Fig. 1.3c). The degree of hydrophobicity could be adjusted based on the concentration of BSA used and UV exposure times (Michael et al. 2018).

An alternative to wax and lithographic techniques is chemical vapor deposition (CVD), which consists of introducing reactive chemicals onto a sample in the presence of a vacuum. The chemicals will react with the surface of the target material, altering its surface chemistry or create a film on the surface. Haller *et al.* were among the first to demonstrate this technique on paper. They patterned photoresponsive poly(o-nitrobenzyl methacrylate) (PoNBMA) onto chromatography paper to create hydrophobic channels

(Haller et al. 2011). Chen *et al.* used CVD to create lipophobic barriers in paper (Chen et al. 2013). These barriers allowed the use of organic solvents on paper, which was not possible with traditional wax barriers. Wang *et al.* created hydrophobic channels on paper through the deposition and subsequent etching of parylene-C (a polymer commercially used for moisture barriers). CVD was used to deposit parylene-C onto filter paper. The paper subsequently etched using a microplasma jet to create hydrophilic channels inside the paper (Wang et al. 2018b).

Plasma treatment has also been used to pattern paper. Dimitrakellis *et al.* used it to create 'super hydrophobic' paper by treating it with atmospheric helium-oxygen plasma followed by fluorocarbon deposition. This procedure achieved contact angles > 150° on regular printer paper without any noticeable degradation (Dimitrakellis et al. 2017). A similar technique was used by Li *et al.*, whereby paper was etched with oxygen plasma prior to treatment with fluoro-silanes (Li et al. 2017b). Navarro *et al.* created hydrophobic paper using fluorotrimethylsilane plasma treatment. The resulting paper achieved super hydrophobicity without drastically effecting its mechanical properties (Navarro et al. 2003). An interesting, alternative application of plasma treatment is the work of Zhao *et al.*, who showed that treating paper with oxygen plasma (~4 min) can allow proteins and antibodies to be immobilized directly onto the paper (Zhao et al. 2016).

More recent advances have created hydrophobic surfaces on paper through the aerosolized deposition of different chemicals on the surface. Pal *et al.* implemented omniphobic (resistant to polar/non-polar fluids) filter paper as part of a smart bandage for chronic wound monitoring. The device used pieces of Whatman 5 filter paper that were

sprayed with 2% fluorinated alkyltrichlorosilane in isopropyl alcohol. Conductive electrodes were then printed onto the paper and fixed to the underside of a bandage. The omniphobic electrodes were used for measuring pH and uric acid concentration at the wound site (Pal et al. 2018). Deng *et al.* used aerosol spray paint to create hydrophobic surfaces on paper by applying the paint through a mask (Deng et al. 2019). Liu *et al.* created hydrophobic surfaces on paper by spraying water repellant (Neverwet®) onto the paper through a mask (Liu et al. 2017a). Heist *et al.* used the aerosolized deposition of polycaprolactone to create hydrophobic regions in paper. This technique created completely hydrophobic barriers with widths below 280 μm and can also be used to create 3D fluid networks by stacking multiple pieces of paper (Heist et al. 2018). The most notable work is that of Koşak Söz *et al.*, who developed so-called 'Janus' hydrophobic paper, which is superhydrophobic on one face only, preserving wettability on the opposite face (Fig. 1.3d). This unique property was achieved by spin-coating a mixture of PDMS, glass and silica particles onto a piece of filter paper (Koşak Söz et al. 2018). After subsequent baking, the treated side became super hydrophobic (contact angle > 150°) while the opposite side was unaffected.

In addition to patterning, chemical methods have also been used to generate delays in paper channels. Noh and Phillips were among the first researchers in this field, depositing various amounts of paraffin wax on paper to create delays (Noh and Phillips 2010a, b). The delays were incorporated into 3-D vertical flow assays, where the paraffin wax could generate delays of several minutes. Weng *et al.* employed a similar technique, printing different amounts of solid-wax ink onto filter paper to slow down fluid flow (Weng

et al. 2014). Melting the wax caused it to flow into the paper matrix, blocking the pores inside and stopping fluid. Strong *et al.* also made use of wax barriers, but without the melting step (Strong et al. 2019). Covering a certain proportion of a paper channel with wax could generate variable delays (Fig. 1.3e). Additionally, Potter *et al.* noted the dependency of hydrophobicity on wax color (Potter et al. 2019). In a CMYK color system (Xerox solid ink), magenta wax was found to be the most hydrophobic and yellow the most hydrophilic. Wax barriers have also been demonstrated in LFAs to improve sensitivity by concentrating the sample at the detection zone (Rivas et al. 2014) (Fig. 1.3f). Schilling *et al.* used laser toner to seal paper-based devices, containing all added fluids inside the device (Schilling et al. 2012).

Chen *et al.* used deposition of surfactant onto paper to create fluidic diodes on wax-bound paper, achieving unidirectional flow (Chen et al. 2012). The surfactant reduces the surface tension of the fluid, allowing fluid to flow through the wax barrier in front of it. Other groups have used manual addition of surfactant to open a wax valve after a specific incubation time (Chen et al. 2019) (Fig. 1.3g). Lai *et al.* generated delays by spotting different concentration of tween-20 onto paper for ELISA. Delays of up to 160 seconds were generated (Lai et al. 2019). As an alternative to surfactant, Lutz *et al.* created flow delays by applying different concentrations of sugar into paper channels (Lutz et al. 2013). The sugar would block the pores of the paper until the fluid was able to dissolve it. Another valving mechanism was developed by Houghtaling *et al.* who used dissolvable sugar bridges within paper channels (Houghtaling et al. 2013). The bridge degrades after a specific volume of fluid travels across. Jahanshahi-Anbhuhi *et al.* used a similar eroding bridge comprised of water-soluble pullulan (Jahanshahi-Anbuhi et al. 2014).

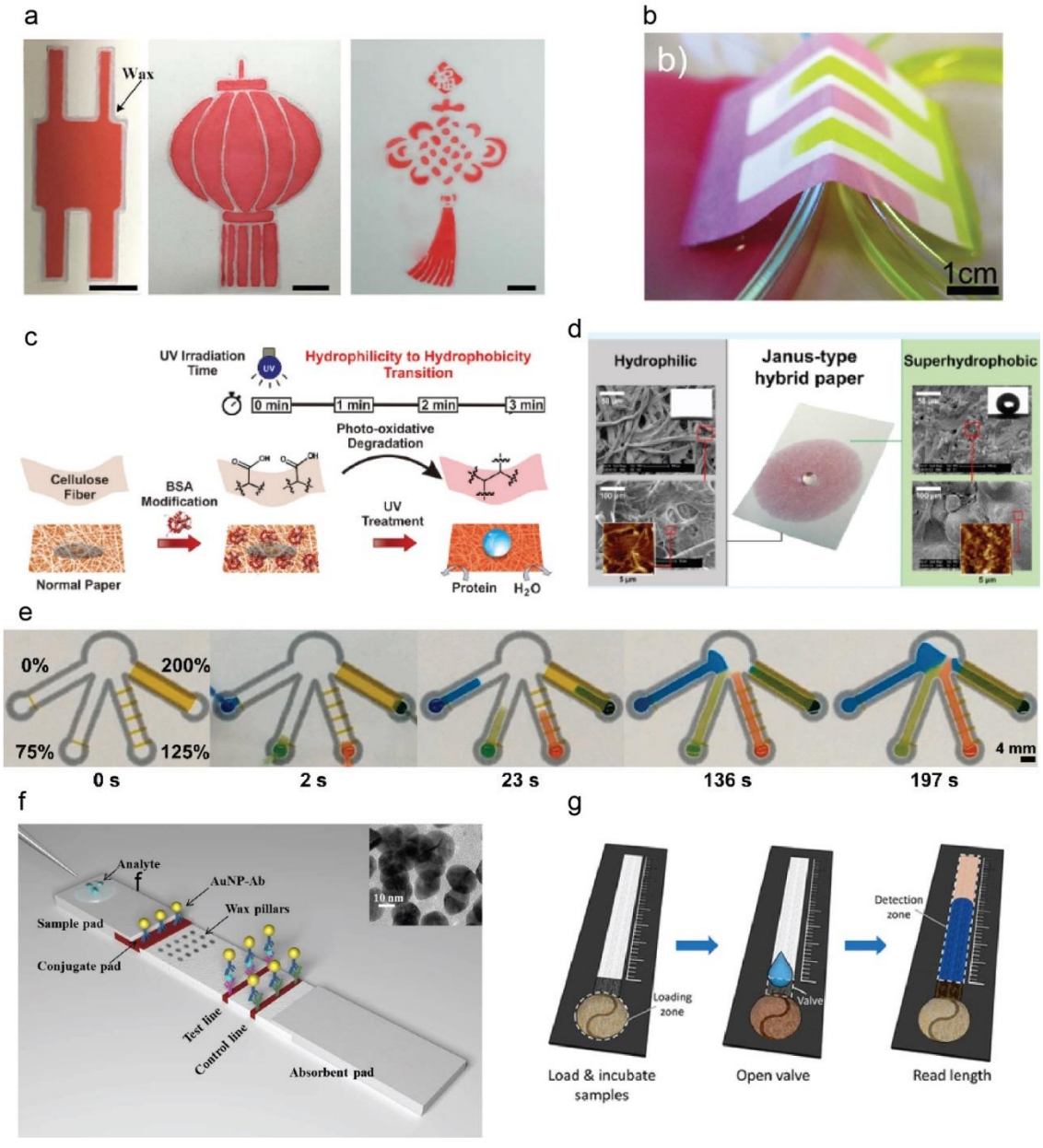
a
Wax
b
b)
1cm
c
UV Irradiation Time
Hydrophilicity to Hydrophobicity Transition
0 min
1 min
2 min
3 min
Photo-oxidative Degradation
Cellulose Fiber
BSA Modification
UV Treatment
Normal Paper
Protein
H_2O
d
Hydrophilic
Janus-type hybrid paper
Superhydrophobic
e
0%
200%
75%
125%
4 mm
0 s
2 s
23 s
136 s
197 s
f
Analyte
AuNP-Ab
Wax pillars
Sample pad
Conjugate pad
Test line
Control line
Absorbent pad
10 nm
g
Loading zone
Valve
Detection zone
Load & incubate samples
Open valve
Read length

Fig. 1.3 Flow control in paper using chemical approaches. (a) Specially modified ball-point pen that is capable of depositing wax onto paper to create hydrophobic boundaries. Adapted from (Li et al. 2017d) with permission from Elsevier. (b) Whatman 1 Chr rendered hydrophobic via optical exposure of a silane mixture soaked into the paper, but retaining its flexibility. Adapted from (Nargang et al. 2018) with permission from The Royal Society of Chemistry. (c) BSA was deposited on paper and UV-irradiated to create hydrophobic boundaries while preserving the porosity of the paper. Adapted with permission from (Michael et al. 2018). Copyright (2018) American Chemical Society. (d) 'Janus' type paper that is superhydrophobic on one side and hydrophilic on the other. Adapted with permission from (Koşak Söz et al. 2018). Copyright (2018) American Chemical Society. (e) Wax printed on the channel surface (without melting) acts as a delay. The greater amount of wax printed, the greater the delay. Adapted from (Strong et al. 2019). (f) The use of wax pillars on a LFA to improve sensitivity. Adapted from (Rivas et al. 2014) with permission from The Royal Society of Chemistry. (g) Deposition of surfactant allows fluid to bypass the wax boundary at the inlet. Adapted with permission from (Chen et al. 2019). Copyright (2019) American Chemical Society.

1.1.4. Electrical/Magnetic/Thermal Flow Control

Electrical flow control on paper typically deals with changing the surface tension of a liquid on the paper surface through the application of an electric potential. Ainla *et al.* developed electrical textile valves using a hydrophobic mesh (Ainla et al. 2017) (Fig. 1.4a). In the absence of an applied electric field, the mesh prevents passage of fluid through it. However, an applied potential disrupts this hydrophobicity and allows fluid to pass through. The authors also demonstrated that whole blood is also able to pass through. An orthogonal approach was taken by Wang *et al.*. The authors developed an electromagnetic valve to actuate a specific region of their device (Wang et al. 2018a). The timing circuit is printed on either side of a paper channel. When dry, the circuit is incomplete and there is no actuation (Fig. 1.4b). However, when fluid reaches the region with the electrodes, the circuit is complete, and the device actuates. A recent study utilized electro-osmotic pumping to accelerate flow on paper. Rosenfeld *et al.* demonstrated that applying a potential on either side of a channel can cause fluid to wick towards a specific side (Rosenfeld and Bercovici 2019). The applied potential can be varied to control the rate

of wicking (Fig. 1.4c). Koo *et al.* designed electrowetting valves on a paper-based device using hydrophobic and hydrophilic conductive electrodes (Koo et al. 2013). The sample is blocked by the hydrophobic electrode. Applying a potential across the electrode renders it hydrophilic and allows the fluid to pass it (Fig. 1.4d). Atabaksh *et al.* demonstrated actuation and confinement of water droplets on a sequence of screen-printed resistors (Atabakhsh and Ashtiani 2018) Sequentially applying a potential on each resistor drives the droplet horizontally across the surface of the device. This device uses lower driving potentials compared to other electrowetting techniques (mesh with hydrophobic coating). The applied voltage can be used to control droplet velocity.

Flow control can also be indirectly used through magnetic or thermal actuation on paper. Fratzl *et al.* developed a magnet-driven valve system. neodymium (NdFeB) powder was impregnated onto paper to create magnetic valves (Fig. 1.4e). The powder was deposited onto paper such that it does not interact with fluids flowing through the paper (Fratzl et al. 2018). Applying a magnetic field causes the channel to contact another, creating a flow path. Philips *et al.* developed thermally actuated wax valves by placing a printed heating element under a lateral-flow strip with a printed wax boundary (Fig. 1.4f). Turning the heating element on melts the wax and allows fluid to flow past it (Phillips et al. 2016). Following from Philips *et al.*, Atabakhsh *et al.* also developed a microfluidic device that utilizes melting wax barriers (Atabakhsh and Ashtiani 2019). The wax boundaries across each channel have a heating element printed directly underneath them. Under an applied DC voltage, the heating element can melt the wax barrier and allow fluid into that zone.

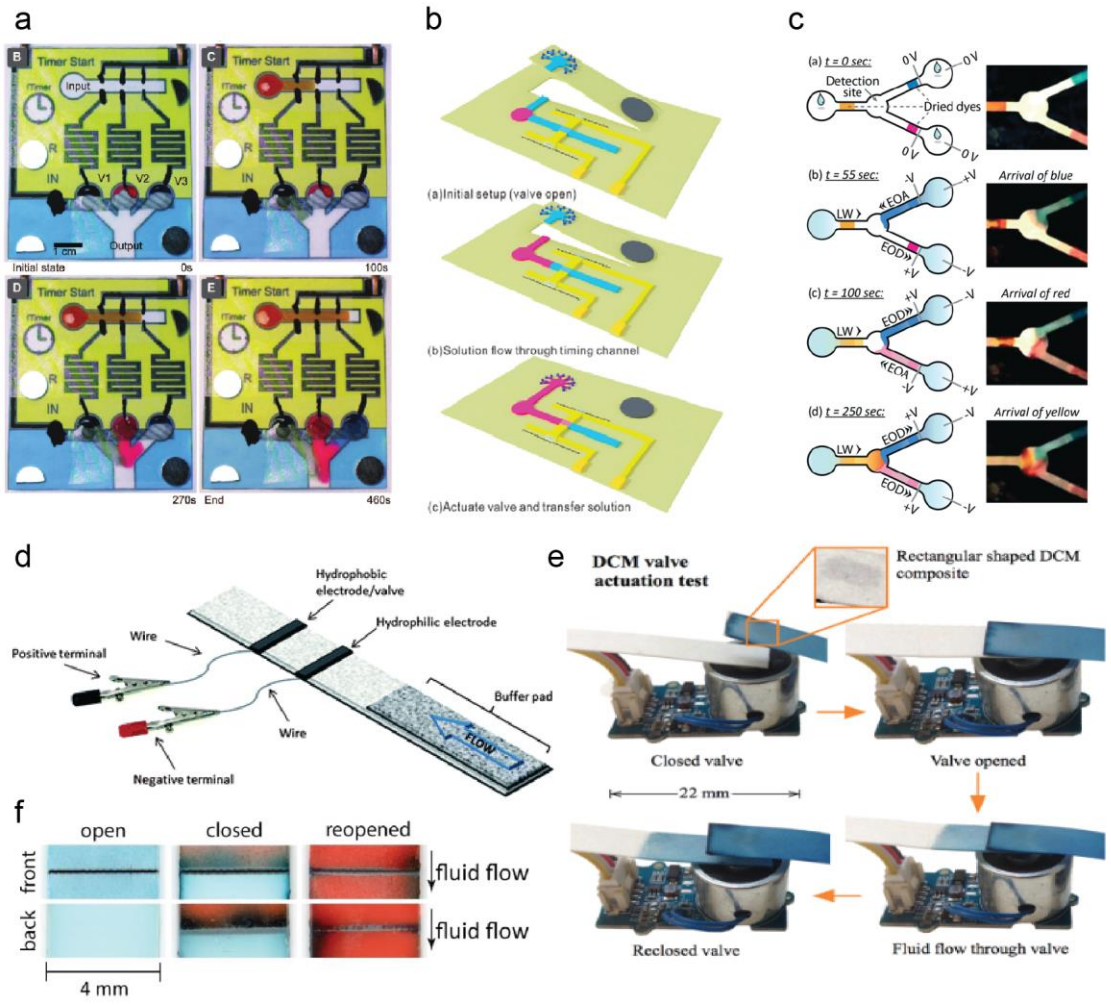

Fig. 1.4 Flow control in paper using electrical/magnetic/thermal approaches. (a) Fabric valves that rely on application of a potential to change wettability of the textile. Adapted from (Ainla et al. 2017) with permission from John Wiley and Sons. (b) Electromagnetically actuated valve and time controller. Connecting the circuit via wash buffer completes the circuit and actuates the magnetic PDMS channel. Adapted from (Wang et al. 2018a) with permission from Elsevier. (c) Control preferred wicking direction via electroosmotic pumping. Adapted from (Rosenfeld and Bercovici 2019) with permission from The Royal Society of Chemistry. (d) Fluidic valve that actuates under the application of a potential. Adapted from (Koo et al. 2013) with permission from The Royal Society of Chemistry. (e) Magnetic NdFeB powder is deposited onto a paper channel. An applied magnetic field causes the channel to bend, connect it to another channel. Adapted with permission from (Fratzl et al. 2018). (https://pubs.acs.org/doi/abs/10.1021/acsomega.7b01839) This is an unofficial adaptation of an article that appeared in an ACS publication. ACS has not endorsed the content of this adaptation or the context of its use. Further permissions related to the material excerpted should be directed to the ACS. (f) Thermally actuated wax valves that can open and close in response to temperature changes. Adapted from (Phillips et al. 2016) with permission from The Royal Society of Chemistry.

1.2. Application of Paper-based Analytical Devices

Paper-based devices have been designed for a plethora of different applications, ranging from environmental monitoring to personal health. What follows is a summary of different devices developed in the last 2-3 years and their applications. For more thorough reviews of different devices, please refer to the reviews of (Brothers et al. 2019; Tang et al. 2019; Noviana et al. 2020; Ratajczak and Stobiecka 2020).

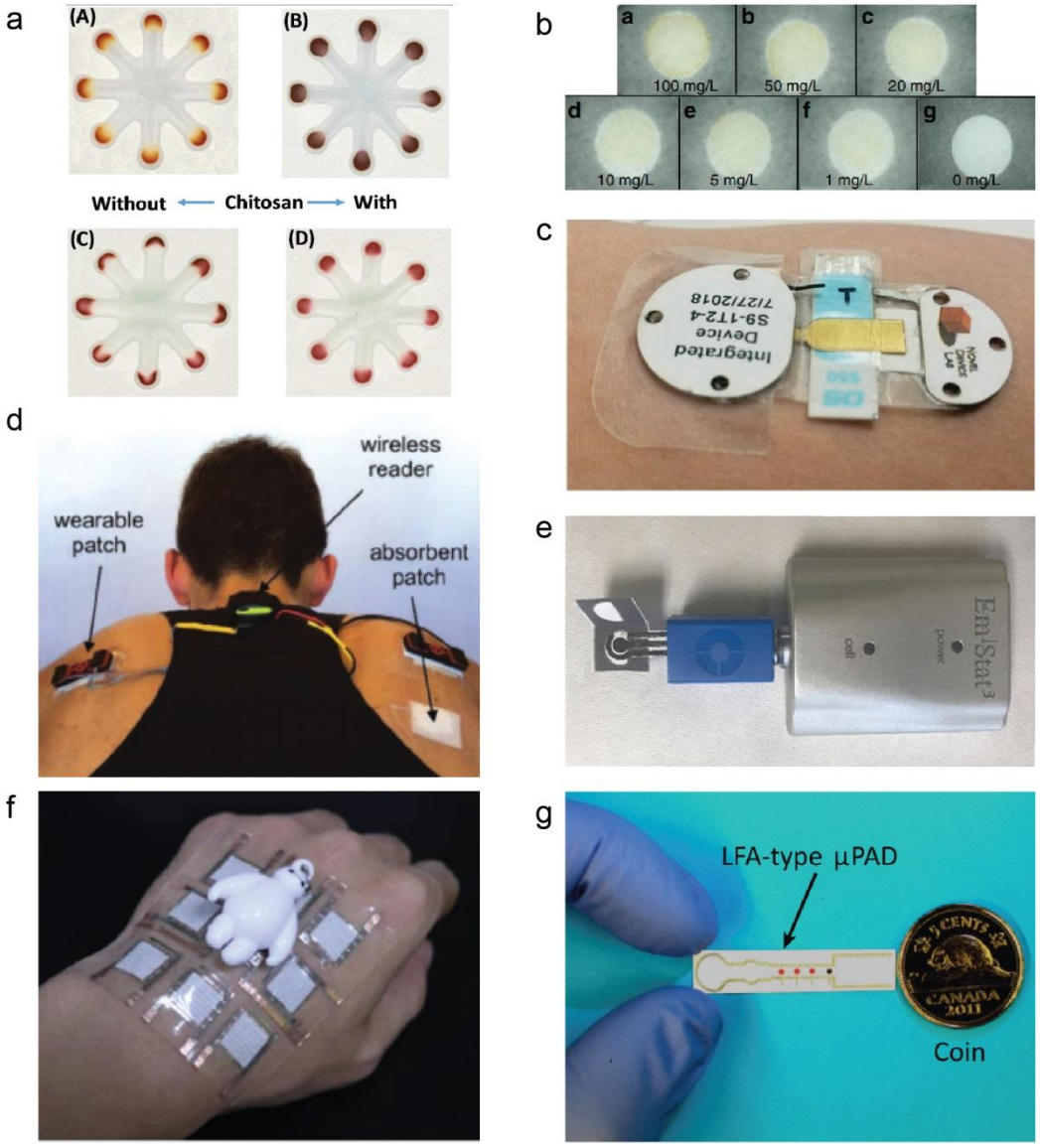

Fig. 1.5 Paper-based analytical devices designed for the detection of different analytes. (a) Paper-based detection of glucose and uric acid from biological fluids. Adapted from (Gabriel et al. 2016) with permission from The Royal Society of Chemistry. (b) Colorimetric paper-based sensor for heavy metal ions (Cu^{2+}). Adapted from (Guan and Sun 2020). (c) Continuous-monitoring sweat sensor that measures sweat alcohol levels. Adapted from (Hauke et al. 2018) with permission from The Royal Society of Chemistry. (d) Wearable paper-based sensor for perspiration monitoring. Adapted from (Parrilla et al. 2019) with permission from John Wiley and Sons. (e) Electrochemical paper-based sensor for detection of mustard gas. Adapted from (Colozza et al. 2019) with permission from Elsevier. (f) Paper-based pressure sensor designed for use in electronic, artificial skin. Adapted with permission from (Gao et al. 2019). Copyright (2019) American Chemical Society. (g) Miniaturized paper-based device, which only requires ~5μL of sample volume. Reprinted from (Mahmud et al. 2020) with permission from AIP Publishing.

1.2.1. Medical Applications

According to a recent report by the World Bank and WHO, at least half the global population cannot obtain essential healthcare. Roughly 800 million people spend at least 10% of their annual income on healthcare. Moreover, health care expenses for 100 million people are high enough to push them into extreme poverty (WHO 2017). These issues disproportionately affect developing countries, which typically have more dense populations and poor healthcare infrastructure. Rapid and affordable diagnostic assays would go a long way towards addressing these healthcare deficiencies.

Bills *et al.* developed a paper-based device that can separate, and measure white blood cell counts from whole blood (Bills et al. 2019). The paper device consists of a three-layer stack comprised of fiberglass, Whatman GF/D microfiber and Whatman 1 chromatography paper. As blood passes vertically through the device, the white blood cells are captured in the middle layer. The group uses a commercial smartphone microscope attachment and a small LED to visualize the WBCs on the captured layer for cell counting. Songjaroen *et al.* designed a simple blood-typing device that consists of filter paper, an absorbent gel and a 3D-printed plastic cassette (Songjaroen et al. 2018). Anti-A and anti-

B antibodies are pre-immobilized onto the filter paper in the shape of letters ‘A’ and ‘B’ respectively. As the blood passes through the device, the antibodies bind to the blood and elicit a color change. The colored letters indicate the blood type of the sample. Paper-based devices have also been demonstrated with other bodily fluids such as saliva and urine. Previous efforts showcased glucose detection from saliva samples (Gabriel et al. 2016; de Freitas et al. 2018) (Fig. 1.5a). Ferreira *et al.* developed a μPAD for determining nitrate/nitrite concentrations from human saliva (Ferreira et al. 2020). Higher concentrations of these ions are usually indicative of gastric cancer. Zhang *et al.* developed a simple colorimetric assay for glucose detection from urine, which utilizes a traditional sandwich ELISA format (Zhang et al. 2019). The device consisted of inkjet-printed channels on filter paper with a detection zone functionalized with the enzyme of interest. An interesting alternative application was developed by Mankar *et al.* who designed a microbial fuel cell that can harvest energy from urine (Mankar et al. 2019). The device consisted of conductive inks printed onto filter paper and immersed in an electrolyte solution. The group was able to generate potentials up to 400 mV.

1.2.2. Environmental Monitoring & Food Safety

With climate change becoming a more visible threat, efforts are being launched to curtail its effects through investment in environmental monitoring. To that end, paper-based devices are being used for low-cost monitoring of different natural resources. Water testing is the most common application, with many different types of analytes detectable using paper devices. Guan *et al.* demonstrated a paper-based colorimetric sensor for copper ions (Guan and Sun 2020). The device consisted of a paper channel with stamped PDMS

boundaries (Fig. 1.5b). The channels were stamped with reagents to provide colorimetric readouts. The specified limit of detection (LOD) was 1 mg/mL. Ding *et al.* developed a modified paper sampler for potentiometric detection of lead and cadmium (Ding et al. 2019). The filter paper was pre-treated with different salts to increase binding affinity of metals ions to the paper. Ion concentrations were determined using normal potentiometry. Lin *et al.* developed a colorimetric assay for E. coli detection in water samples (Lin et al. 2020). Polyurethane acrylate (PUA) was stamped onto paper to create hydrophobic boundaries. Reagents were added to the paper for colorimetric analysis. The group achieved a linear response in the range of 10^4 to 10^9 cfu/mL. Tromfimchuk *et al*. developed a similar colorimetric assay to detect norfloxacin in different food sources (Trofimchuk et al. 2020). Norfloxacin is an antibiotic that is commonly used in animal agriculture and by humans to treat urinary tract infections and other sexually transmitted diseases. Excessive amounts of this drug in food can lead to the emergence of drug-resistant bacteria and cancers, which is why the use of the drug in agriculture is regulated. Determination of norfloxacin concentration in food samples was achieved by monitoring the colorimetric reaction between norfloxacin and iron (III) nitrate nonahydrate in 5 mM ammonia that was added in each reaction chamber.

1.2.3. Wearable Sensors

An interesting area of development for paper-based devices is the field of wearable sensors. These are diagnostic devices that are worn on the body and provide continuous, real-time monitoring of different signals. Wearable sensors eliminate the need for testing at specific intervals and can be coupled with smartphones for rapid data

recording and transmission. Earlier designs of wearable sensors dealt mainly with flexible, plastic substrates patterned with different circuitry (Hauke et al. 2018; Francis et al. 2019; Torrente-Rodríguez et al. 2020) (Fig. 1.5c). Recent advances have seen paper substrates incorporated into these sensors. Parrilla *et al.* developed a wearable paper-based sweat sensor that can monitor perspiration in real time (Parrilla et al. 2019). The device consists of filter paper that is made conductive through the deposition of single-walled carbon nanotubes (Fig. 1.5d). The sensor is worn on the upper back during testing. Changes in the resistance of the carbon nanotube network are proportional to perspiration rate. Colozza *et al.* developed a wearable sensor for detection of sulfur mustard, a volatile compound commonly used in biological weapons (Colozza et al. 2019). The device measures sulfur concentration amperometrically based on the inhibition of the choline oxidase enzyme spotted on the sensor (Fig. 1.5e). The sensor is designed for use with soldiers and is worn on the arm. Gao *et al.* designed a wearable all paper-based piezoresistive (APBP) pressure sensor that detects arterial pulses and other surface measurements such as throat movements during speech (Gao et al. 2019) (Fig. 1.5f). De Castro *et al.* designed a wearable sensor to measure glucose levels from saliva (de Castro et al. 2019). Unlike most wearable devices, this one is placed in the mouth (akin to a mouth guard). The device simply consists of a filter paper channel spotted with reagents and a 3D-printed holder.

1.3. Conclusion and Future Perspectives

Over the last decade, paper-based microfluidic devices have evolved into a highly complex field. As the mechanics of flow in porous media are better understood, researchers can control this flow with greater precision. Modern devices incorporate

numerous types of fluid control, ranging from simple mechanical actuation to highly automated electrical control. Moreover, these devices are being used for a plethora of different applications. Current research aims to further reduce sample requirements for different assays. Mahmud *et al.* have designed LFAs capable of using sub-microliter sample volumes (Mahmud et al. 2020) (Fig. 1.5g). The group demonstrated colorimetric detection of glucose and IgG using only 0.5 μL and 1 μL of sample respectively.

While many promising paper-based devices have been developed on the benchtop, most have not found commercial success. One problem is the lack of high-throughput processes that can mass-produce these devices. Many μPADs are fabricated in small batches, whereas commercialization requires mass production. This is especially problematic for origami devices, which require folding to be used properly. The success of LFAs is partially due to their suitability for automated, mass production. Another challenge is the lack of commercial standards specific for paper devices. Medical device standards such as ISO 13485 and FDA 21 CFR Part 820 provide general guidelines on quality control, but standardization of manufacturing techniques for different design features is needed. Additionally, microfluidic devices have not yet discovered a 'killer application' that could give these devices mass-market appeal (Volpatti and Yetisen 2014). The LFA became popular after its use in home-pregnancy tests. While LFAs have been used to detect other markers, their continued popularity is still driven by pregnancy-test kits. Commercial success rewards devices which diagnose common ailments ('low-hanging fruit') while academic research favors novel devices with niche applications. This means that most academic researchers are not making devices with an eye towards commercialization.

Among the first movers in this space is a nonprofit group called Diagnostics for All (DFA), which was co-founded in 2007 by George Whitesides. The goal of the organization is to provide affordable diagnostic tests to resource-limited settings (Diagnostics for All Inc.). Currently, the group is developing assays for liver function assessment, HIV detection and child nutrition tests.

Additionally, a handful of companies are attempting to successfully commercialize paper-based devices. One such company is Phase Scientific, which was co-founded by several UCLA students and professors. Their current products include PHASIFY™, a nucleic acid extraction/purification platform and INDICAID™, a diagnostic platform to assess tooth decay (Phase Scientific Int. Ltd.). This technology is based on the work of Daniel Kamei at UCLA who researches aqueous two-phase systems in LFAs. As of this writing, the company is working to commercialize their technology in Hong Kong. Another company called Group K Diagnostics is developing point-of-care devices which can work with human samples. Their flagship product, KormaHeath Kit, requires only a few drops of human sample (blood, urine or serum) and provides colorimetric readouts which are processed using special software (Group K Diagnostics Inc.). Currently, the company is developing this platform for zika virus, blood counting and liver function. They hope to add HIV and cancer detection in future versions. PaperdropDX, a Spanish startup founded in 2016, has a similar goal. The company is developing lateral flow platform for rapid diagnosis of different targets (Paperdrop Diagnostics). Their first product, Faststroke, determines the risk of ischemic stroke from a single drop of blood. A potentially big player in this field is Mammoth Biosciences. The

company was co-founded by Jennifer Doudna, who is one of the pioneers of the CRISPR-CAS gene-editing system. The company is currently developing rapid assays for detection of SARS-COV-2 (Mammoth Biosciences Inc.). An oral/nasal swab is collected, RNA is extracted from the sample, converted to DNA and then mixed with CAS12 and SARS-COV-2 sequences. The result is read out using a LFA. Away from diagnostics, SoilCards, a UK-based start-up is developing paper-based tests to measure soil quality. The user adds soil onto a sticky sample pad then folds the device closed (Science Practice Ltd.). Water is then added, which washes the soil and wicks nutrients into the detection region, where a colorimetric readout is obtained. The company conducted in-field research in Kenya in 2017 and is currently working with farms in the UK to test their product. All these companies are in the early stages of development.

Paper-based devices have great potential for widespread success. However, a thorough understanding of flow behavior and use of flow-control techniques that are amenable to mass production are needed to fabricate more complex, functional devices.

1.4. References

Abe, K., Kotera, K., Suzuki, K., Citterio, D., 2010. Analytical and Bioanalytical Chemistry 398, 885-893.

Ainla, A., Hamedi, M.M., Güder, F., Whitesides, G.M., 2017. Advanced Materials 29, 1702894.

Akyazi, T., Gil-González, N., Basabe-Desmonts, L., Castaño, E., Morant-Miñana, M., Benito-Lopez, F., 2017. Sensors and Actuators B: Chemical 247, 114-123.

Akyazi, T., Tudor, A., Diamond, D., Basabe-Desmonts, L., Florea, L., Benito-Lopez, F., 2018. Sensors and Actuators B: Chemical 261, 372-378.

Apilux, A., Ukita, Y., Chikae, M., Chailapakul, O., Takamura, Y., 2013. Lab on a Chip 13, 126-135.

Atabakhsh, S., Ashtiani, S.J., 2019. Microfluidics and Nanofluidics 23, 69.

Atabakhsh, S., Ashtiani, S.J., 2018. Microfluidics and Nanofluidics 22, 43.

Bills, M.V., Nguyen, B.T., Yoon, J.-Y., 2019. IEEE Sensors Journal 19, 7822-7828.

Brothers, M.C., DeBrosse, M., Grigsby, C.C., Naik, R.R., Hussain, S.M., Heikenfeld, J., Kim, S.S., 2019. Accounts of chemical research 52, 297-306.

Camplisson, C.K., Schilling, K.M., Pedrotti, W.L., Stone, H.A., Martinez, A.W., 2015. Lab on a Chip 15, 4461-4466.

Carrilho, E., Martinez, A.W., Whitesides, G.M., 2009. Analytical Chemistry 81, 7091-7095.

Castro, C., Rosillo, C., Tsutsui, H., 2017. Microfluidics and Nanofluidics 21, 21.

Channon, R.B., Nguyen, M.P., Scorzelli, A.G., Henry, E.M., Volckens, J., Dandy, D.S., Henry, C.S., 2018. Lab on a Chip 18, 793-802.

Chen, B., Kwong, P., Gupta, M., 2013. Acs Appl Mater Inter 5, 12701-12707.

Chen, C., Zhao, L., Zhang, H., Shen, X., Zhu, Y., Chen, H., 2019. Analytical chemistry 91, 5169-5175.

Chen, H., Cogswell, J., Anagnostopoulos, C., Faghri, M., 2012. Lab on a Chip 12, 2909-2913.

Chiang, C.-K., Kurniawan, A., Kao, C.-Y., Wang, M.-J., 2019. Talanta 194, 837-845.

Chiem, N.H., Harrison, D.J., 1998. Clinical chemistry 44, 591-598.

Chitnis, G., Ding, Z.W., Chang, C.L., Savran, C.A., Ziaie, B., 2011. Lab on a Chip 11, 1161-1165.

Chou, K.-H., Yeh, S.-H., Yang, R.-J., 2017. Microfluidics and Nanofluidics 21, 112.

Colozza, N., Kehe, K., Dionisi, G., Popp, T., Tsoutsoulopoulos, A., Steinritz, D., Moscone, D., Arduini, F., 2019. Biosensors and bioelectronics 129, 15-23.

Cummins, B.M., Chinthapatla, R., Lenin, B., Ligler, F.S., Walker, G.M., 2017. Technology 5, 21-30.

da Silva, E.T., Santhiago, M., de Souza, F.R., Coltro, W.K., Kubota, L.T., 2015. Lab on a Chip 15, 1651-1655.

de Castro, L.F., de Freitas, S.V., Duarte, L.C., de Souza, J.A.C., Paixão, T.R., Coltro, W.K., 2019. Analytical and bioanalytical chemistry 411, 4919-4928.

de Freitas, S.V., de Souza, F.c.R., Rodrigues Neto, J.C., Vasconcelos, G.s.A., Abdelnur, P.c.V., Vaz, B.G., Henry, C.S., Coltro, W.K., 2018. Analytical chemistry 90, 11949-11954.

Deng, M., Liao, C., Wang, X., Chen, S., Qi, F., Zhao, X., Yu, P., 2019. Canadian Journal of Chemistry 97, 373-377.

Diagnostics for All Inc., (Salem, MA). http://dfa.org/ Accessed December 28, 2020

Dieterich, K., 1902. US Patent, 691249, USA.

Dimitrakellis, P., Travlos, A., Psycharis, V.P., Gogolides, E., 2017. Plasma Processes and Polymers 14, 1600069.

Ding, R., Krikstolaityte, V., Lisak, G., 2019. Sensors and Actuators B: Chemical 290, 347-356.

Dungchai, W., Chailapakul, O., Henry, C.S., 2011. Analyst 136, 77-82.

Dungchai, W., Chailapakul, O., Henry, C.S., 2010. Analytica chimica acta 674, 227-233.

Elizalde, E., Urteaga, R., Berli, C.L., 2015. Lab on a Chip 15, 2173-2180.

Fenton, E.M., Mascarenas, M.R., Lopez, G.P., Sibbett, S.S., 2009. Acs Appl Mater Inter 1, 124-129.

Ferreira, F.T., Mesquita, R.B., Rangel, A.O., 2020. Talanta, 121183.

Francis, J., Stamper, I., Heikenfeld, J., Gomez, E.F., 2019. Lab on a Chip 19, 178-185.

Fratzl, M., Chang, B.S., Oyola-Reynoso, S., Blaire, G., Delshadi, S., Devillers, T., Ward III, T., Dempsey, N.M., Bloch, J.-F., Thuo, M.M., 2018. ACS omega 3, 2049-2057.

Fu, E., Lutz, B., Kauffman, P., Yager, P., 2010. Lab on a Chip 10, 918-920.

Fu, E.L., Ramsey, S., Kauffman, P., Lutz, B., Yager, P., 2011. Microfluidics and Nanofluidics 10, 29-35.

Fu, X., Cheng, Z., Yu, J., Choo, P., Chen, L., Choo, J., 2016. Biosensors and Bioelectronics 78, 530-537.

Gabriel, E.F., Garcia, P.T., Cardoso, T.M., Lopes, F.M., Martins, F.T., Coltro, W.K., 2016. Analyst 141, 4749-4756.

Gao, B., Chi, J., Liu, H., Gu, Z., 2017. Scientific reports 7, 1-8.

Gao, L., Zhu, C., Li, L., Zhang, C., Liu, J., Yu, H.-D., Huang, W., 2019. Acs Appl Mater Inter 11, 25034-25042.

Giokas, D.L., Tsogas, G.Z., Vlessidis, A.G., 2014. Analytical chemistry 86, 6202-6207.

Group K Diagnostics Inc., (Philadelphia, PA). https://groupkdiagnostics.com/ Accessed December 28, 2020

Guan, Y., Sun, B., 2020. Microsystems & Nanoengineering 6, 1-12.

Haller, P.D., Flowers, C.A., Gupta, M., 2011. Soft Matter 7, 2428-2432.

Han, J., Qi, A., Zhou, J., Wang, G., Li, B., Chen, L., 2018. ACS sensors 3, 1789-1794.

Hauke, A., Simmers, P., Ojha, Y., Cameron, B., Ballweg, R., Zhang, T., Twine, N., Brothers, M., Gomez, E., Heikenfeld, J., 2018. Lab on a Chip 18, 3750-3759.

Heist, C.A., Bandara, G.C., Bemis, D.J., Pommerenck, J.C., Remcho, V.T., 2018. Analytical methods 10, 2994-3000.

Hossain, S.Z., Brennan, J.D., 2011. Analytical chemistry 83, 8772-8778.

Houghtaling, J., Liang, T., Thiessen, G., Fu, E., 2013. Analytical chemistry 85, 11201-11204.

Jahanshahi-Anbuhi, S., Henry, A., Leung, V., Sicard, C., Pennings, K., Pelton, R., Brennan, J.D., Filipe, C.D., 2014. Lab on a Chip 14, 229-236.

Jang, I., Song, S., 2015. Lab on a Chip 15, 3405-3412.

Kalish, B., Tan, M.K., Tsutsui, H., 2020. Microfluidics and nanofluidics.

Kalish, B., Tsutsui, H., 2014. Lab on a Chip 14, 4354-4361.

Kalish, B., Tsutsui, H., 2016. JoVE (Journal of Visualized Experiments), e53805.

Kettler, H., White, K., Hawkes, S.J., 2004. Geneva: World Health Organization.

Kim, K.S., Park, J.-K., 2005. Lab on a Chip 5, 657-664.

Kim, T.H., Hahn, Y.K., Kim, M.S., 2020. Micromachines 11, 269.

Kim, T.H., Hahn, Y.K., Lee, J., Van Noort, D., Kim, M.S., 2018. Analytical chemistry 90, 2534-2541.

Kong, T., Flanigan, S., Weinstein, M., Kalwa, U., Legner, C., Pandey, S., 2017. Lab on a Chip 17, 3621-3633.

Koo, C.K., He, F., Nugen, S.R., 2013. Analyst 138, 4998-5004.

Koşak Söz, C.a.l., Trosien, S., Biesalski, M., 2018. Acs Appl Mater Inter 10, 37478-37488.

Lai, Y.-T., Tsai, C.-H., Hsu, J.-C., Lu, Y.-W., 2019. Micromachines 10, 837.

Lazar, I.M., Trisiripisal, P., Sarvaiya, H.A., 2006. Analytical chemistry 78, 5513-5524.

Li, B., Yu, L., Qi, J., Fu, L., Zhang, P., Chen, L., 2017a. Analytical chemistry 89, 5707-5712.

Li, C., Boban, M., Tuteja, A., 2017b. Lab on a Chip 17, 1436-1441.

Li, H., Steckl, A.J., 2018. Analytical chemistry 91, 352-371.

Li, W., Shi, Z., Fang, C., Lu, Y., Yu, L., Li, C.M., 2017c. Microfluidics and Nanofluidics 21, 71.

Li, X., Chen, W., Liu, G., Lu, W., Fu, J., 2014. Lab on a Chip 14, 2565-2575.

Li, Z., Li, F., Xing, Y., Liu, Z., You, M., Li, Y., Wen, T., Qu, Z., Li, X.L., Xu, F., 2017d. Biosensors and Bioelectronics 98, 478-485.

Lim, H., Jafry, A.T., Lee, J., 2019. Molecules 24, 2869.

Lin, D., Li, B., Qi, J., Ji, X., Yang, S., Wang, W., Chen, L., 2020. Sensors and Actuators B: Chemical 303, 127213.

Liu, J., Kong, X., Wang, H., Zhang, Y., Fan, Y., 2020. Microfluidics and Nanofluidics 24, 6.

Liu, M., Zhang, C., Liu, F., 2015. Analytica chimica acta 891, 234-246.

Liu, N., Xu, J., An, H.-J., Phan, D.-T., Hashimoto, M., Lew, W.S., 2017a. Journal of Micromechanics and Microengineering 27, 104001.

Liu, Q., Xu, C., Liang, H., 2017b. Talanta 175, 289-296.

Lu, Y., Shi, W., Jiang, L., Qin, J., Lin, B., 2009. Electrophoresis 30, 1497-1500.

Lutz, B., Liang, T., Fu, E., Ramachandran, S., Kauffman, P., Yager, P., 2013. Lab on a Chip 13, 2840-2847.

Mahmud, M.A., Blondeel, E.J., MacDonald, B.D., 2020. Biomicrofluidics 14, 014107.

Malmstadt, N., Yager, P., Hoffman, A.S., Stayton, P.S., 2003. Analytical chemistry 75, 2943-2949.

Mammoth Biosciences Inc., (San Francisco, CA). https://mammoth.bio/ Accessed December 28, 2020

Mankar, C., Rewatkar, P., Dhone, M., Balpande, S., Kalambe, J., Pande, R., Goel, S., 2019. Sensor Letters 17, 69-74.

Martinez, A.W., Phillips, S.T., Butte, M.J., Whitesides, G.M., 2007. Angewandte Chemie International Edition 46, 1318-1320.

Martinez, A.W., Phillips, S.T., Wiley, B.J., Gupta, M., Whitesides, G.M., 2008. Lab on a Chip 8, 2146-2150.

Mendez, S., Fenton, E.M., Gallegos, G.R., Petsev, D.N., Sibbett, S.S., Stone, H.A., Zhang, Y., López, G.P., 2010. Langmuir 26, 1380-1385.

Michael, I.J., Kumar, S., Oh, J.M., Kim, D., Kim, J., Cho, Y.-K., 2018. Acs Appl Mater Inter 10, 33839-33846.

Modha, S., Castro, C., Tsutsui, H., 2021. Biosensors and Bioelectronics 178, 113026.

Nargang, T.M., Dierkes, R., Bruchmann, J., Keller, N., Sachsenheimer, K., Lee-Thedieck, C., Kotz, F., Helmer, D., Rapp, B.E., 2018. Analytical methods 10, 4028-4035.

Navarro, F., Davalos, F., Denes, F., Cruz, L., Young, R., Ramos, J., 2003. Cellulose 10, 411-424.

Nie, Z., Deiss, F., Liu, X., Akbulut, O., Whitesides, G.M., 2010. Lab on a Chip 10, 3163-3169.

Noh, H., Phillips, S.T., 2010a. Analytical chemistry 82, 8071-8078.

Noh, H., Phillips, S.T., 2010b. Analytical chemistry 82, 4181-4187.

Noviana, E., Carrão, D.B., Pratiwi, R., Henry, C.S., 2020. Analytica Chimica Acta 1116, 70-90.

Ozer, T., McMahon, C., Henry, C.S., 2020. Annual Review of Analytical Chemistry 13.

Pal, A., Goswami, D., Cuellar, H.E., Castro, B., Kuang, S., Martinez, R.V., 2018. Biosensors and Bioelectronics 117, 696-705.

Paperdrop Diagnostics, Barcelona, Spain. http://paperdropdx.com/ Accessed December 28, 2020

Park, J., Park, J.-K., 2017. Sensors and Actuators B: Chemical 246, 1049-1055.

Park, J., Shin, J.H., Park, J.K., 2016. Micromachines 7.

Parrilla, M., Guinovart, T., Ferré, J., Blondeau, P., Andrade, F.J., 2019. Advanced Healthcare Materials 8, 1900342.

Phase Scientific Int. Ltd., Kwun Tong, Kowloon, Hong Kong. https://phasescientific.com/ Accessed December 28, 2020

Phillips, E.A., Shen, R., Zhao, S., Linnes, J.C., 2016. Lab on a Chip 16, 4230-4236.

Potter, J., Brisk, P., Grover, W.H., 2019. Lab on a Chip 19, 2000-2008.

Preechakasedkit, P., Siangproh, W., Khongchareonporn, N., Ngamrojanavanich, N., Chailapakul, O., 2018. Biosensors and Bioelectronics 102, 27-32.

Ratajczak, K., Stobiecka, M., 2020. Carbohydrate polymers 229, 115463.

Ratnarathorn, N., Chailapakul, O., Henry, C.S., Dungchai, W., 2012. Talanta 99, 552-557.

Renault, C., Li, X., Fosdick, S.E., Crooks, R.M., 2013. Analytical chemistry 85, 7976-7979.

Rivas, L., Medina-Sánchez, M., de la Escosura-Muñiz, A., Merkoçi, A., 2014. Lab on a Chip 14, 4406-4414.

Rosenfeld, T., Bercovici, M., 2019. Lab on a Chip 19, 328-334.

Schilling, K.M., Lepore, A.L., Kurian, J.A., Martinez, A.W., 2012. Analytical chemistry 84, 1579-1585.

Science Practice Ltd., London, UK. https://www.science-practice.com/ventures/soilcards/ Accessed December 28, 2020

Shin, J.-H., Lee, G.-J., Kim, W., Choi, S., 2016. Sensors and Actuators B: Chemical 230, 380-387.

Shin, J.H., Park, J., Kim, S.H., Park, J.-K., 2014. Biomicrofluidics 8, 054121.

Songjaroen, T., Dungchai, W., Chailapakul, O., Laiwattanapaisal, W., 2011. Talanta 85, 2587-2593.

Songjaroen, T., Primpray, V., Manosarn, T., Khumchanta, W., Sakuldamrongpanich, T., Kulkeratiyut, S., Laiwattanapaisal, W., 2018. Journal of Immunoassay and Immunochemistry 39, 292-307.

Strong, E.B., Knutsen, C., Wells, J.T., Jangid, A.R., Mitchell, M.L., Martinez, N.W., Martinez, A.W., 2019. Inventions 4, 20.

Sun, X., Li, B., Tian, C., Yu, F., Zhou, N., Zhan, Y., Chen, L., 2018. Analytica chimica acta 1007, 33-39.

Tachibana, H., Saito, M., Shibuya, S., Tsuji, K., Miyagawa, N., Yamanaka, K., Tamiya, E., 2015. Biosensors and Bioelectronics 74, 725-730.

Tang, R.H., Liu, L.N., Zhang, S.F., He, X.C., Li, X.J., Xu, F., Ni, Y.H., Li, F., 2019. Microchimica Acta 186, 521.

Toley, B.J., McKenzie, B., Liang, T., Buser, J.R., Yager, P., Fu, E., 2013. Analytical chemistry 85, 11545-11552.

Toley, B.J., Wang, J.A., Gupta, M., Buser, J.R., Lafleur, L.K., Lutz, B.R., Fu, E., Yager, P., 2015. Lab on a Chip 15, 1432-1444.

Torrente-Rodríguez, R.M., Tu, J., Yang, Y., Min, J., Wang, M., Song, Y., Yu, Y., Xu, C., Ye, C., IsHak, W.W., 2020. Matter 2, 921-937.

Trofimchuk, E., Nilghaz, A., Sun, S., Lu, X., 2020. Journal of Food Science 85, 736-743.

Van Hooij, A., Fat, E.M.T.K., Richardus, R., Van Den Eeden, S.J., Wilson, L., Claudia, J., Faber, R., Alam, K., Richardus, J.H., Corstjens, P.L., 2016. Scientific reports 6, 34260.

Verma, M.S., Tsaloglou, M.-N., Sisley, T., Christodouleas, D., Chen, A., Milette, J., Whitesides, G.M., 2018. Biosensors and Bioelectronics 99, 77-84.

Volpatti, L.R., Yetisen, A.K., 2014. Trends in biotechnology 32, 347-350.

Wang, C.-C., Hennek, J.W., Ainla, A., Kumar, A.A., Lan, W.-J., Im, J., Smith, B.S., Zhao, M., Whitesides, G.M., 2016. Analytical chemistry 88, 6326-6333.

Wang, J., Li, W., Ban, L., Du, W., Feng, X., Liu, B.-F., 2018a. Sensors and Actuators B: Chemical 254, 855-862.

Wang, S., Ge, L., Song, X., Yu, J., Ge, S., Huang, J., Zeng, F., 2012. Biosensors and bioelectronics 31, 212-218.

Wang, T., Hu, M., Yang, B., Wang, X., Chen, X., Liu, J.-Q., 2018b. 2018 IEEE Micro Electro Mechanical Systems (MEMS), pp. 1249-1252. IEEE.

Wang, X., Choi, N., Cheng, Z., Ko, J., Chen, L., Choo, J., 2017. Analytical chemistry 89, 1163-1169.

Weng, C.H., Chen, M.Y., Shen, C.H., Yang, R.J., 2014. Biomicrofluidics 8.

WHO, 2017. WHO, Tokyo. Accessed June 5, 2020

Yetisen, A.K., Akram, M.S., Lowe, C.R., 2013. Lab Chip 13, 2210-2251.

Yung, C.W., Fiering, J., Mueller, A.J., Ingber, D.E., 2009. Lab on a Chip 9, 1171-1177.

Zhang, C., Xing, D., Li, Y., 2007. Biotechnology advances 25, 483-514.

Zhang, D., Huang, L., Liu, B., Ni, H., Sun, L., Su, E., Chen, H., Gu, Z., Zhao, X., 2018. Biosensors and Bioelectronics 106, 204-211.

Zhang, H., Smith, E., Zhang, W., Zhou, A., 2019. Biomedical microdevices 21, 48.

Zhao, M., Li, H., Liu, W., Guo, Y., Chu, W., 2016. Biosensors and Bioelectronics 79, 581-588.

2. USING FLOW CONTROLS IN PAPER-BASED DEVICES

2.1 Introduction

Since the introduction of microfluidic paper-based analytical devices (μPADs) in 2007, the field of paper-based diagnostics has expanded rapidly (Martinez et al. 2007). The use of paper for diagnostic purposes was reported as far back as the early 1900s (Dieterich 1902; Yetisen et al. 2013). However, it was not until the 1950s when modern paper-based diagnostics were first reported with the introduction of the lateral flow assay which was mainly used for home pregnancy tests (Yetisen et al. 2013). Martinez *et al.* showed how fluidic circuits can be created in paper using simple lithography (Martinez et al. 2007) . Since then, μPADs have been developed for a plethora of applications, such as disease detection from human samples as well as various crops and food sources (Li and Steckl 2018). Paper provides numerous advantages compared to traditional microfluidic substrates, such as lower material costs and the ability to wick fluids spontaneously through capillary action, making paper devices more affordable and user-friendly.

Initially, μPADs were used for simple, colorimetric assays, such as detection of glucose or heavy-metal ions, which typically only require single fluid types (sample) spotted or wicked onto the paper (Dungchai et al. 2010; Hossain and Brennan 2011; Ratnarathorn et al. 2012). However, recent developments in paper-based devices have seen the adaptation of more complicated, multi-step procedures (Park and Park 2017; Verma et al. 2018). The simplest approach is to manually deposit these reagents at different times. However, this would make the device significantly less user-friendly. Typically, automated

fluid control on μPADs has been achieved by engineering delays on the paper to slow the fluid down. A distance-based delay is the easiest to implement, which consists of increasing the length of the channel (Fu et al. 2010; Fu et al. 2011; Apilux et al. 2013). However, this approach is limited by the footprint of the device as well as the volume of sample since longer channels require more fluid volume to fill them. Other efforts include adding dissolvable barriers onto the paper, providing additional wicking material (known as a shunt) that the fluid must pass through, and reducing the available wicking area through geometry changes (Toley et al. 2013; Shin et al. 2014). While effective, delay mechanisms can increase overall assay time. Furthermore, slowing down fluid flow can exacerbate other issues, such as fluid loss due to evaporation or reduced mixing between reagents.

Native paper is a slow wicking material, owing to the complex network of pores inside that creates a highly tortuous path for fluid to follow (Elizalde et al. 2015; Castro et al. 2017) Efforts to accelerate wicking in paper channels have included either sandwiching the paper between polymer films (Jahanshahi-Anbuhi et al. 2014; da Silva et al. 2015), creating a two-ply structure (Camplisson et al. 2015; Channon et al. 2018), physically modifying pore sizes by laser ablation (Kalish et al. 2020), or by removing regions of the paper to create 'macro capillaries' for the liquid to flow through (Renault et al. 2013; Giokas et al. 2014; Shin et al. 2016; Liu et al. 2017). Of interest is the work of Giokas *et al.*. and Liu *et al.*., who demonstrated that etching parallel grooves onto paper channels using either a plotter or a CO_2 laser can lead to much faster wicking speeds.

A recent development in the field is the paper-based chemiresistive biosensor. Utilizing single-walled carbon nanotubes (SWNTs), this type of sensor can detect analyte concentrations based on changes in the electrical properties of the SWNTs. Current label-based electrochemical sensors lack appropriate markers for all types of analytes. Additionally, these sensors require larger fluid volumes to accommodate the necessary redox reactions. By contrast, chemiresistive bisensors are label-free and provide accurate, quantitative data at lower limits of detection (LOD) compared to traditional electrochemical sensors (Villamizar et al. 2008; Yamada et al. 2014; Shen et al. 2019; Shen et al. 2020). In this study, we build upon the work of Giokas *et al.* and Liu *et al.* (Giokas et al. 2014; Liu et al. 2017) by conducting a more thorough analysis of laser-etched grooves on paper. In addition to finding optimum groove parameters, we demonstrated the use of laser-etched grooves on paper for sequential delivery for a chemiresistive biosensor, which we recently reported (Shen et al. 2019). This chapter contains material adopted from one of our previous publications (Modha et al. 2021).

2.2 Materials & Methods

2.2.1 Groove Fabrication

Groove designs were created in Adobe Illustrator CC (Adobe Inc, San Jose, CA). As shown in Fig. 2.1a, Whatman 4 filter paper (GE Healthcare, Chicago, IL) was cut out and etched using an Epilog Zing 16 30W CO_2 laser cutter (Epilog Lasers, Golden, CO). Laser power and frequency were set at 5% and 5000 Hz respectively, while laser speed was varied between 20% and 100% to etch grooves with different depths. The nominal thickness of untreated filter paper is 180μm.

2.2.2 Groove Characterization - Mass Loss

Mass loss was assessed by weighing 50mm x 50mm squares etched with grooves at different speed settings. Grooves were etched with a center-to-center spacing of 350μm (~137 linear grooves/square). Samples were weighed using a model TP-64 analytical balance (Denver Instrument, Bohemia, NY)

2.2.3 Groove Characterization - Cross-sectional Area assessment

Visualization of the grooves was achieved using a Nova NanoSEM 450 scanning electron microscope (SEM) (FEI, Hillsboro, OR). Prior to imaging, paper samples were coated with platinum/palladium using a Cressington 108 Auto Sputter Coater (Cressington Scientific Instruments, UK). Groove morphology was characterized by measuring the cross-sectional area for each groove relative to the total thickness of the paper. Measurements were made using ImageJ (NIH, Bethesda, MD). A 'unit cell' was drawn around each groove, with a width equal to the top width of the groove and a height equal to the thickness of the paper. The fraction of the unit cell that was taken up by the groove was assessed using the polygon tool in ImageJ.

2.2.4 Vertical Wicking

Vertical-wicking test strips were designed in Adobe Illustrator CC. Each test strip has six channels (2mm × 40mm), consisting of one blank (unetched) channel and five channels each with a single groove (etched at a different laser speed) in the center of the channel. Grooves were defined in Illustrator as line segments. Wicking experiments were performed in a humidity-controlled chamber (Model 5503-E, Electro-Tech Systems, Glenside, PA) kept at 99% relative humidity (RH). This high RH minimizes effects of evaporation. Each test strip was mounted vertically to a testing rig and placed inside the chamber (Fig. A1). All channels were tested without washing or other chemical treatment.

A small reservoir of deionized (DI) H_2O was placed onto a laboratory jack (Model L-490, Thorlabs, Newton, NJ) situated beneath the test strip. The jack was raised

until the water touched the bottom of the strip, allowing wicking to commence. Wicking fronts were recorded using a Nikon D5100 camera (Tokyo, Japan) fitted with a Tamron Macro lens (Saitama, Japan). Video files were processed into individual frames using Adobe Premier Pro CS6 (San Jose, CA). Wicking distances were then recorded using ImageJ's Manual Tracking plugin.

2.2.5 Sealed Channels

The previously described wicking experiments were repeated with channels sealed with different tapes. The ones used in this study were Scotch 3M Heavy Duty Shipping Packaging Tape (3M, Two Harbors, MN), MD Weatherstrip Tape (MD Building Products, Oklahoma City, OK) and Uline S-423 Industrial Tape (Uline, Pleasant Prairie, WI). Channels were sealed on the front (side with the groove) or back only and on both sides (Fig. 2.1c). Additionally, paper channels were sealed using thermal laminating pouches (3M, Two Harbors, MN) (Fig. 2.1d, e). To laminate the channels on front/back only, a single laminating sheet was placed onto a hot plate (Torrey Pines, San Diego, CA) set to 150°C. The paper channel was placed on top of the laminating sheet and held there with a small weight for three minutes to insure a proper seal. Channels laminated on both sides were passed through a Scotch Thermal Laminator (3M, Two Harbors, MN) using the 5mil thickness setting.

2.2.6 Wider Grooves

Wicking test strips with wider grooves were created in a similar manner to regular wicking test strips. Rather than defining a groove using a line segment, rectangles with various widths (50μm – 200μm) were instead used to define wider grooves. Laser

settings were fixed at 20% speed and 5% power. Channels were tested untaped and sealed on both sides with Uline S-423 Industrial Tape.

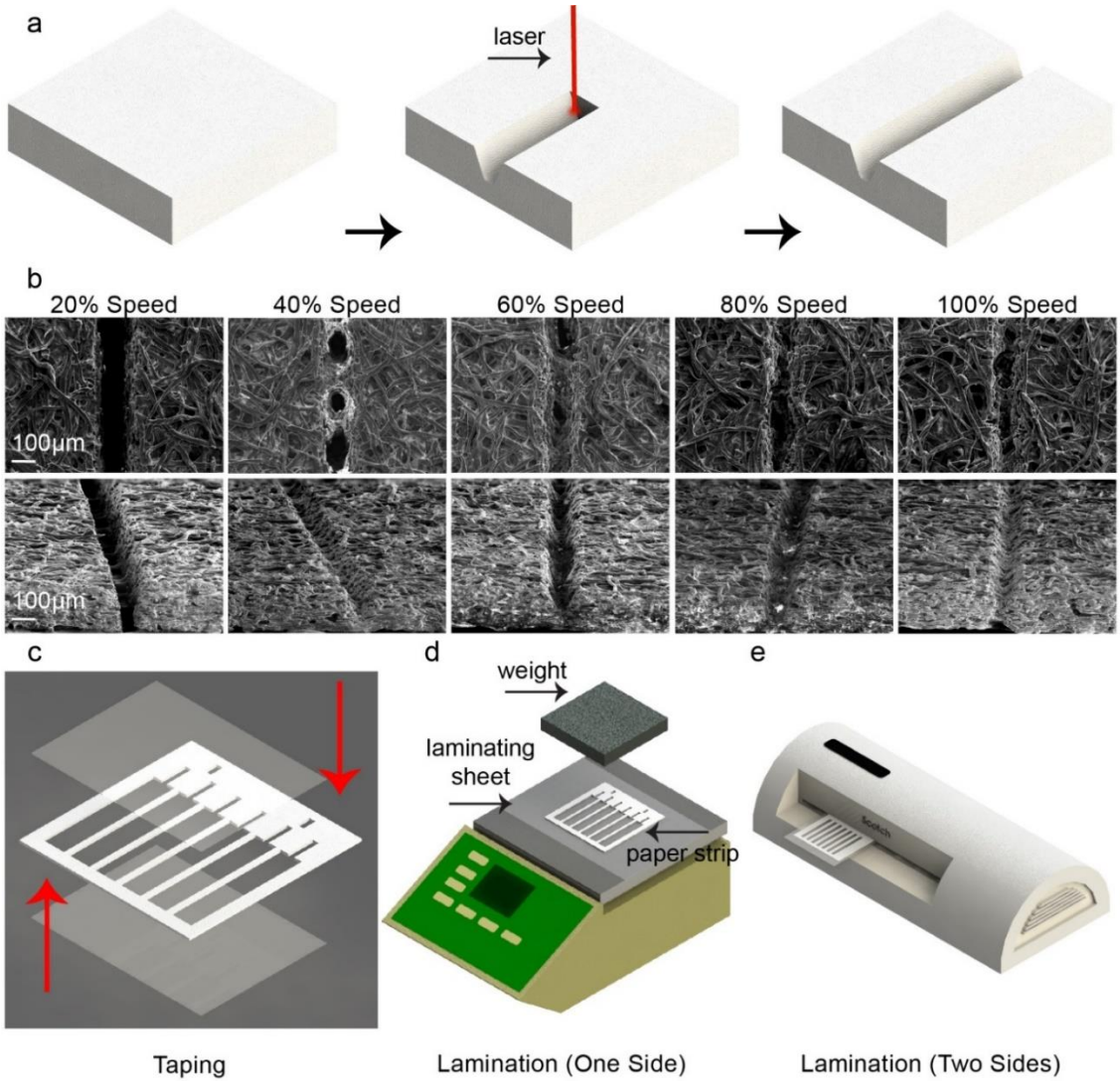

Fig. 2.1 Fabrication of paper-based microfluidic test devices featuring laser-etched grooves (a) Schematic summarizing fabrication of laser-etched grooves on paper. As the laser beam passed the paper, it burnt away some of the material, leaving behind a groove. (b) SEM images of grooves etched at different speeds. Note that while the width of the groove was consistent, the depth was inversely proportional to the etching speed. (c) Taped channels were made by applying tape to either one side of the paper strip or both. (d) Laminating only one side of a paper strip was done by heating the laminate on a hot plate at 150°C and pressing the paper onto it with a weight. (e) Laminating on both sides was done by simply putting the paper strip inside a laminating pouch and passing it through a conventional laminator (5mil thickness setting).

2.2.7 Groove Pitch Optimization

Groove designs were made in Adobe Illustrator, as in the previously described tests. Vertical test strips had channels which were 6 mm wide and 40 mm long. Grooves were etched using the CO_2 laser (speed setting: 20%, power setting: 5%) at different center-to-center pitches, ranging from 0.1 mm to 3 mm. Vertical wicking experiments that were identical to those described above were conducted on untaped channels and channels sealed on both sides with Uline S-423 Industrial Tape.

2.2.8 Effect of Increased Viscosity

Additional wicking experiments were conducted with 10%, 20% and 35% (v/v) glycerol (Fisher) in DI H_2O. These solutions have viscosity values corresponding to 1.38 cP, 1.98 cP and 3.76 cP at 20°C, respectively (Cheng 2008; Volk and Kähler 2018). Channels were tested untaped and taped on both sides with Uline S-423 Industrial Tape. Each test strip had 3 unetched, blank channels and 3 channels etched at 20% speed. Wicking experiments were conducted as described in section 2.4.

2.2.9 Demo Device for Sequential Delivery and Analyte Detection

The demonstration device utilizes a paper-based chemiresistive biosensor employing SWNTs, which we recently reported (Shen et al. 2019). To fabricate this sensor strip, SWNTs (P3-SWNTs, Carbon Solutions, Inc., Riverside, CA,) and pyrene carboxylic acid (PCA) (Tokyo Chemical Industry Co., Ltd. Portland, OR) were dispersed in dimethylformamide (DMF) (Fisher Scientific, Pittsburgh, PA) through sonication. The mixture was then filtered to collect the PCA/SWNT aggregates, which were washed several times with methanol/DI H_2O and dispersed in DI H_2O. The sensor base was made by

printing wax ink (Xerox ColorQube 8880, Xerox, Norwalk, CT) onto a strip of Whatman 5 filter paper (GE Healthcare, Chicago, IL). The wax was melted at 170°C for 5 min to create hydrophobic boundaries throughout the thickness of the paper. A second layer of wax was printed but not melted to ensure sufficient hydrophobicity at the paper surface. The paper channels were placed on a glass frit with a vacuum (~80 kPa) underneath, and the PCA/SWNT dispersion was dropped onto the sensing channel to deposit the PCA/SWNTs. Source and drain electrodes were created by applying silver paste (Ted Pella Inc. Redding, CA) onto either end of the sensor. Anti-human serum albumin (anti-HSA) antibody (BiosPacific, Inc. Emeryville, CA) was immobilized on the SWNT channel using EDC/NHS chemistry. This was followed by quenching remaining active groups with 0.1 M ethanolamine (Fisher Scientific, Pittsburgh, PA) and blocking non-specific binding with 0.1 wt% Tween-20 (Bio-Rad, Hercules, CA). The dry initial resistance of the sensing channels after the functionalization, quenching, and blocking was 9.90 ± 0.31 kΩ.

The rest of the demonstration device consisted of a fluid-handling layer, which facilitated rapid, sequential delivery of a sample and wash buffer and waste pads that absorbed excess fluid as it passed through the sensor. Both fluid-handling and waste layers were constructed from Whatman 4 filter paper and cut out using the CO_2 laser. The device itself was constructed using a bottom-up approach. A strip of Uline tape was placed adhesive-side up onto a piece of thick, double-sided tape (Style-592, Intertape Polymer Group, Newport Beach, CA). This double-sided tape acted as a rigid support for the device. The waste pad was then attached to the Uline tape, followed by the sensor and the fluid-handling layer on top of that. Another piece of Uline tape was placed on top of the fluid

handling layer to seal together this three-layer sandwich. This top layer of tape had holes cut into it to allow addition of sample and wash buffer and to connect electrodes to the sensor for electrical measurement.

All electrical measurements were carried out using a potentiostat (model 600E, CH Instruments, Austin TX) as previously reported (Shen et al. 2019). Flat alligator clips were connected to the silver conductive pads. Electrical measurements were performed by measuring the I-V curve using linear sweep voltammetry (LSV) from -0.1 V to 0.1 V. The reciprocal of the slope of the curve was the resistance of the sensor. Real-time monitoring was done by amperometric monitoring of current vs. time with a source-drain bias set at 0.1 V

Devices were tested by first priming the chemiresistive sensor with 20 μL of 10 mM phosphate buffer (PB) (pH 7.4), which was added to the sample inlet. The buffer was allowed to wick through the sensor for 2 minutes. HSA solutions were prepared using PB, artificial urine (AU) and artificial saliva (AS). AU and AS formulations were adapted from previous works (Brooks and Keevil 1997; Tlili et al. 2010). Preparation of AU included the following: 170 mM urea, 90 mM KCl, 90 mM NaCl, 25 mM NH_4Cl, 7 mM creatinine, 7 mM K_2HPO_4, 7 mM KH_2PO_4, 2.5 mM $CaCl_2$, 2 mM $MgSO_4$, 2 mM $MnCl_2$, and 0.4 mM uric acid mixed together in deionized water with pH adjusted to 7.4. AS consisted of 0.6 g/L of Na_2HPO_4, 0.6 g/L of anhydrous $CaCl_2$, 0.4 g/L of KCl, 0.4 g/L of NaCl, 4 g/L of mucin and 4 g/L of urea dissolved in DI H_2O with pH adjusted to 7.4. Then, 20 μL of HSA (Sigma-Aldrich, St. Louis, MO) sample (prepared at varying concentrations in PB, AU, or AS) and another 60 μL of 10 mM PB were simultaneously added to the

sample and wash buffer inlets, respectively. Measurements were taken until the output current achieved steady state.

2.3 Results and Discussion

2.3.1 Groove Fabrication

Fig. 2.1b shows SEM images of grooves that were etched at different speeds. As speed decreased, the laser burned away more material and made a deeper groove. The slowest speed tested (20%) allowed the laser to cut through the paper, creating a slit. A speed setting of 40% created characteristic holes in the paper, spaced evenly throughout the length of the groove. The laser module was driven by stepper motors, which cause the module to move in a series of 'steps' rather than continuously. Therefore, the laser spends slightly more time at a region that corresponds with the end of a step, burning more material there. This phenomenon was seen to a lesser extent in grooves etched at faster speeds. A secondary contribution could also come from the non-homogenous fiber density in the paper. Certain regions may have more densely packed fibers than others due to variability in the manufacturing process (Alava and Niskanen 2006).

The second row of Fig. 2.1b shows perspective SEM images of grooves that were etched at different speeds. Grooves etched at 20% have a trapezoidal cross-section. Since the focus of the laser was on the paper surface, power density was reduced at any point below, causing the laser to burn through less material. Grooves etched at the other speeds exhibited roughly v-shaped cross-sections of varying depths. All grooves were ~175μm wide at opening.

2.3.2 Groove Characterization

The morphology of the laser-etched grooves was characterized by analyzing the depth of each groove relative to the thickness of the paper as well as mass loss caused by each groove. Measurements indicated that slits (20% speed) reduced the cross-sectional area of the paper by ~60% (Fig. B1a). Grooves etched at faster speeds reduced the cross-sectional area by lesser amounts. A linear relationship was observed between etching speed and cross-sectional area (Fig. B1c). Mass loss experiments determined that slits reduced the mass of the paper by roughly 15% (Fig. B2b). Again, a linear relation was observed between mass loss and etching speeds. More detailed information regarding these relationships can be found in Supplemental Figures B1 and B2.

2.3.3 Vertical Wicking – No Tape & Uline Taped Channels

Fig. 2.2 shows distance vs. time plots for untaped channels as well as channels sealed on various sides using Uline S-423 Industrial Tape. This tape was chosen here because our lab has used it in the past to fabricate multilayer paper devices. With a thickness of only 50.8 μm, the tape was very easy to fold around edges/creases to seal different layers of paper together. Untaped grooves etched at all speeds created faster wicking channels compared to untreated paper with the fastest wicking occurring in channels etched at 20% speed (Fig. 2.2 No Tape). The grooves acted as macro capillaries with a lower flow resistance compared to the paper around it. This allowed fluid to wick outside the paper matrix and serve as a secondary fluid source above the waterline for the paper, resulting in faster overall wicking. Since a 20%-speed groove was etched completely

through the paper, it had the largest macro capillary, making it the fastest, which indicated that cutting a slit into the channel was the optimal way to speed up fluid delivery.

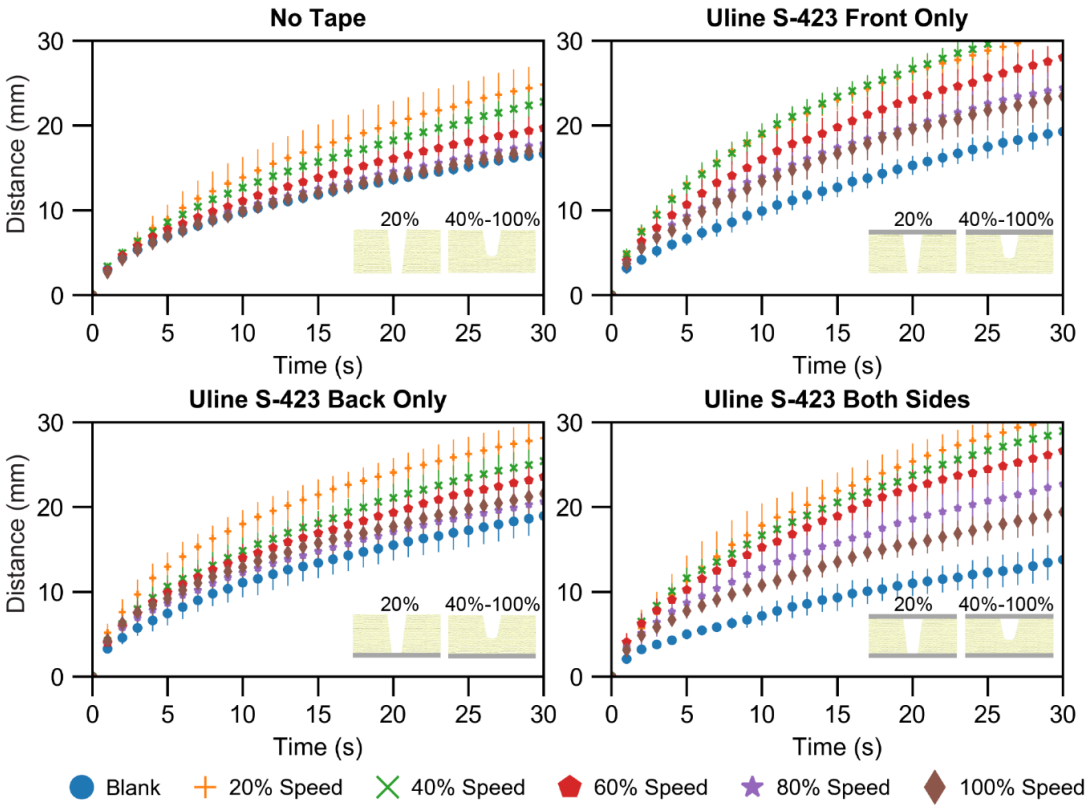

Fig. 2.2 Distance vs. time plots for grooves with different etching speeds without tape and taped in various configurations with Uline S-423 Industrial Tape. Insets show tape configurations relative to groove geometries. With or without tape, grooves etched at 20% wicked the fastest. Wicking performance was strongly dependent on which side of the channel was taped. Data presented as mean ± SD. N=10.

In general, the same trend was seen for taped channels. However, etched channels with tape were generally faster than their untaped counterparts. Moreover, wicking speeds seemed to depend on which side of the channel was sealed. When channels were sealed only on the front, grooves etched at all speeds wicked more quickly (Fig. 2.2 Uline S-423 Front Only). The tape provided extra surface area which increased contact forces between the liquid and the capillary. Without tape, the surrounding paper tends to

flex/swell during wicking, which can destabilize the capillary and slow fluid down. Since the tape was applied to the side that was etched, fluid inside the macro capillary in all groove types benefited from the extra surface area, which made all the etched channels faster. Regarding the 20%-speed grooves, taping the slit even on one side stabilizes the macro capillary in the center. On the other hand, sealing channels only on the back improved wicking in channels etched at all speeds but to a lesser extent (Fig. 2.2 Uline S-423 Back Only). Since grooves etched at faster speeds did not extend all the way through the paper for the entire groove length, there was less interaction between the fluid within the capillary and any tape on the back side. Thus, much smaller differences in wicking speeds were observed relative to the untaped channels. Applying tape to both sides had a similar effect to applying tape on the front side for channels etched at lower speeds (Fig. 2.2 Uline S-423 Both Sides). However, channels etched at faster speeds along with blank channels wicked somewhat slower. One possible reason was that sealing the paper on both sides blocks pores that lead to the surface of the paper. Without tape, fluid wicked along the outer surfaces of the paper, which had a lower flow resistance than the porous matrix of the paper. With the tape in place, all the fluid must flow within the paper, forcing it to wick more slowly.

2.3.4 Vertical Wicking – Sealed Channel Comparison

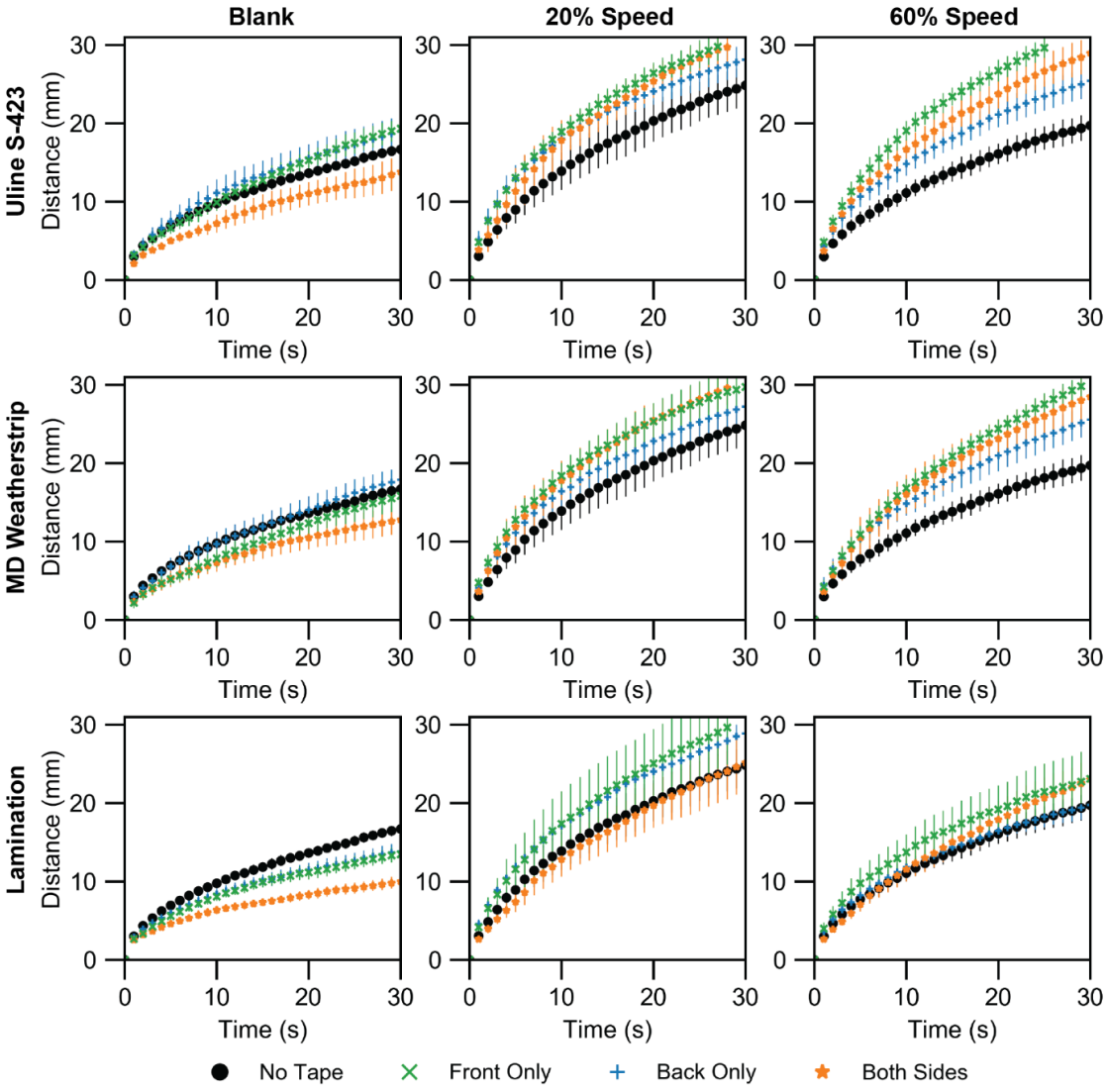

Fig. 2.3 Distance vs. time plots for grooves with different etching speeds without tape and taped in various configurations with various tapes. Wicking performance was strongly dependent on what type of tape was used to seal the channels. Data presented as mean ± SD. N=10.

Further analysis was conducted how sealing grooved channels with different types of tape/sealing would affect their wicking behavior. Preliminary tests were conducted using 3M Heavy Duty packing tape (Fig. C1). However, the tape was very susceptible to lifting off when the paper beneath it was wet, causing a great deal of variability. We repeated experiments with tapes that were more fluid resistant. In addition to the Uline tape, the MD Weatherstrip tape was selected as it was typically used to seal window frames to protect against moisture. Additionally, lamination has been commonly used to protect documents against liquid and has been used to make paper-based devices in the past (Ota et al. 2018). Both the Uline and MD tapes were slightly hydrophobic (contact angles 109° and 106°, respectively) while the lamination sheet was weakly hydrophilic (83°) (Fig. D1). Fig. 2.3 shows distance vs. time plots for all three sealing methods for blank, grooved etched at 20% speed and 60% speed. The Uline and MD tapes followed a similar trend. However, laminated channels were much slower, despite the lamination sheet having a more hydrophilic surface. Lamination was accomplished by heating up the laminating sheet and applying force to press it onto the paper. It appeared that the adhesive on the lamination sheet melted and seeped into the paper, blocking some pores. This slowdown was dramatic enough that 20%-speed groove that was laminated on both sides was no faster than its untaped counterpart (Fig. 2.3).

The theoretical capillary rise for through-cut grooves of different widths (taped and untaped) is plotted in Fig. E1a. This was done by assuming that the grooves had a capillary with a rectangular cross section and the walls were impermeable. This simple capillary model suggests that laminated channels should have the highest capillary rise,

due to the relative hydrophilicity of the laminate sheets and the extra surface area fluid can interact with. This implies that these channels should wick the fastest. However, as described above, laminated channels were slowest among the sealed channels and even slower than untaped channels in certain configurations. Moreover, the Uline and MD tapes should theoretically be the slowest, as the hydrophobicity of the adhesive would impede the rise of fluid within the capillary. Wicking data showed the opposite trend. Channels sealed with these tapes were generally faster than laminated channels. Additionally, the model suggests that a smaller capillary will have a higher capillary rise and should wick more quickly. However, we found that etching completely through the paper (20%-speed grooves), which created the largest macro capillary, was in fact the fastest. This discrepancy between the model and experimental results is mainly because the simple capillary model did not consider transport of fluid between the groove and surrounding paper pores. These pores continuously draw fluid out of the groove as it is wicking along the channel. Since shallower grooves have more paper surrounding them, they are presumably losing more liquid and thus rise more slowly.

2.3.5 Vertical Wicking – Channels with Wider Grooves

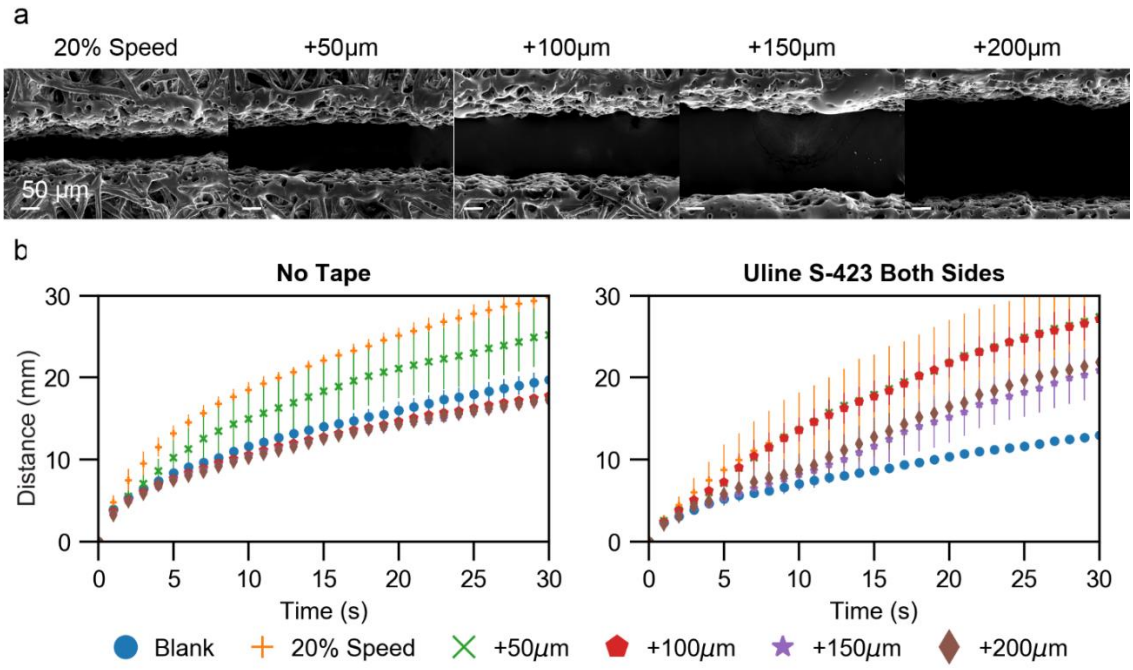

Fig. 2.4 Characterization of wide groove channels. (a) SEM images of 'wide' grooves that were etched by cutting rectangles in the paper channel with the CO_2 laser. The '20% Speed' groove was the original groove cut using a straight line, while the wider grooves were designed using rectangles of specified widths. The scale bar was 50µm. (b) Distance vs. time plots for wide grooves in untaped and taped configurations. Data presented as mean ± SD. N=5.

Having observed that cutting a slit in the paper created the fastest wicking channels (Fig. 2.2), our next goal was to determine the optimal geometry that would create the fastest channels. We decided to expand the width of the groove, reasoning that a wider capillary would allow more fluid to wick in between the paper and thus make the channel faster. As discussed before, rectangles with different widths were used to create wider grooves. Fig. 2.4a shows SEM images of wider grooves and the width of the rectangles used to create them. The smooth edges presented on the +150µm and +200µm grooves were due to ash that has accumulated from the laser-etching process. The same 6-channel test strip design used previously (Fig. A1b) was used in these experiments, with the four

wider grooves compared to the original groove etched at 20% speed and a blank, unetched channel.

Distance vs. time plots in Fig. 2.4b show that the original 20%-speed groove wicked faster than any of wider grooves without tape. The theoretical capillary rise for through-cut grooves of different widths is plotted Fig. E1a. As the width of the groove increases, the theoretical height of the fluid in the capillary decreases. The weight of the fluid increases more quickly if the capillary is wider, canceling the surface tension force more quickly. Therefore, the liquid would rise to a lower height in wider capillaries, which explained why those channels wicked more slowly. For untaped channels, it appeared that very little fluid entered the capillary in the wider-groove channels, given their similarity to the blank channel. Without this meniscus in the center, the fluid wicked in two, narrower parallel strips of paper. The reduced cross-section of each strip resulted in slower wicking overall.

With regards to groove width, theory suggests that wider grooves should have a lower capillary rise (thus slower wicking speed in the channel) regardless of how the channels are sealed (Fig. E1a). While untaped channels behaved according to this trend, taped channels performed less predictably (Fig. 2.4b). The 20% speed, +50μm and +100μm channels wicked at roughly the same speed. Nonetheless, the original 20%-speed groove consistently wicked the fastest in both taped and untapped configurations, and hence used in the subsequent investigations.

2.3.6 Groove Pitch Optimization

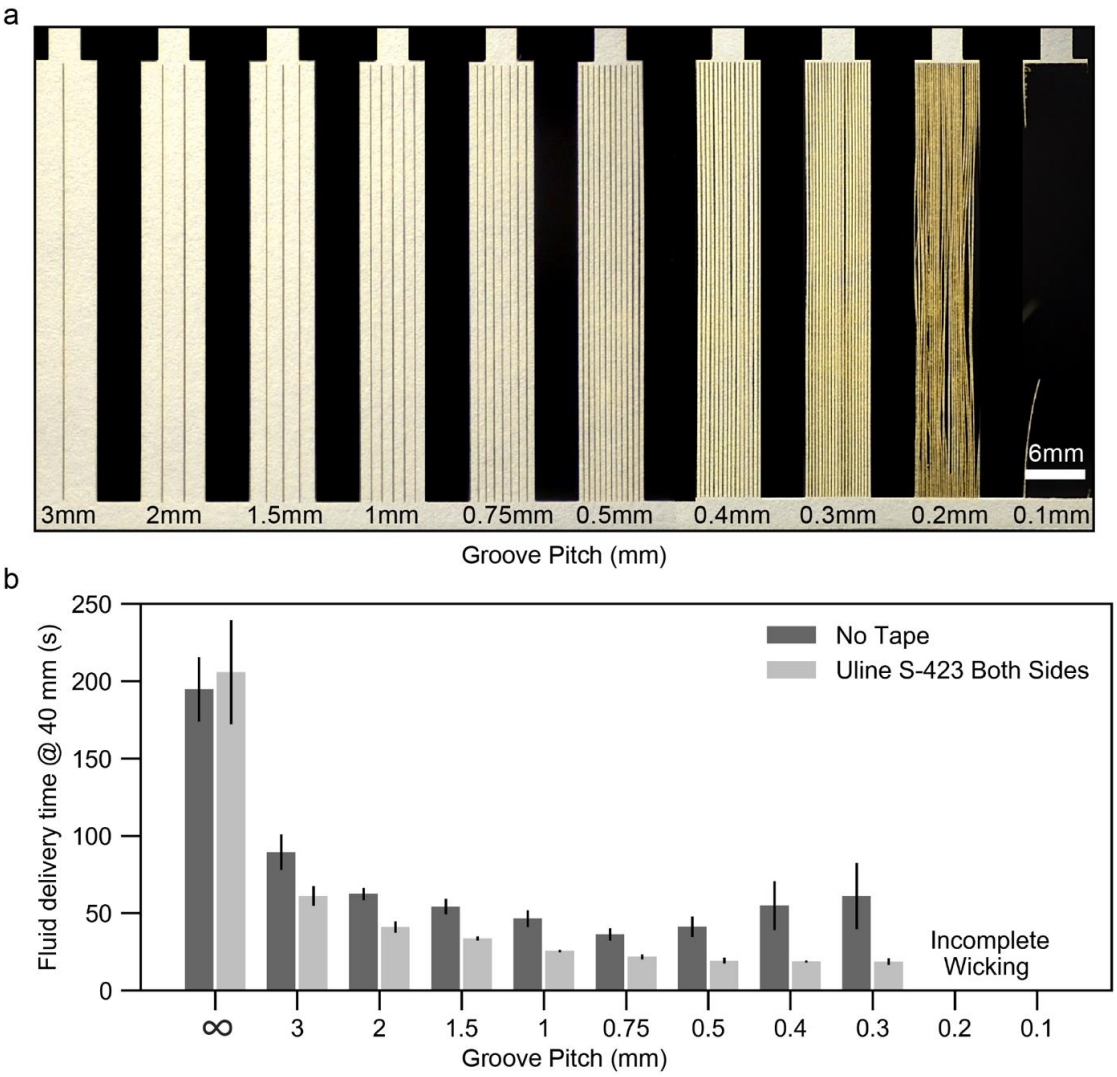

Fig. 2.5 Groove pitch optimization. (a) Image of test strip used to test groove densities. Channels were 6 mm wide × 40 mm tall. The distance at the bottom of each channel represents the gap between adjacent grooves. Below 0.3mm, the grooves are spaced within the resolution of the laser, which means that most of the paper was burned away. Scale bar was 6mm (b) Fluid delivery times for different groove densities in taped and untaped (Uline S-423) configurations. A groove pitch of 0.75mm was chosen as optimum. Data presented as mean ± SD. N=5.

Having established the optimal laser and geometry settings for a single groove, it was important to determine the ideal number of grooves to place in a single channel. Whatman 4 filter paper test strips with 6mm × 40mm channels were etched with grooves of varying pitches. Fig. 2.5a shows all the pitches that were explored. Rather than measuring the wicking front over time, we simply measured the time needed for the wicking front to reach the top of the channel (Fig. 2.5b).

As shown in Fig. 2.5b, untaped channels had an optimal pitch of 0.75mm. At smaller pitches, the excessive removal of material made the paper channel more unstable. There was excessive bending/buckling of the paper which disrupted wicking. The 0.2 mm and 0.1 mm pitch channels were destroyed and did not wick completely because the groove pitch was below the resolution of the laser. This means that the laser passed over the same region of paper multiple times and burnt it away. Taped channels did not yield an optimal value. Rather, there were diminishing gains in wicking speed as more grooves were added. As stated before, sealing the channels with tape helps stabilize the macro capillaries that formed inside each channel. A pitch of 0.75mm was selected as optimum due to negligible reduction in wicking time for grooves with higher densities. Additionally, having to etch fewer grooves reduced fabrication times. For both taped and untaped channels, it was interesting to note the dramatic reduction in wicking time when only a single groove is added to an unetched channel (~50% and ~70% respectively).

Our discovery that a through-cut groove has the fastest wicking speed matched the results of Liu *et al.*. (2017) who reached the same conclusion using different laser settings. However, while our experiments employed vertical wicking studies, they used

horizontal wicking. This means that the effect of gravity was negated in their experiments. This key difference may explain why their reported wicking speeds were much higher than ours (~59-fold improvement in avg. velocity vs ~8-fold). Our results show that gravity can play a significant role in wicking performance, as the rise of the fluid inside the macro capillary is slowed down by the weight of the fluid itself. Additionally, Liu *et al.*. achieved fastest wicking with a groove pitch of 0.375 mm (8 grooves in a 3mm channel) vs. 0.75 mm from our findings. Both groups found that taping channels can make them wick much faster. However, our findings show that the type of sealing tape employed played a significant role in wicking speeds (i.e., lamination vs. tape). Additionally, we found that certain tapes influence wicking differently based on what side of the channel is sealed (etch-side up or down).

2.3.7 Effect of Increased Viscosity

At room temperature (20°C), water (1.002 cP) (Korson et al. 1969) is less viscous compared to body fluids such as plasma (1.81 cP) (Lowe 2019) , saliva (2.45 cP), (Kusy and Schafer 1995) 20% hematocrit blood (3.8 cP), and 40% hematocrit blood (6.3 cP) (Rand et al. 1964). We repeated the vertical wicking experiments with 10%, 20% and 35% (v/v) concentrations of glycerol in DI H_2O to simulate the behavior of different biological fluids in our device. At an ambient temperature of 20°C, the dynamic viscosities of the three solutions were 1.38 cP, 1.98 cP and 3.76 cP, respectively (Cheng 2008; Volk and Kähler 2018). Additionally, since the dynamic viscosity of urine at 20°C is 1.09 cP (Elkins et al. 1974; Inman et al. 2013), its viscosity is comparable to that of water. For unetched channels, increasing the viscosity of the fluid reduced wicking speed (Fig. F1).

Even 10% glycerol reduced wicking speed by roughly half. However, wicking in grooved channels for each type of fluid was still significantly faster than their unetched counterparts. Wicking of the 35% glycerol solution was roughly twice as fast in the grooved channels compared to the unetched channels. These data show that grooves can dramatically increase wicking speeds even in viscous fluids.

2.3.8 Demo Device for Sequential Delivery and Analyte Detection

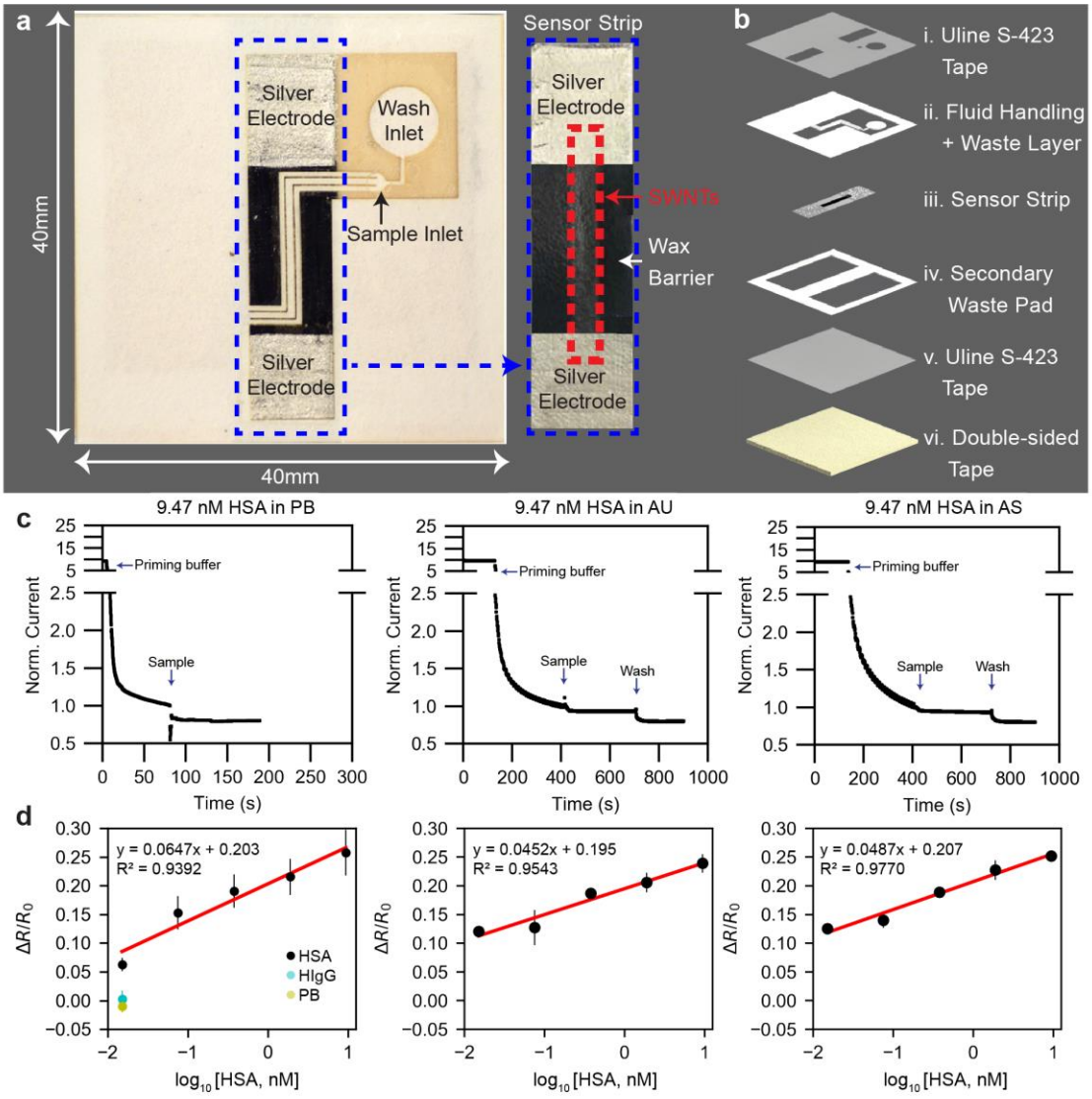

Fig. 2.6 Overall design and demonstration of the paper-based chemiresistive sensor device. (a) Images of the assembled multi-layer device (left) and the sensor strip inside (right). (b) Schematic of the multi-layer assembly, showing the fluid-handling layer, the chemiresistive sensor strip, and the other layers. (c) Current response for a fixed concentration of HSA (9.47 nM) in PB, AU and AS. Current is normalized with respect to the current after priming. Plots for both artificial biological fluids show the need for a washing step for signal recovery compared to PB. (d) Calibration plot of normalized change in resistance for each fluid type. Data presented as mean ± SD. N=3.

The optimization studies conducted on laser-etched grooves were used to design a fluid-handling mechanism for the chemiresistive paper-based sensor. The main goal of the fluid-handing mechanism was to sequentially deliver a sample and wash buffer to the chemiresistive sensor without any user intervention after initial depositions of fluids. In our previous report (Shen et al. 2019), both the sample and wash buffer were manually applied by pipet and removed by vacuum in sequence, requiring substantial user intervention. In addition, a vacuum source might not be readily available in resource-limited or in-field settings.

As shown in Fig. 2.6a, the location of the sample inlet provided the liquid with two possible directions to wick, either towards the etched channel to the sensor or towards a narrow channel to the wash buffer inlet. Because the grooved channel had a much lower resistance to flow, almost all the sample wicked in that direction. The grooved channel rapidly delivered the sample across the surface of the chemiresistive sensor that was positioned directly underneath. Additionally, since the grooves were slits, they allowed bulk fluid to directly contact the sensor, improving mass-transfer kinetics and reducing time required for stable signals. A secondary waste pad (Fig. 2.6b iv) sit directly below the sensor and absorbed any fluid that passed through it, reducing accumulation of ‘depleted’ sample fluid at the sensor surface. Excess sample also wicked onto the waste-pad region at the end of the grooved channel. Since the channel is presaturated with fluid, the wash buffer will not be able to wick until all the fluid in the sample inlet was depleted. Once the sample inlet was empty, the wash buffer wicked towards the sensor. Fig. G1 shows a time-lapse of the aforementioned sequential delivery step.

Since the SWNT chemiresistor sensor is highly sensitive to its environment, priming buffer was needed to fully moisturize the sensor before sample was introduced. The assembled devices showed a stable current around 10 μA with a source-drain voltage of 0.1V, because of its initial dry resistance of 9.9 kΩ. However, the current decreased significantly upon the addition of the priming buffer (20 μL 10 mM PB, pH 7.4) due to a large addition of water molecules onto the chemiresistor (Fig. 2.6c). Water molecules in the priming buffer n-doped the p-typed SWNTs and thus caused the observed decrease in the current through a dramatic increase in the resistance (Han et al. 2012; Shen et al. 2019; Shen et al. 2020). As shown in Fig. 2.6c, sample added after the priming process flattened the baseline current. Normalization based on the primed baseline was an essential step for reading the electrical responses. Normalized current was defined as the ratio of the raw current (I) and the current after the priming process (I_p). As shown in Fig. 6c, the normalized current was, by definition, at 1.0 at the point of sample arrival and decreased as more HSA sample was delivered to the sensor. In PB at pH 7.4, HSA molecules carried a net negative charge and were specifically bound to the anti-HSA. The binding events transferred charge to the semiconducting SWNTs. The SWNT chemiresistive sensor responded to the charge change at the sensor's surface due to the dominating effect of electrostatic gating (Shen et al. 2019). Fig S9 contains current vs. time plots for different concentrations of HSA in PB and controls.

A linear calibration curve with a satisfactory sensitivity and specificity was obtained over a wide range between 0.015 nM to 9.47 nM. As shown in Fig. 2.6d, the calibration curves were graphed as $\triangle R/R_0$ versus Log_{10}[HSA, nM], where ΔR was the

difference between the steady-state resistance R of the sensor after sample incubation and wash and the resistance R_0 after the sensor was primed (before sample addition). The response was linear with a 6.47% increase in the resistance per Log_{10}[HSA, nM]. Controls were tested by adding the same volume of PB or a non-target protein (9.47 nM human immunoglobin G (HIgG) in 10 mM PB, pH 7.4). PB alone introduced a -1.01±1.1% change after normalization, while the non-target crosstalk control (HIgG) resulted in only a 0.289±1.4% change. By comparing the responses from the PB blank ($\triangle R/R_0$±3SD) and the responses from 15 pM HSA in PB ($\triangle R/R_0$±SD), the lowest detectable concentration of HSA in PB was 15 pM based on S/N ratio of 3 ($p=0.023<0.05$). This figure is superior to traditional HSA biosensor LODs in the milligram per milliliter or micromolar range (Choi et al. 2004; Aliño and Yang 2011). These results indicated the high sensitivity and specificity of the biosensor.

Furthermore, to mimic the detection of HSA in real samples, we challenged the device with HSA samples in complex matrices, such as AU and AS. Due to the elevated level of dissolved salts in the AU and AS, the local ionic strength near the sensor surface was high and therefore led to a minimal Debye length. Thus, it was necessary to use PB washes to dilute the local ionic solution and recover the electrical responses corresponding to the affinity-based binding between the antigen and antibody (Kaisti 2017; Shen et al. 2020). As shown in Fig. 2.6c, after PB priming, the HSA sample in AU or AS matrix gave a reduced response (less decrease in the current) compared to that in HSA samples in PB. A 60 µL PB wash was used to recover the responses (more decrease in the current). The possible mechanism was that the continuous inflow of PB with low ionic strength washed

the salts to the waste layer/pad and diluted the local matrix, which resulted in a larger Debye length to overturn the charge screening and thus recovered the responses (Kaisti 2017; Shen et al. 2020). These observations show that a well-controlled fluid delay is an essential function for a paper-based microfluidic biosensor for biomarkers in more complex, real-life samples. Figs. G2-G4 contain current vs. time plots for different concentrations of HSA in AU and AS, respectively. The viscosity of the biological samples can also affect their wicking behavior in paper (Fig. F1).

Compared with our previous work (Shen et al. 2019), in which the samples and wash buffers were manually added by pipet and removed by vacuum filtration, the device presented here was ~70% as sensitive with a satisfactory lowest detectable limit of 15 pM HSA in PB. The lower sensitivity for HSA in PB in the current device compared to our prior work is likely because the latter utilized the vacuum filtration to very effectively remove excess sample and wash solution from the sensor surface after incubations. The current device also gave high sensitivities to HSA in AU and AS. The responses were linear with a 4.52 % and 4.87% increase in the resistance per Log10[HSA, nM] for AU and AS, respectively. However, devices tested in AU/AS had a ~25% to 30% lower sensitivity compared to devices tested with PB only. The lower sensitivities for HSA in AU and AS were likely because the washing process is even more critical for samples containing ions and other interfering substances. It is expected that the sensitivities can be improved with the revision of the device design to allow for a larger wash buffer volume, which is currently limited to 60 μL. Nevertheless, the sensor still maintained good sensitivity and specificity to HSA. Furthermore, with the new fluid-handling architecture, external devices

such as a vacuum filter and a vacuum pump are no longer necessary. The fluid-handling layer was able to semi-automatically deliver the fluids sequentially to the SWNT chemiresistor, thus eliminating the need for specialized personnel to use it.

2.4 Conclusion

The above work detailed the use of laser-etched grooves to accelerate wicking speeds on paper. Optimization studies were conducted to determine ideal fabrication parameters. It was discovered that the fastest wicking channels were created by simply cutting a slit through the paper. The slit acted as a macro capillary, letting fluid wick outside the paper matrix. The exact mechanisms behind the observed behaviors are not yet well understood and require further investigation. Additional studies found that making the slit wider did not improve wicking performance but sealing the channels did improve wicking speeds. However, the type of adhesive used drastically influences wicking speeds; certain adhesives can slow down the channels, counteracting the enhancement provided by the sealing. An ideal groove pitch was found that balanced the number of macro capillaries in the channel with the reduced structural integrity of the paper due to excess removal of material. As a proof of concept, we successfully demonstrated the utility of laser-etched grooves by enabling rapid, semi-automated sequential fluid delivery for a chemiresistive SWNT paper-based sensor targeting HSA in PB, AU, and AS. Furthermore, it is expected that by combining etching with other fluid control strategies, such as delay shunts or multilayer channels, a much higher degree of wicking control can be available for more complicated point-of-care devices.

2.5 References

Alava, M., Niskanen, K., 2006. Reports on progress in physics 69, 669.

Aliño, V.J., Yang, K.-L., 2011. Analyst 136, 3307-3313.

Apilux, A., Ukita, Y., Chikae, M., Chailapakul, O., Takamura, Y., 2013. Lab on a Chip 13, 126-135.

Brooks, T., Keevil, C., 1997. Letters in applied microbiology 24, 203-206.

Camplisson, C.K., Schilling, K.M., Pedrotti, W.L., Stone, H.A., Martinez, A.W., 2015. Lab on a Chip 15, 4461-4466.

Castro, C., Rosillo, C., Tsutsui, H., 2017. Microfluidics and Nanofluidics 21, 21.

Channon, R.B., Nguyen, M.P., Scorzelli, A.G., Henry, E.M., Volckens, J., Dandy, D.S., Henry, C.S., 2018. Lab on a Chip 18, 793-802.

Cheng, N.-S., 2008. Ind Eng Chem Res 47, 3285-3288.

Choi, S., Choi, E.Y., Kim, H.S., Oh, S.W., 2004. Clinical chemistry 50, 1052-1055.

da Silva, E.T., Santhiago, M., de Souza, F.R., Coltro, W.K., Kubota, L.T., 2015. Lab on a Chip 15, 1651-1655.

Dieterich, K., 1902. US Patent, 691249, USA.

Dungchai, W., Chailapakul, O., Henry, C.S., 2010. Analytica chimica acta 674, 227-233.

Elizalde, E., Urteaga, R., Berli, C.L.A., 2015. Lab on a Chip 15, 2173-2180.

Elkins, H.B., Pagnotto, L.D., Smith, H.L., 1974. American Industrial Hygiene Association Journal 35, 559-565.

Fu, E., Lutz, B., Kauffman, P., Yager, P., 2010. Lab on a Chip 10, 918-920.

Fu, E., Ramsey, S.A., Kauffman, P., Lutz, B., Yager, P., 2011. Microfluidics and nanofluidics 10, 29-35.

Giokas, D.L., Tsogas, G.Z., Vlessidis, A.G., 2014. Analytical chemistry 86, 6202-6207.

Han, J.-W., Kim, B., Li, J., Meyyappan, M., 2012. The Journal of Physical Chemistry C 116, 22094-22097.

Hossain, S.Z., Brennan, J.D., 2011. Analytical chemistry 83, 8772-8778.

Inman, B.A., Etienne, W., Rubin, R., Owusu, R.A., Oliveira, T.R., Rodriques, D.B., Maccarini, P.F., Stauffer, P.R., Mashal, A., Dewhirst, M.W., 2013. International Journal of Hyperthermia 29, 206-210.

Jahanshahi-Anbuhi, S., Henry, A., Leung, V., Sicard, C., Pennings, K., Pelton, R., Brennan, J.D., Filipe, C.D., 2014. Lab on a Chip 14, 229-236.

Kaisti, M., 2017. Biosensors and Bioelectronics 98, 437-448.

Kalish, B., Tan, M.K., Tsutsui, H., 2020. Micromachines 11, 773.

Korson, L., Drost-Hansen, W., Millero, F.J., 1969. The Journal of Physical Chemistry 73, 34-39.

Kusy, R., Schafer, D., 1995. Journal of Materials Science: Materials in Medicine 6, 385-389.

Li, H., Steckl, A.J., 2018. Analytical chemistry 91, 352-371.

Liu, Q., Xu, C., Liang, H., 2017. Talanta 175, 289-296.

Lowe, G.D., 2019. Crc Press.

Martinez, A.W., Phillips, S.T., Butte, M.J., Whitesides, G.M., 2007. Angewandte Chemie International Edition 46, 1318-1320.

Modha, S., Shen, Y., Chamouni, H., Mulchandani, A., Tsutsui, H., 2021. Biosensors and Bioelectronics 180, 113090.

Ota, R., Yamada, K., Suzuki, K., Citterio, D., 2018. Analyst 143, 643-653.

Park, J., Park, J.-K., 2017. Sensors and Actuators B: Chemical 246, 1049-1055.

Rand, P.W., Lacombe, E., Hunt, H.E., Austin, W.H., 1964. Journal of Applied Physiology 19, 117-122.

Ratnarathorn, N., Chailapakul, O., Henry, C.S., Dungchai, W., 2012. Talanta 99, 552-557.

Renault, C., Li, X., Fosdick, S.E., Crooks, R.M., 2013. Analytical chemistry 85, 7976-7979.

Shen, Y., Modha, S., Tsutsui, H., Mulchandani, A., 2020. Biosensors and Bioelectronics, 112721.

Shen, Y., Tran, T.-T., Modha, S., Tsutsui, H., Mulchandani, A., 2019. Biosensors and Bioelectronics 130, 367-373.

Shin, J.-H., Lee, G.-J., Kim, W., Choi, S., 2016. Sensors and Actuators B: Chemical 230, 380-387.

Shin, J.H., Park, J., Kim, S.H., Park, J.-K., 2014. Biomicrofluidics 8, 054121.

Tlili, C., Cella, L.N., Myung, N.V., Shetty, V., Mulchandani, A., 2010. Analyst 135, 2637-2642.

Toley, B.J., McKenzie, B., Liang, T., Buser, J.R., Yager, P., Fu, E., 2013. Analytical chemistry 85, 11545-11552.

Verma, M.S., Tsaloglou, M.-N., Sisley, T., Christodouleas, D., Chen, A., Milette, J., Whitesides, G.M., 2018. Biosensors and Bioelectronics 99, 77-84.

Villamizar, R.A., Maroto, A., Rius, F.X., Inza, I., Figueras, M.J., 2008. Biosensors and Bioelectronics 24, 279-283.

Volk, A., Kähler, C.J., 2018. Experiments in Fluids 59, 75.

Yamada, K., Kim, C.-T., Kim, J.-H., Chung, J.-H., Lee, H.G., Jun, S., 2014. PLoS One 9, e105767.

Yetisen, A.K., Akram, M.S., Lowe, C.R., 2013. Lab Chip 13, 2210-2251.

3. SIMULATING FLOW IN PAPER CHANNELS

3.1 Introduction

Fluid control for paper devices has been achieved in a trial-and-error fashion, where researchers fabricated devices with different control strategies until a suitable approach is found. If the behavior of fluid in paper were better understood, flow control strategies could be developed straight from theoretical models, rather than lengthy experimental work. As paper-based devices become more sophisticated, more accurate models of fluid behavior would accelerate device development and save costs. Additionally, once an accurate theoretical framework is obtained, much of the testing could be done using *in-silico* models. Paper is produced from an aqueous suspension of cellulose fibers primarily derived from wood and cotton. The manufacturing process involves drawing these aqueous suspensions through a sieve, pressing the remaining product, drying it and treating it with different chemicals. This produces a material with an intricate, interconnected network of cellulose fibers. This property makes accurate calculation of imbibition especially difficult. In this section, we review different theoretical approaches that have been developed for modeling flow in paper/porous media. Additionally, we develop an *in-silico* model in MATLAB using Richards Equation that can predict wicking behavior in untreated paper as well as grooved channels.

3.2 Imbibition Models for Paper

3.2.1 Darcy's Law

Fluid imbibition into paper is a complex process governed by a highly coupled system of length and time-scaled parameters. In the 19th century, Darcy found that flow in the macroscopic regime is proportional to the pressure gradient applied across a porous substrate. This is analytically presented as,

$$v = -\frac{K}{\mu}\nabla p\,, \tag{1}$$

where v is the average liquid velocity, K is the permeability of the substrate (ease of fluid penetration), μ is the dynamic viscosity, and ∇p is the pressure gradient across the porous substrate (Darcy 1856) . This relationship is known today as Darcy's Law, and describes flow in a generic porous medium of any kind. This model assumes that flow within a porous medium is driven solely by pressure gradient. Additionally, the model assumes that flow is laminar, steady and a constant material permeability. Darcy's Law does not consider the geometry of the medium nor the effects of evaporation. This model is used extensively in the field of hydrogeology but is less common in the paper-microfluidics field.

3.2.2 Lucas-Washburn Equation

The most common way to model imbibition in paper is by treating it as a bundle of parallel, rigid capillary tubes of uniform size with an infinite liquid reservoir at the inlet. Movement of the liquid front is governed by a single representative capillary tube with four acting forces: the suction force created by the interfacial pressure difference at the meniscus, the viscous force, the gravitational force, and the inertial force.

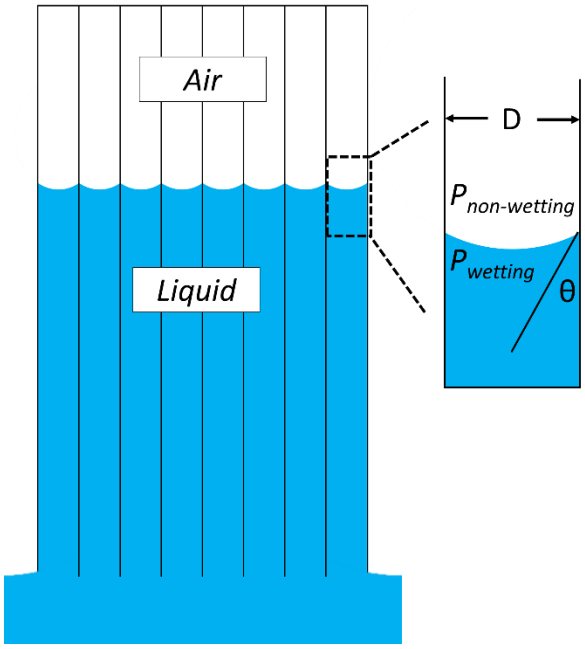

Fig. 3.1 Schematic representative of a porous substrate using a bundle of capillary tubes.

As shown in Fig. 3.1, a capillary tube of diameter D contains two immiscible fluids (liquid and air) immersed in an infinite reservoir at ambient pressure. A meniscus is formed at the interface, and combined with surface tension γ, creates a pressure difference denoted by the Young-Laplace equation as the capillary pressure,

$$P = \frac{4\gamma cos\theta}{D}, \tag{2}$$

where θ is the contact angle.

The momentum balance of the capillary front yields Eq. 3 (Zhmud et al. 2000; Fries and Dreyer 2008),

$$\rho \frac{d}{dt}\left(h\frac{dh}{dt}\right) = \frac{4\gamma cos\theta}{D} - \frac{32\mu}{D^2} h\frac{dh}{dt} - \rho g h, \tag{3}$$

where ρ is the liquid density, and h is the height of the meniscus. The left side of the equation is the inertial force while the right side is the capillary pressure, viscous force

represented by Hagen-Poiseuille flow, and the gravitational force. An analytical solution to Eq. 3 is not possible, though numerical methods such as the Runge-Kutta method have previously been used (Szekely et al. 1971). The gravitational effect generally plays a negligible role in short-distance imbibition, being within 10% of the final equilibrium height (Fries and Dreyer 2008). The influence of the inertial term has been investigated by Rideal (Rideal 1922) and Bosanquet (Bosanquet 1923) who determined that inertia is only important in early imbibition where distance is linearly proportional to time or when the capillary is large. Hence, the inertial and gravity terms are often ignored. Therefore, Eq. 3 becomes,

$$\frac{4\gamma cos\theta}{D} = \frac{32\mu}{D^2} h \frac{dh}{dt}, \tag{4}$$

where the capillary pressure is balanced by the viscous force. Solving Eq. 4 with initial conditions $h(t=0) = 0$ gives the widely used Lucas-Washburn (LW) equation (Lucas 1918; Washburn 1921),

$$h = \sqrt{\frac{D\gamma cos\theta}{4\mu} t}, \tag{5}$$

where the wicking distance is proportional to the square root of time. The LW model is widely used due to its simplicity and generally accurate representation of flow behavior (Masoodi and Pillai 2010).

3.2.3 Modifications to Darcy's Law and LW Equation

Both Darcy's Law and the LW equation make simplifying assumptions that reduce their applicability. The LW equation assumes a constant capillary diameter throughout the length of the paper. Additionally, the LW model does not consider changes

in channel geometry or the effects of evaporation. Darcy's law also does not consider both these factors. Therefore, several modifications have been proposed to make both models more accurate.

3.2.3.1 Effective Diameter

Eq. 5 represents wicking in a perfect capillary tube, which is obviously not the case in porous materials. Therefore, a slight modification is needed.

$$\frac{4\gamma cos\theta}{D} = \frac{32\mu}{{D_h}^2} h \frac{dh}{dt} \tag{6}$$

In Eq. 6, D is the static diameter of the pore and D_h is the hydrodynamic diameter of the represented capillary tube (Fries et al. 2008; Masoodi and Pillai 2010). Solving Eq. 6 produces,

$$h = \sqrt{\frac{D_e \gamma cos\theta}{4\mu} t}, \tag{7}$$

where D_e is the effective diameter given by $D_e = D_h^2/D$. This substitution has been proposed to improve accuracy when modeling polymer wicks (Masoodi et al. 2007) and metal weaves (Fries et al. 2008). For paper, the static and hydrodynamic diameters are difficult to obtain due to the complex material structure. Therefore, the effective diameter has no physical significance apart from measuring the ease of liquid penetration.

The form of the LW equation shown in Eq. 7 is the most widely recognized model for characterizing imbibition in paper. It has been used to characterize one-dimensional imbibition numerous times (Lutz et al. 2013; Bohm et al. 2014; Jafry et al. 2016) and has also been used as the basis for modeling two-dimensional flows within paper-like materials (Fu et al. 2011; Benner and Petsev 2013; Shou et al. 2014; Elizalde et

al. 2015).

The question of effective diameter becomes very important for multi-layer paper devices. These are devices comprised of multiple layers of paper with a hollow, macrocapillary in between the paper layers. Channon *et al.* have derived an equation describing wicking in multilayer devices, where the capillary pressure is balanced by the viscous dissipation inside the paper (Channon et al. 2019).

$$t = \frac{4ct^2}{(2a+1)\left(\sqrt{4ct + a^2h^2} - ah\right)^2} + \beta\left[\frac{t}{(a+1)\left(\sqrt{4ct + a^2h^2} - ah\right)}\right]^{1/(a+1)}, \quad (8)$$

where $a = 3t_h^2/{t_g}^2$, $c = \gamma t_h^2 \cos^2\theta/\mu t_g$, t_h = paper thickness, t_g = half gap height, h = wicking distance, β = constant of integration. The group suggested that the thickness of the paper around the macrocapillary has a negligible effect on imbibition velocity.

Cummins *et al.* developed a transport model that incorporated different pore sizes present within the paper matrix (Cummins et al. 2017). Using mercury porosimetery, they determined the range of pore sizes present within Whatman 1 filter paper and applied Darcy's law to ten equally spaced pore radii in that range (Fig. 3.2). While their model matched well with experimental data, the team observed that assuming complete saturation behind the wetting front was inaccurate.

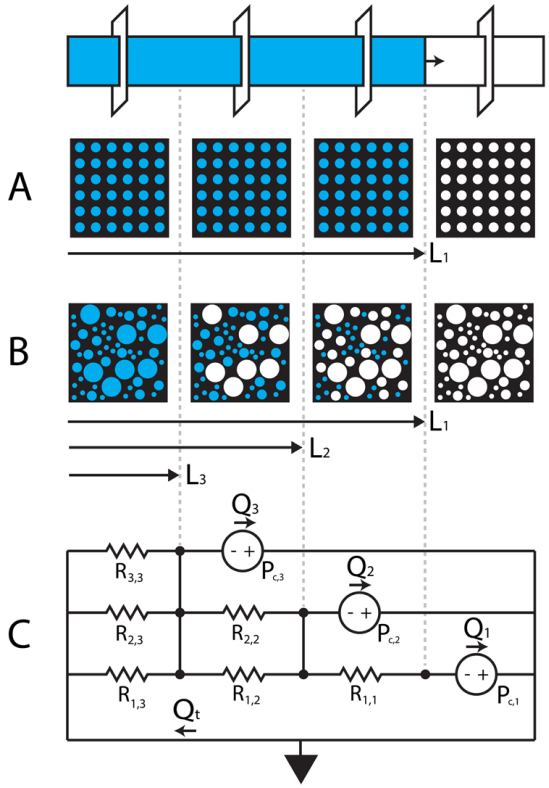

Fig. 3.2 Flow through a material with uniform and different-sized pores. (A) Models that use uniform pore size (LW etc.) assume complete saturation behind the wicking front. (B, C) The model developed by Cummins *et al.* postulates a position-dependent saturation. The group implemented an electrical circuit model, where pore size is modeled as the resistance and volumetric flow rate modeled as current. Adapted with permission from ((Cummins et al. 2017) https://pubs.acs.org/doi/10.1021/acs.analchem.6b04717). Copyright (2017) American Chemical Society. Further permissions related to the material excerpted should be directed to the ACS

$$Q_1 = \frac{dL_1}{dt} A_1 \phi = \frac{P_1 - P_2}{R_{1,1}} \tag{9a}$$

$$Q_2 = \frac{dL_2}{dt} A_2 \phi = \frac{P_2 - P_3}{\left(\Sigma_1^2 R_{i,2}^{-1}\right)^{-1}} - Q_1 \tag{9b}$$

$$Q_3 = \frac{dL_3}{dt} A_3 \phi = \frac{P_3}{\left(\Sigma_1^3 R_{i,3}^{-1}\right)^{-1}} - \sum_{i=1}^{2} Q_i \tag{9c}$$

Eq. 9a-c are for a porous medium with three major pore sizes, where L is the position of the wetting front at a specific time, R is the pore radius, Q is the volumetric flow rate, P is the capillary pressure for a specific pore radius, A is the cross-sectional area of the pore and ϕ is the porosity of the medium.

A similar study conducted by Ghassemzadeh et al., who developed a model for coating fluid onto paper. Their model also treated paper as a complex structure with multiple pore sizes. For their simulations, the group determined average radii values from statistical distributions (Ghassemzadeh et al. 2001).

3.2.3.2 Permeability

Permeability represents the ease of fluid penetration, which is generally a material-specific property. In relating the interstitial velocity (Hagen-Poiseuille flow) of the capillary to the superficial velocity (Darcy), the relationship,

$$\frac{32}{D_e^2} = \frac{\phi}{K}, \tag{10}$$

gives the capillary model permeability (Masoodi and Pillai 2010), where ϕ is the porosity and K is the effective permeability. This can be substituted into Eq. 7 to produce an alternative form of the Lucas-Washburn equation,

$$h = \sqrt{\left(\frac{2K}{\phi}\right)^{1/2} \frac{\gamma cos\theta}{\mu} t} \tag{11}$$

Aside from the permeability relation of Eq. 10, other permeability relationships have been proposed, generally in the form,

$$K = \epsilon D_e^2 , \tag{12}$$

where ϵ is a function of the substrate geometry (Kao and Hunt 1996).

One of these permeability relationships, the Kozeny-Carman equation, has been frequently used (Wyllie and Gregory 1955; Xu and Yu 2008) even though it was developed for a pack bed of solids. For paper, permeability relations developed for fiber beds are more appropriate. Permeability relations developed by (Gebart 1992), (Van der Westhuizen and Du Plessis 1996), and.(Nabovati et al. 2009) are widely used in the analysis of woven textiles (summarized in Table 1). More recently, Qin et al. developed a novel permeability model by using a Venturi tube to measure gas flow rate through porous media (Qin et al. 2018). Additionally, Xu et al. developed a permeability model that uses fractal characteristics of pore-scale structure (Xu et al. 2013). However, using these relationships is challenging for paper-like materials as fiber properties can vary due to humidity and the imbibing fluid. Nevertheless, studies investigating permeability relationships are undoubtedly beneficial.

Table 1 Selected permeability relations.

Permeability Relation	Developed for	Reference
$K = d^2 \frac{\phi^3}{180(1-\phi)^2}$	Pack bed of solids	(Wyllie and Gregory 1955; Xu and Yu 2008)
$K = \frac{d^2}{4} C \left(\sqrt{\frac{1-\phi_c}{1-\phi} - 1} \right)^{5/2}$	Close-packed fibers	(Gebart 1992)
$K = \frac{d^2}{4} \pi\phi \left(\frac{\left(1-\sqrt{1-\phi}\right)^2}{24(1-\phi)^{3/2}} \right)$	Random unidirectional fiber beds	(Van der Westhuizen and Du Plessis 1996)
$K = \frac{d^2}{4} C_1 \left(\sqrt{\frac{1-\phi_C}{1-\phi} - 1} \right)^{C_2}$	3D random fiber network	(Nabovati et al. 2009)
$K = \left[\frac{1}{\mu_g u} \left(\frac{\Delta P}{h} - \rho_g B u^2 \right) \right]^{-1}$	Highly porous media	(Qin et al. 2018)
$K = \frac{G}{2^{1-D_T}} \frac{\phi}{A_p h_0^{D_T-1}} \frac{D_f}{3 - D_f + D_T} R_{max}^{3+D_T}$	Saturated porous media	(Xu et al. 2013)

3.2.3.3 Evaporation and Humidity

The significance of evaporation has motivated researchers to incorporate its inhibitory effects within the models they use (Mendez et al. 2010; Jahanshahi-Anbuhi et al. 2014; Camplisson et al. 2015; Castro et al. 2017). Most studies have adopted the model developed by Fries *et al.* (Fries et al. 2008). This model incorporates a uniform constant evaporation flux from the paper surface. The derived model, neglecting gravity, results in,

$$h = \sqrt{\frac{a}{b} - \frac{a}{b} e^{-2bt}} \text{ with } a = \frac{4\gamma cos\theta}{\phi\mu} \frac{K}{D} \text{ and } b = \frac{\dot{m}_e (W + t_h)}{\rho W t_h \phi}, \quad (13)$$

where $\dot{m}_e$ is the evaporation rate, W is the width of the substrate, and t_h is the thickness of the substrate.

Most studies utilize the correlation found in the ASHRAE handbook to estimate the evaporation rate (Shah 2014).

$$\dot{m}_e = (P_w - P_v)\frac{0.089 + 0.0782\,V_{air}}{Y}, \tag{14}$$

where P_w is the saturated pressure, P_v is the partial pressure of vapor, V_{air} is the air flow speed, and Y is the heat of vaporization of water. Ignoring convection effects, evaporation from a porous surface behaves like a fully wetted surface, provided that the pore size is small relative to the size of the surface (Beyhaghi et al. 2014).

However, the assumption of constant evaporation flux has been questioned. Veran-Tissoires *et al.* (Veran-Tissoires et al. 2012) determined that evaporation during imbibition would result in a non-uniform evaporation flux distribution, with a much higher flux within the imbibition front surface. Van Engeland *et al.* developed a wicking model which assumes a non-constant evaporative flux (Van Engeland et al. 2020). Their model assumes that evaporation from the surface of the porous medium is driven by diffusion. Starting from Fick's law, the molar evaporative flux (mole/s per m^2), j is given by Eq. 15

$$j = \frac{\phi c_g D_{va}}{\tau}\frac{1}{H-h} ln\left(\frac{1-X_a}{1-X_i}\right) \tag{15}$$

Combined with imbibition governed by Darcy's law, the final equation for imbibition velocity is given by Eq. 16,

$$\frac{dh}{dt} = \frac{K}{\mu_l \phi}\frac{P_c - \rho_l g h}{h} - \frac{c_g D_{va}}{c_l \tau}\frac{1}{H-h} ln\left(\frac{1-X_a}{1-X_i}\right), \tag{16}$$

where ϕ is the porosity, K is the permeability, P_c is the capillary pressure, c_g is the gas molar concentration , c_l is the liquid molar concentration, D_{va} is the diffusion coefficient of vapor in air, τ is the tortuosity, H is the height of the porous medium, h is the height of wicking

front, X_i is the mole fraction of gas at the liquid-air interface, and X_a is the mole fraction of gas at the top of the porous medium.

The presence of humidity can also lead to residual saturation of the paper substrate. This parameter has been incorporated into the Fries *et al.* model by a multiplicative adjustment (Jahanshahi-Anbuhi et al. 2014). A more analytical approach was made by modeling moist soils (Kao and Hunt 1996). By modeling soil as a capillary tube, the capillary diameter was adjusted by an initial saturation to account for the reduction in volume due to the liquid-coated internal surface.

3.2.3.4 Tortuosity

Tortuosity describes how twisted (how many twists/turns) a path is relative to a straight line. It depends on the topology of the material, which includes the porosity and the interconnectivity of the microstructure. However, there is no fixed method to determine tortuosity. In fact, there is debate whether tortuosity is an intrinsic property of the material, or an artificial parameter that attempts to correlate real data with experimental models. Many of the parameters that are used in calculations are derived from experimental data. Moreover, the tortuosity of a material can be influenced by different factors, such as saturation and material properties. The review written by Ghanbarian *et al.* (Ghanbarian et al. 2013) contains a thorough analysis of different tortuosity models that have been used previously.

3.2.3.5 Contact Angle

The contact angle used in the LW equation (Eq. 5) assumes static conditions in a single capillary for simplification purposes. Often, the contact angle is assumed to be

0° due to the high affinity of cellulose for water. As water is absorbed into the paper, the contact angle quickly reduces to 0° (Liukkonen 1997). In this case the effect of wettability is absorbed into the effective pore diameter D_e (Camplisson et al. 2015; Adkins et al. 2016; Kalish et al. 2020) However, others have reported static contact angles such as 26° (Joubert et al. 1959; Liukkonen 1997), 34±4° (Channon et al. 2019) and 75° (Cummins et al. 2017). Others have shown that that the contact angle is associated with the speed of the moving fluid front (Dussan 1979; Degennes 1985) and the internal structure of the substrate. There have been many investigations on the importance of dynamic contact angle (Marmur 1992; Hamraoui and Nylander 2002; Martic et al. 2002). Bracke *et al.* (Bracke et al. 1989) proposed that the dynamic contact angle θ_d and the static contact angle θ_s are related by,

$$\frac{cos\theta_d - cos\theta_s}{cos\theta_s + 1} = -2Ca^{1/2}, \tag{17}$$

where Ca is the capillary number, $Ca = \mu v/\gamma$.

Capillary numbers calculated from our own previous data typically had a magnitude of 10^{-3} (data not shown), which suggests a small difference between dynamic and static contact angle values ($\cos\theta_d \approx \cos\theta_s$ from Eq. 17). Therefore, for modeling purpose, it is acceptable to assume a static angle, which would simplify calculations.

3.2.3.6 Swelling

Swelling has largely been neglected as most imbibition models assume a rigid structure, which makes the final solutions relatively simple. Since effective diameter and effective permeability are represented parameters, the effects of swelling have been incorporated into these values. It has been shown that a single fiber can expand up to 85%

(Mantanis et al. 1995), producing a noteworthy effect on permeability and porosity. Therefore, swelling is a major influence on imbibition dynamics in paper devices.

Incorporating porosity and liquid-uptake as time-dependent variables produces immensely complicated relationships due to the system becoming a deformable porous medium (Spiegelman 1993; Ambrosi 2002; Diersch et al. 2010).

Attempts have been made to produce straightforward models while still incorporating overall swelling effects. Schuchardt and Berg (Schuchardt and Berg 1991) incorporated swelling through a linear function,

$$D = D_0 - \beta t \,, \tag{18}$$

where D is the pore diameter, D_0 is the pore diameter "seen" by the meniscus, and β is a fitting constant representing the rate of constriction. Incorporating Eq. 18 in the capillary model (Eq. 7) results in,

$$h = \sqrt{\frac{D_0 \gamma cos\theta}{4\mu}\left(t - \frac{2\beta}{D_0}t^2 + \frac{4\beta^2}{3D_0^2}t^3\right)} \tag{19}$$

Note that when $\beta = 0$, Eq. 19 reduces to the traditional LW equation (Eq. 7). Eq. 19 has been shown to agree favorably with experimental data. Based on Schuchardt and Berg's swelling relation (Eq. 18), constrictions will become more apparent as time increases.

Masoodi *et al*. (Masoodi and Pillai 2010) proposed a more complex model derived by using Darcy's equation and by incorporating sink terms in the mass conservations,

$$h = \sqrt{\frac{2P_c}{\phi\mu} e^{(b-1)\,\phi/\phi_0} \int_0^t e^{(1-b)\,\phi/\phi_0} K(t')dt'} \,, \tag{20}$$

where ϕ_0 is the porosity in front of the meniscus, b is a fitted absorbent coefficient, and $K(t')$ is a time- dependent permeability utilizing the same linear relationship as Schuchardt and Berg.

Ha *et al.* observed that horizontal imbibition into cellulose sponges is proportional to $t^{1/2}$. In vertical imbibition, the front grows proportional to $t^{1/2}$ but changes in later stages (Ha et al. 2018). For non-aqueous liquids which cause the paper to swell differently, (silicone oils etc.) late-stage imbibition is proportional to $t^{1/4}$ as seen in Eq. 21. The work of Ha and Kim contains a more thorough review of this topic (Ha and Kim 2020).

$$h \sim \left[\frac{\gamma^3}{\mu(\rho g)^2 r}\right]^{1/4} t^{1/4} \,, \tag{21}$$

where μ is viscosity, R is capillary radius, and ρ is liquid density.

3.2.4 Richards Equation

Both Darcy's Law and the LW equation assume that the paper is fully saturated behind the wetting front. That is, the paper is either fully dry or fully saturated. However, previous findings have shown that during wet-out flow, wetted regions of paper remain unsaturated even after the wetting front has passed (Chang et al. 2018). Therefore, a model which accommodates the saturation-level of the paper would be more accurate. The fundamental equation governing flow in unsaturated porous media is the Richards equation (Richards 1931), which assumes that permeability and suction are dependent on volumetric water content θ_w.

These assumptions, along with Darcy's law and mass conservation, lead to,

$$\frac{\partial \theta_w}{\partial t} = \frac{\partial}{\partial x}\left(\widetilde{K}(\theta_w)\frac{\partial \Psi}{\partial x}\right), \tag{22}$$

where $\widetilde{K}(\theta_w)$ is the hydraulic conductivity and Ψ is the pressure head (suction). Eq. 22 can also be rewritten as,

$$\frac{\partial \Theta}{\partial t} = \frac{\partial}{\partial x}\left(D(\Theta)\frac{\partial \Theta}{\partial x}\right), \tag{23}$$

where $D(\Theta) = \widetilde{K}(\theta_w)\frac{\partial \Psi}{\partial \theta_w}$ and is referred to as the water diffusivity. Eq. 22 can also be written in several other ways, with or without a gravity term (Gillespie 1959; Ruoff et al. 1960; Kao and Hunt 1996; Lockington et al. 2007; Jaganathan et al. 2009; Ashari et al. 2010). For clarity, saturation Θ is defined as the ratio between volumetric water content and porosity, $\Theta = \theta_w/\phi$. The system is fully saturated when volumetric water content and porosity are equal. An analytical solution for the Richards equation is seldom attainable due to its high non-linearity. For the equation to be solvable, the permeability and pressure head need to be functions of saturation (Jaganathan et al. 2009). Scientists have tried developing linear methods to solve this equation. Iterative techniques such as the Newton-Raphson and Picard methods have been successfully applied (Celia et al. 1990; Bergamaschi and Putti 1999). Berardi *et al.* used time and space discretization methods to derive a 1D Richards equation describing water infiltration through the interface of two different soil layers (Berardi et al. 2018).

A more comprehensive summary of iterative methods for solving Richards equation was published by List and Radu (List and Radu 2016). Moreover, many groups have designed software to carry out simulations, mainly using temporal or spatial

discretization. Farthing and Ogden have documented a list of solvers that have been developed for solving Richards equation (Farthing and Ogden 2017).

3.3 Flow Simulation and Visualization Tools

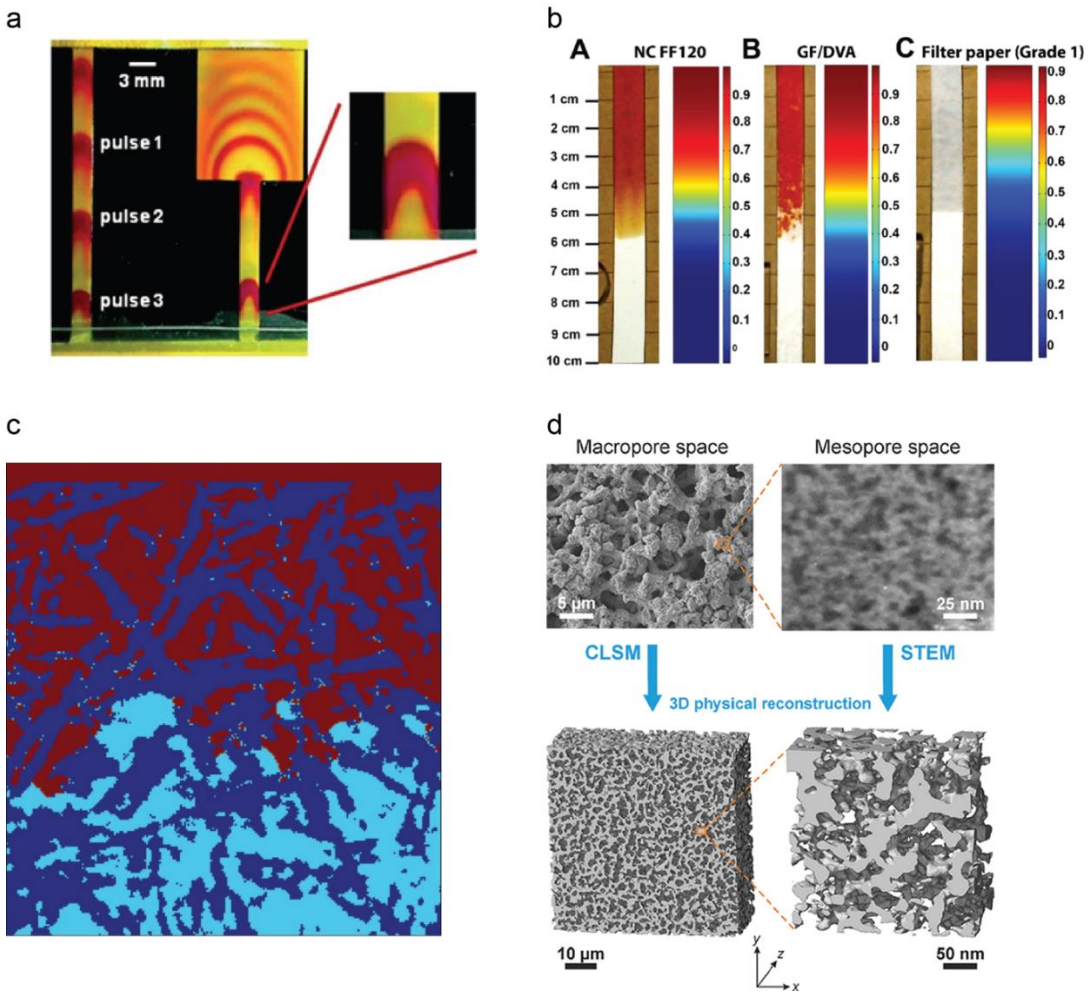

Fig. 3.3 Simulation strategies for porous media flow. (a) Flow visualization using electrochemical pulses. Adapted from (Kauffman et al. 2010) with permission from The Royal Society of Chemistry. (b) COMSOL simulation of fluid distribution in different paper strips. Adapted with permission from (Rath et al. 2018). Copyright (2018) American Chemical Society. (c) Liquid imbibition into a porous medium. The red, blue and cyan regions depict the liquid, solid and gas phases respectively. Reprinted figure with permission from (Hyvaluoma et al. 2006). Copyright (2006) by the American Physical Society. (d) CSLM and STEM reconstruction of silica monoliths. Adapted with permission from (Tallarek et al. 2019). Copyright (2019) American Chemical Society.

Simulating flow computationally is an important tool that is used to validate mathematical models as well as visualize flow behavior under different circumstances. Martic *et al*. (2002; 2004) used molecular dynamic simulations to study the early stages of the velocity-dependent contact angle. Fu *et al.* (Fu et al. 2010) (Fig. 3.3a) and Masoodi *et al.* (Masoodi et al. 2011) used simulations to validate and visualize flow in expanding and contracting channels. Mendez *et al.* (Mendez et al. 2010) similarly validated results in fan-shaped porous channels. WitkowskaNery *et al.* (WitkowskaNery et al. 2016) investigated an array of channel geometries where computational simulations were used to optimize the channel geometry for glucose and uric acid detection. Garcia *et al.* conducted pore-scale simulations regarding the spatial distribution of liquid-liquid interfaces within porous media (García et al. 2016). Tirapu-Azpiroz *et al.* developed a multiphase flow model to track paper imbibition (Tirapu-Azpiroz et al. 2018). Their formula results in two, coupled Darcy's law equations that represent pressure and saturation of the wetting and nonwetting fluids. A finite element solver (COMSOL) was used to simulate their model.

Rath *et al.* used the Richards equation to model imbibition in paper. The group experimentally determined relations for capillary pressure and permeability as functions of saturation. Capillary pressure was derived by centrifuging a fully saturated piece of paper for a set time then measuring its mass. Assuming that liquid in the paper is at equilibrium after every spin cycle, the capillary pressure was equated to the centrifugal force. Relationships between k and θ were determined theoretically. Comparing the pressure drop specified by the Hagen-Poiseuille equation and Darcy's Law yields $k = Cr^2$ (where C is a constant of proportionality). Values of r were determined from Ψ vs. θ curves using the

Young-Laplace equation. These relationships were fitted to the van Genuchten equations, which have been used extensively to model water infiltration into unsaturated soils, and imbibition was simulated using COMSOL (Van Genuchten 1980; Rath et al. 2018). This group is among the first to design flow-control architectures straight from computational models. They successfully designed a 2D paper device that sequentially delivers fluids at specific intervals (Rath and Toley 2020). In a related development, DeChiara *et al.* developed software that automatically designs paper channels based on user inputs (DeChiara et al. 2017). Known as AutoPAD, the software auto-generates channels based on the desired number of inlets and outlets. This software can be used to design multilayer devices with interconnected channels.

As beneficial as simulations are, a glaring drawback is their inability to model the paper structure itself. This can lead to inaccurate fluid flow representations. However, advanced imaging methods have enabled accurate representations of the paper structure and fluid flow. Nuclear magnetic resonance (NMR) cryoporometry has frequently been used in the geology and soil science fields to non-destructively determine pore parameters such as the porosity and pore size distribution of the material (Strange et al. 1993; Gane et al. 2004). For a detailed review, see the work of Mitchell *et al.* (Mitchell et al. 2008). This NMR technique has been applied to paper to determine porosity and pore-size distribution as well characterize the morphology of the paper (Capitani et al. 2002). NMR has also been used to evaluate the moisture content of paper substrates (Froix and Nelson 1975) and to determine the diffusivity coefficient with respect to moisture content (Topgaard and Soderman 2001). de Azevedo *et al.* (de Azevedo et al. 2008) used magnetic resonance

imaging (MRI) to determine the diffusivity of paper fibers. They were able to characterize imbibition in unsized paper and determine the existence of a precursor film that develops ahead of the macroscopic liquid front.

Imbibition simulations with accurate representations of the paper structure can be done using x-ray imaging techniques. In x-ray microtomography, many two-dimensional projections can be combined to reconstruct the paper sample. Hyvaluoma *et al.* (Hyvaluoma et al. 2006) studied radial liquid penetration in a paper board, which is a thicker form of paper (Fig. 3.3c). They determined that unidirectional penetration is described well by the LW equation. They also theorized that the leading front proceeds along fibers, a similar conclusion to that of de Azevedo *et al* .(de Azevedo et al. 2008). Lavrykov *et al.* (Lavrykov et al. 2016) determined the directional permeabilities of the paper substrate. By using x-ray microtomography, the three-dimensional paper reconstruction was skeletonized. Once skeletonized, simulations allowed the resistances and tortuosity to be correlated to the permeabilities. X-ray microtomography has also been used to study the link among the way a specific type of paper is made, its microstructure, and the mechanical properties of the fibers inside (Marulier et al. 2012). Microtomography techniques have also been used to determine effective contact angles for two-phase flow in porous media (Scanziani et al. 2017; Mascini et al. 2020). Using x-ray densitometry, a detailed visualization of imbibition in paper can be obtained (Beuther et al. 2010). From these images, the roughening of the liquid front can be seen with potential precursor films and the liquid gradients assumed in Richards equations. Electron microscopy has also been previously used to reconstruct porous media (Tallarek et al. 2019) (Fig. 3.3d).

3.4 Coarse-Grain Model of Richards Equation

A computer-based simulation was developed using Richards Equation to simulate imbibition into Whatman 4 filter paper. As stated previously, Richards Equation takes the form

$$\frac{\partial \Theta_w}{\partial t} = \nabla \cdot (D(\Theta_w)\nabla\Theta_w)\,, \tag{24}$$

where $D(\Theta) = \frac{k(\theta_w)}{\mu}\frac{\partial \Psi}{\partial \theta_w}$ and is referred to as the water diffusivity (m^2/s) and k and Ψ are permeability and capillary pressure respectively. The challenge is determining relationships between k and Ψ as functions of θ_w, which are not readily available. As reported previously, Rath *et al.* determined relations for permeability and pressure experimentally and fitted them using van Genuchten correlations. They used these correlations to simulate imbibition using COMSOL. However, one specific issue arises with filter paper. The team were unable to achieve a saturation below 0.3, as they were unable to extract any more moisture from the paper using centrifugation. The correlations they use are only valid for $\theta_w \in$ (0.3-0.99). Therefore, we implemented a simplified power-law relation for both Ψ and k (Eq 25-26) which defines values of pressure and permeability through the full the range of saturation values.

$$\Psi = \Psi_0 \theta_w^n \tag{25}$$

$$k = k_0 \theta_w^n \tag{26}$$

We defined Ψ_0 and k_0 as the capillary pressure and permeability in the paper when $\theta_w = 0$. Treating the paper as a bundle of capillary tubes, the pore radius was estimated by fitting distance vs. time curves for blank and grooved channels (20% speed) to the LW equation.

The corresponding pressure was then calculated using the Young-Laplace equation. Permeability was estimated from the pore radius using the capillary-model permeability ($k_0 = \frac{r^2}{10}$) (Masoodi and Pillai 2010). For Whatman 4, the pore radius was 0.219 μm for blank channels and 0.822 μm for grooved channels. The relations obtained using these parameters for blank Whatman 4 filter paper are seen in the graphs below (Fig. 3.4).

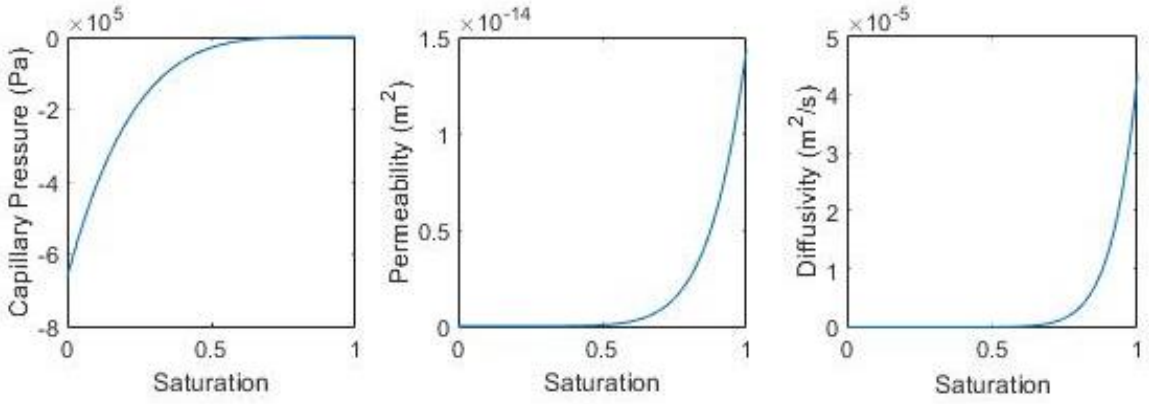

Fig. 3.4 Relations for capillary pressure, permeability and diffusivity as functions of saturation for blank Whatman 1 Filter paper. The capillary pressure is strongest when the paper is unsaturated. As the pores fill with liquid, the capillary pressure reduces to 0 Pa at θ_w = 1. Conversely, permeability and diffusivity increase in value as more pores are filled with fluid.

As shown in Fig. 3.5, Richards Equation was solved within the paper using a 'Finite Volume' approach. A mesh grid was generated over the entire geometry of the paper. The regions encapsulated by the mesh can be thought of as individual control volumes. A single node is placed in the center of each control volume. The distance between adjacent nodes is fixed (dx/dy in the x/y directions). The product of diffusivity and gradient of volumetric water content determines the flux at each node. Therefore, the volumetric water content at each node can be determined by summing the flux entering/exiting each control volume in the the x and y directions at each timestep.

$$\frac{\partial \theta_w}{\partial t} = \nabla \cdot (D(\theta_w) \nabla \theta_w)$$

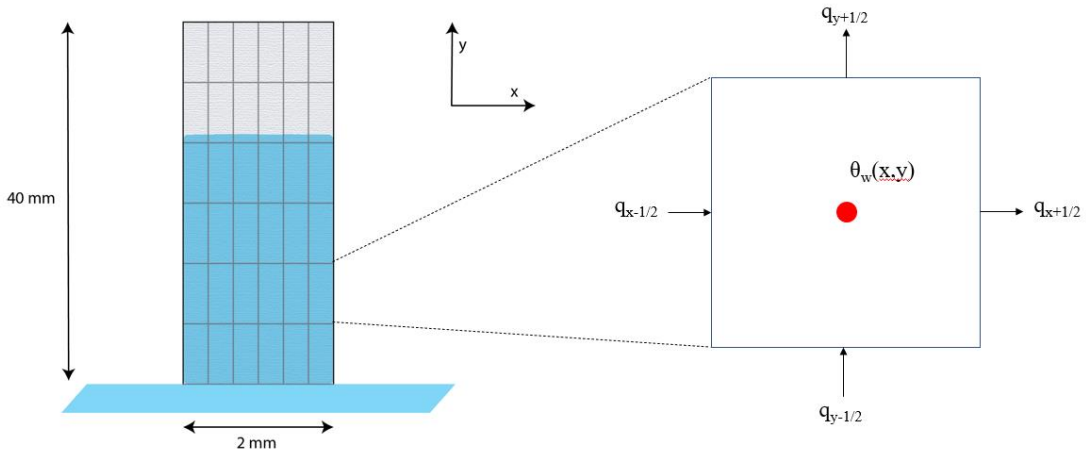

Fig. 3.5 Schematic showing the finite-volume approach that is used to solve Richards equation. A mesh is generated over the entire paper, creating a grid of control volumes. A single node is placed in the center of each control volume. The change in volumetric water content at each node is the sum of the fluxes entering/exiting that control volume.

Following from previous experiments, the paper channel has a width of 2mm and a length of 40mm (Fig. 3.6). Additionally, the simulation assumes that the paper is vertically suspended into a reservoir of fluid. A Dirichlet boundary condition ($\theta_w = 1$) is applied at the bottom edge of the paper, where it touches the fluid reservoir. The interior of the paper is assumed completely dry ($\theta_w = 0$). The remaining three edges have zero-flux, Neumann boundary conditions. For blank paper, this means that there is no net flux in the lateral (x) direction. The timestep for each iteration was defined as $dt = \frac{(dy)^2}{D_0}$ where dy is the gap between adjacent nodes in the y direction and D_0 is the diffusivity at $\theta_w = 1$. Appendix H contains derivations for the time-step that was used in the simulation. At each time step, the wetting front was identified at the point where $\theta_w = 0$ inside the mesh.

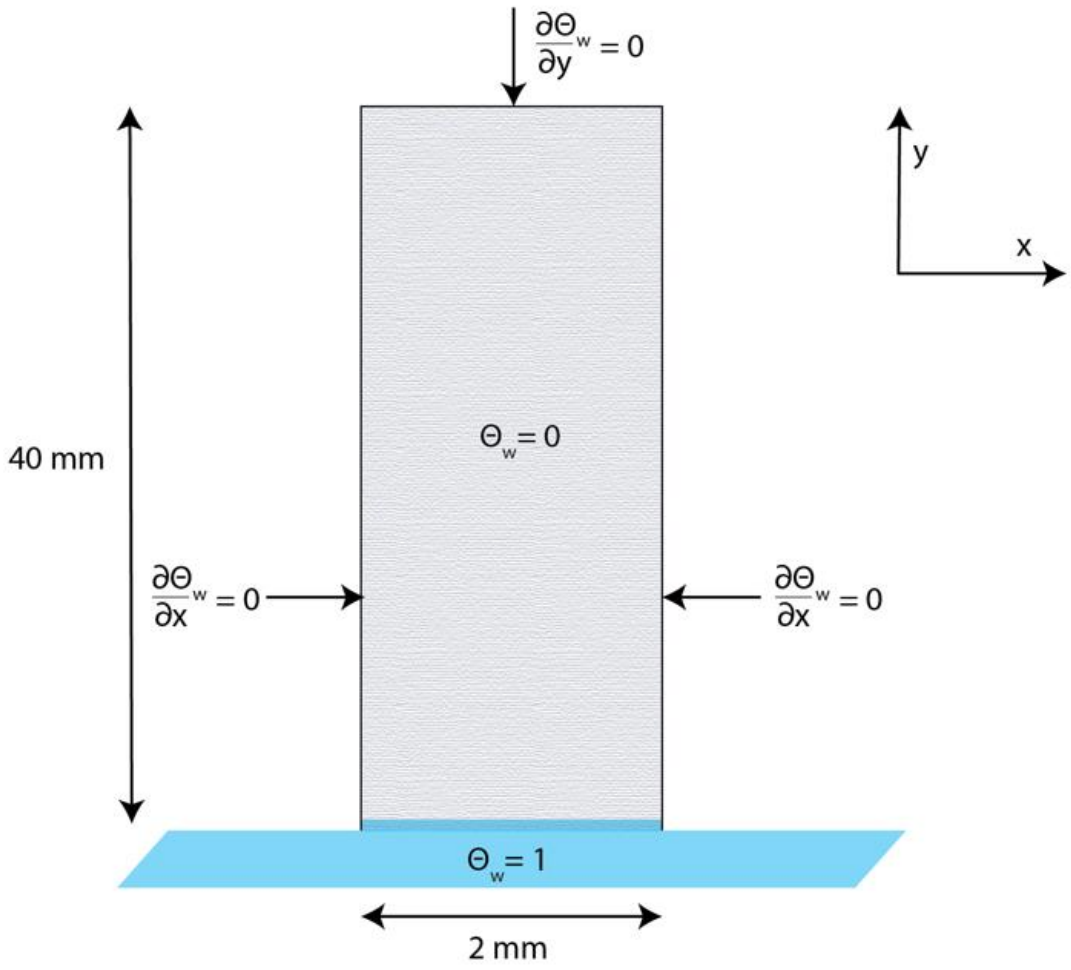

Fig. 3.6 Experimental setup for 1D imbibition into blank and grooved channels (using effective pore radius).

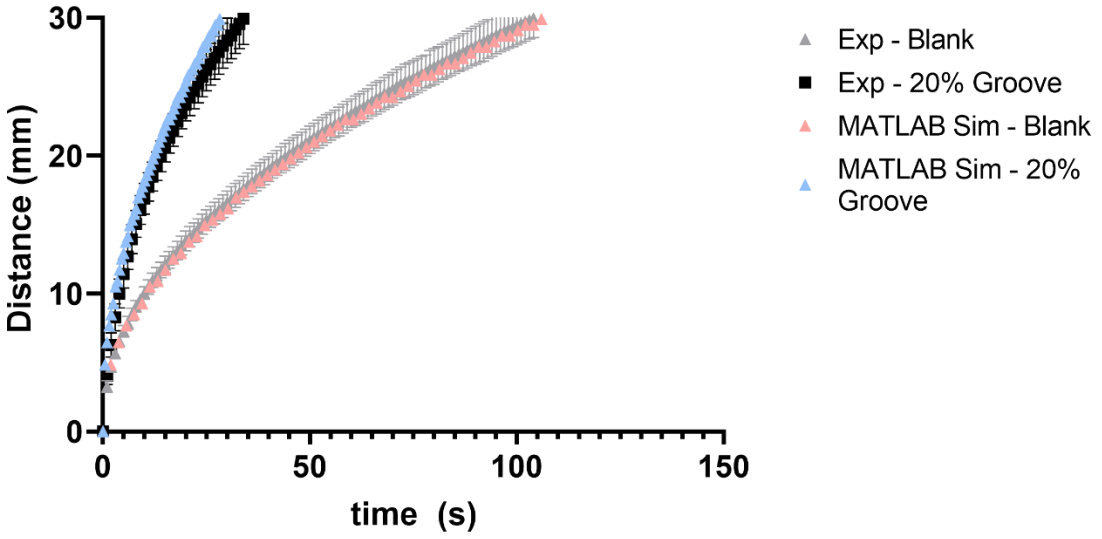

Fig. 3.7 Distance vs. time plots of experimental and simulation data for Whatman 4. that is used to calculate the saturation at each time step. This approach can determine the flux value from either direction and more easily add flux boundary conditions.

Fig. 3.7 shows a strong correlation between experimental data and simulation results for both blank and grooved channels, suggesting that this simplistic modeling approach may be effective in predicting wicking behavior in blank or grooved channels. As reported in Section 2, it is believed that grooved channels wick faster due to the transfer of fluid from the groove into the paper. The modeling approach described above does not consider this phenomenon. The effective radius derived from the LW equation combines the effects of the groove and paper into a single value. To accurately capture the fluid transfer process between groove and paper, the capillary rise of fluid within the groove must be explicitly simulated alongside imbibition in the paper.

3.5 Preliminary Model of Detailed, Multiphase Flow in Grooved Channels

Experimental observations noted that the fluid within the groove did not rise to the top of the channel, instead stopping at ~35 mm (Fig. I1, Fig. J1). We assumed that the force of gravity balanced the capillary pressure at this height. Given the observed final rise height and the radius of the groove, (90 μm) Jurin's law, which takes the form

$$h_r = \frac{2\gamma cos\theta}{\rho g r}, \tag{27}$$

was applied to determine a contact angle (θ) corresponding to the final rise height. The contact angle was then applied to the Young-Laplace equation to determine an equivalent capillary pressure. To model the groove, it was treated as a porous medium, albeit one with a single, large pore. This assumption allowed us to apply Richards equation to the groove as well. As with the paper, power-law relations were formulated for P, k and D as functions of saturation. In reality, the saturation within the groove is binary (either 0 or 1). However, applying a continuous function allows gradients to be calculated more easily. As with blank paper, a finite volume approach was used to simulate the paper-groove system. The paper and groove used the same type of mesh, such at the dx/dy values were the same for both.

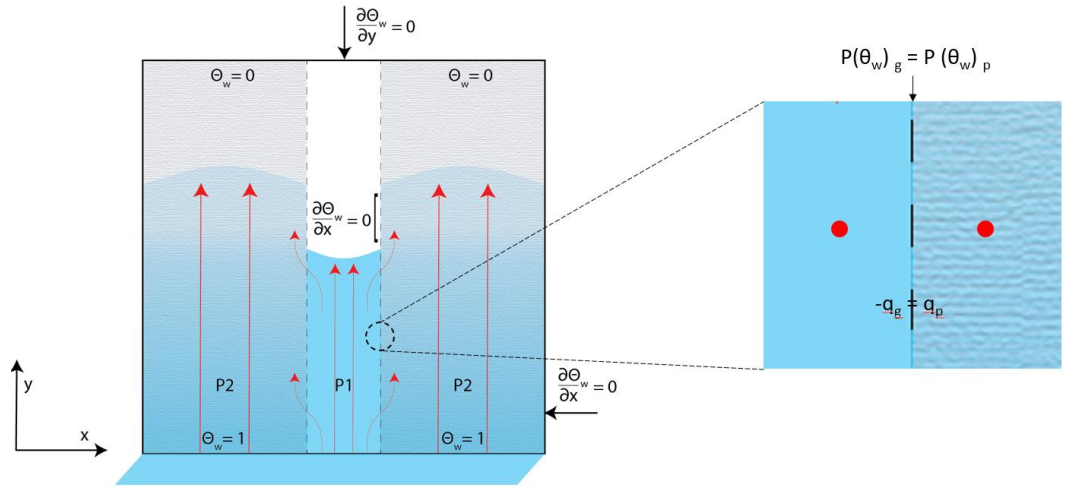

Fig. 3.8 Experimental setup for 2D imbibition into grooved channels using Richards equation for both the groove and paper.

Fig. 3.8 shows a schematic representation of the grooved-channel system being studied. The red lines indicate the flow of liquid from the reservoir underneath the channel. Note, how fluid is transferred from the central groove into the surrounding paper. The two different pressures, in the paper and groove respectively drive this fluid transfer. As before, 100% saturation ($\theta_w = 1$) of the paper at the base of the channel which is immersed in the reservoir. As before, the outer edges of the entire system used a no-flux, Neumann boundary condition. The interface between the groove and paper employed a hybrid flux/pressure condition based on the location of the wetting fronts in the groove and paper. Ideally, the groove-paper system would be solved 'simultaneously' by advancing the groove and paper together and applying appropriate conditions at the interface. Since this is not possible, an iterative approach was used instead. At the start of each iteration, the pressure defined on the interface between groove and paper was equated (P_{paper}(interface) = P_{groove}(interface)). The paper was advanced without considering the presence of the

groove. Next, the groove was advanced using flux/pressure conditions from the paper.

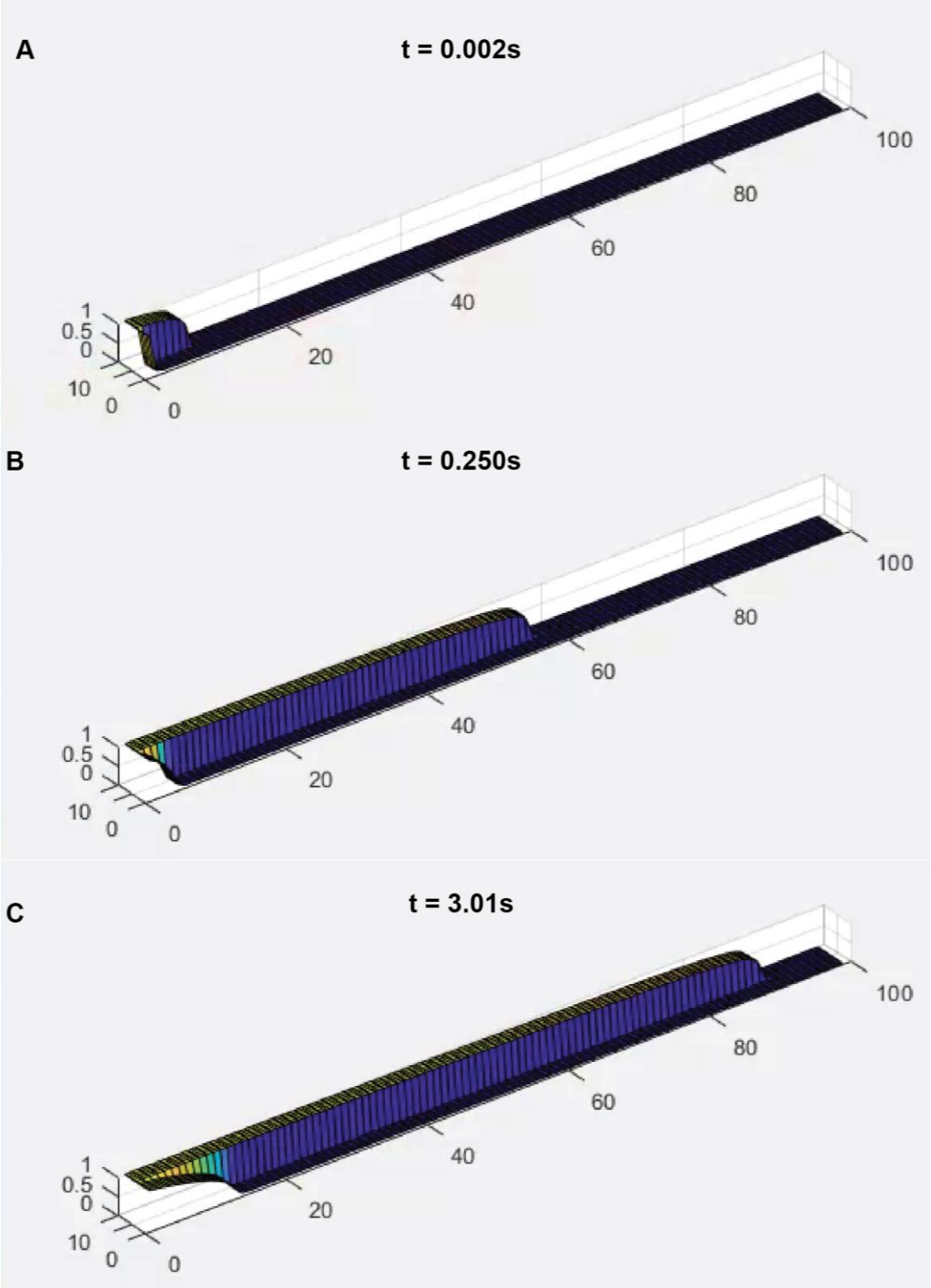

Fig. 3.9 Time-sequence of results for 2D imbibition into grooved channels using Richards equation for both the groove and paper. Paper and groove are simulated side-by-side without any interface conditions.

Simulations run using the specified boundary conditions did not produce results that matched experimental data. Fig. 3.9 shows a time-sequence of simulation results for a paper/groove system without any interface conditions being applied. The groove reaches its equilibrium height in ~3 seconds, far faster than the paper (~190s). The difference in timescales for paper and groove means that the groove is much faster than the paper, even with boundary conditions applied between the two. Additionally, the pressure/permeability for each system are several orders of magnitude apart. Therefore, it appears that a simple, capillary model will overpredict the speed of the groove itself. The groove does not behave like a capillary with an equivalent radius. Further refinement will have to be made to the groove model to achieve more accurate results.

3.6 Conclusion

Modeling of flow in paper is a topic that has been largely overlooked by the biosensors community, mainly because the century-old LW equation has adequately described the macroscopic flow behavior in simple devices, where effective diameter *D* is conveniently adjustable to closely fit many experimental data. More advanced models including ones discussed in this review aim to directly incorporate effects of one or more factors (e.g., evaporation, swelling, and saturation), thus improving their accuracy. However, in these models, solutions are often implicit and/or nonlinear, requiring a numerical solver, or require fitting parameters that are not readily available for biosensor researchers. In this section, we demonstrate successful modeling of wicking in both blank and grooved channels using Richards equation. Our findings highlight the feasibility of simulating more complex transport phenomena that may occur within modified paper channels.

This work highlights two important issues. First, for the field of paper-based biosensors to sustain its rapid advances, the biosensors community needs close collaboration with the porous media and/or fluid dynamics communities. Second, a flow model which is more accurate than the LW model yet almost equally user-friendly without the need of arbitrary fit parameters is currently lacking and highly desirable. The models described here are certainly not exhaustive. The works of Liu *et al.* and Masoodi and Pillai provide discussion on additional modeling techniques used for paper and other porous media (Masoodi and Pillai 2012; Liu et al. 2018).

3.7 References

Adkins, J.A., Noviana, E., Henry, C.S., 2016. Analytical chemistry 88, 10639-10647.

Ambrosi, D., 2002. Z Angew Math Mech 82, 115-124.

Ashari, A., Bucher, T.M., Tafreshi, H.V., Tahir, M.A., Rahman, M.S.A., 2010. Int J Heat Mass Tran 53, 1750-1758.

Benner, E.M., Petsev, D.N., 2013. Phys Rev E 87.

Berardi, M., Difonzo, F., Vurro, M., Lopez, L., 2018. Adv Water Resour 115, 264-272.

Bergamaschi, L., Putti, M., 1999. International journal for numerical methods in engineering 45, 1025-1046.

Beuther, P.D., Veith, M.W., Zwick, K.J., 2010. J Eng Fiber Fabr 5, 1-7.

Beyhaghi, S., Geoffroy, S., Prat, M., Pillai, K.M., 2014. Aiche J 60, 1930-1940.

Bohm, A., Carstens, F., Trieb, C., Schabel, S., Biesalski, M., 2014. Microfluidics and Nanofluidics 16, 789-799.

Bosanquet, C.H., 1923. Philos Mag 45, 525-531.

Bracke, M., Devoeght, F., Joos, P., 1989. Prog Coll Pol Sci S 79, 142-149.

Camplisson, C.K., Schilling, K.M., Pedrotti, W.L., Stone, H.A., Martinez, A.W., 2015. Lab on a Chip 15, 4461-4466.

Capitani, D., Proietti, N., Ziarelli, F., Segre, A.L., 2002. Macromolecules 35, 5536-5543.

Castro, C., Rosillo, C., Tsutsui, H., 2017. Microfluidics and Nanofluidics 21, 21.

Celia, M.A., Bouloutas, E.T., Zarba, R.L., 1990. Water Resour Res 26, 1483-1496.

Chang, S., Seo, J., Hong, S., Lee, D.-G., Kim, W., 2018. J Fluid Mech 845, 36.

Channon, R.B., Nguyen, M.P., Henry, C.S., Dandy, D.S., 2019. Analytical chemistry 91, 8966-8972.

Cummins, B.M., Chinthapatla, R., Ligler, F.S., Walker, G.M., 2017. Analytical chemistry 89, 4377-4381.

Darcy, H., 1856. Victor Dalmont.

de Azevedo, E.N., Alme, L.R., Engelsberg, M., Fossum, J.O., Dommersnes, P., 2008. Phys Rev E 78.

DeChiara, N.S., Wilson, D.J., Mace, C.R., 2017. Scientific reports 7, 1-8.

Degennes, P.G., 1985. Rev Mod Phys 57, 827-863.

Diersch, H.J.G., Clausnitzer, V., Myrnyy, V., Rosati, R., Schmidt, M., Beruda, H., Ehrnsperger, B.J., Virgilio, R., 2010. Transport Porous Med 83, 437-464.

Dussan, E.B., 1979. Annu Rev Fluid Mech 11, 371-400.

Elizalde, E., Urteaga, R., Berli, C.L.A., 2015. Lab on a Chip 15, 2173-2180.

Farthing, M.W., Ogden, F.L., 2017. Soil Science Society of America Journal 81, 1257-1269.

Fries, N., Dreyer, M., 2008. J Colloid Interf Sci 320, 259-263.

Fries, N., Odic, K., Conrath, M., Dreyer, M., 2008. J Colloid Interf Sci 321, 118-129.

Froix, M.F., Nelson, R., 1975. Macromolecules 8, 726-730.

Fu, E., Kauffman, P., Lutz, B., Yager, P., 2010. Sensor Actuat B-Chem 149, 325-328.

Fu, E.L., Ramsey, S., Kauffman, P., Lutz, B., Yager, P., 2011. Microfluidics and Nanofluidics 10, 29-35.

Gane, P.A.C., Ridgway, C.J., Lehtinen, E., Valiullin, R., Furo, I., Schoelkopf, J., Paulapuro, H., Daicic, J., 2004. Ind Eng Chem Res 43, 7920-7927.

García, E.J., Boulet, P., Denoyel, R., Anquetil, J., Borda, G., Kuchta, B., 2016. Colloids and Surfaces A: Physicochemical and Engineering Aspects 496, 28-38.

Gebart, B.R., 1992. J Compos Mater 26, 1100-1133.

Ghanbarian, B., Hunt, A.G., Ewing, R.P., Sahimi, M., 2013. Soil science society of America journal 77, 1461-1477.

Ghassemzadeh, J., Hashemi, M., Sartor, L., Sahimi, M., 2001. Aiche J 47, 519-535.

Gillespie, T., 1959. Journal of Colloid Science 14, 123-130.

Ha, J., Kim, H.-Y., 2020. Annu Rev Fluid Mech 52.

Ha, J., Kim, J., Jung, Y., Yun, G., Kim, D.-N., Kim, H.-Y., 2018. Science advances 4, eaao7051.

Hamraoui, A., Nylander, T., 2002. J Colloid Interf Sci 250, 415-421.

Hyvaluoma, J., Raiskinmaki, P., Jasberg, A., Koponen, A., Kataja, M., Timonen, J., 2006. Phys Rev E 73.

Jafry, A.T., Lim, H., Kang, S.I., Suk, J.W., Lee, J., 2016. Colloid Surface A 492, 190-198.

Jaganathan, S., Tafreshi, H.V., Pourdeyhimi, B., 2009. J Appl Phys 105.

Jahanshahi-Anbuhi, S., Henry, A., Leung, V., Sicard, C., Pennings, K., Pelton, R., Brennan, J.D., Filipe, C.D.M., 2014. Lab on a Chip 14, 229-236.

Joubert, J.M., Krige, G.J.R., Borgin, K., 1959. Nature 184, 1561-1562.

Kalish, B., Tan, M.K., Tsutsui, H., 2020. Microfluidics and nanofluidics.

Kao, C.S., Hunt, J.R., 1996. Water Resour Res 32, 55-64.

Kauffman, P., Fu, E., Lutz, B., Yager, P., 2010. Lab on a Chip 10, 2614-2617.

Lavrykov, S., Singh, S.K., Ramarao, B.V., Ramaswamy, S., Pande, H., 2016. Dry Technol 34, 871-882.

List, F., Radu, F.A., 2016. Computational Geosciences 20, 341-353.

Liu, Z., He, X., Han, J., Zhang, X., Li, F., Li, A., Qu, Z., Xu, F., 2018. Microfluidics and Nanofluidics 22, 132.

Liukkonen, A., 1997. Scanning 19, 411-415.

Lockington, D.A., Parlange, J.Y., Lenkopane, M., 2007. Transport Porous Med 68, 29-36.

Lucas, R., 1918. Kolloid Z 23, 15-22.

Lutz, B., Liang, T., Fu, E., Ramachandran, S., Kauffman, P., Yager, P., 2013. Lab on a Chip 13, 2840-2847.

Mantanis, G.I., Young, R.A., Rowell, R.M., 1995. Cellulose 2, 1-22.

Marmur, A., 1992. Adv Colloid Interfac 39, 13-33.

Martic, G., Gentner, F., Seveno, D., Coulon, D., De Coninck, J., Blake, T.D., 2002. Langmuir 18, 7971-7976.

Martic, G., Gentner, F., Seveno, D., De Coninck, J., Blake, T.D., 2004. J Colloid Interf Sci 270, 171-179.

Marulier, C., Dumont, P.J.J., Orgeas, L., Caillerie, D., du Roscoat, S.R., 2012. Nord Pulp Pap Res J 27, 245-255.

Mascini, A., Cnudde, V., Bultreys, T., 2020. J Colloid Interf Sci 572, 354-363.

Masoodi, R., Pillai, K.M., 2010. Aiche J 56, 2257-2267.

Masoodi, R., Pillai, K.M., 2012. CRC Press.

Masoodi, R., Pillai, K.M., Varanasi, P.P., 2007. Aiche J 53, 2769-2782.

Masoodi, R., Tan, H., Pillai, K.M., 2011. Aiche J 57, 1132-1143.

Mendez, S., Fenton, E.M., Gallegos, G.R., Petsev, D.N., Sibbett, S.S., Stone, H.A., Zhang, Y., Lopez, G.P., 2010. Langmuir 26, 1380-1385.

Mitchell, J., Webber, J.B.W., Strange, J.H., 2008. Phys Rep 461, 1-36.

Nabovati, A., Llewellin, E.W., Sousa, A.C.M., 2009. Compos Part a-Appl S 40, 860-869.

Qin, Y., Zhang, M., Mei, G., 2018. Journal of Hydrology 562, 725-732.

Rath, D., Sathishkumar, N., Toley, B.J., 2018. Langmuir 34, 8758-8766.

Rath, D., Toley, B., 2020. ACS sensors 6, 91-99.

Richards, L.A., 1931. Physics-J Gen Appl P 1, 318-333.

Rideal, E.K., 1922. Philos Mag 44, 1152-1159.

Ruoff, A.L., Stewart, G.H., Shin, H.K., Giddings, J.C., 1960. Kolloid Z 173, 14.

Scanziani, A., Singh, K., Blunt, M.J., Guadagnini, A., 2017. J Colloid Interf Sci 496, 51-59.

Schuchardt, D.R., Berg, J.C., 1991. Wood Fiber Sci 23, 342-357.

Shah, M.M., 2014. ASHRAE Transactions 120, 3-17.

Shou, D.H., Ye, L., Fan, J.T., Fu, K.K., 2014. Langmuir 30, 149-155.

Spiegelman, M., 1993. J Fluid Mech 247, 17-38.

Strange, J.H., Rahman, M., Smith, E.G., 1993. Phys Rev Lett 71, 3589-3591.

Szekely, J., Neumann, A.W., Chuang, Y.K., 1971. J Colloid Interf Sci 35, 273-+.

Tallarek, U., Hlushkou, D., Rybka, J., Höltzel, A., 2019. The Journal of Physical Chemistry C 123, 15099-15112.

Tirapu-Azpiroz, J., Silva, A.F., Ferreira, M.E., Candela, W.F.L., Bryant, P.W., Ohta, R.L., Engel, M., Steiner, M.B., 2018. Journal of Micro/Nanolithography, MEMS, and MOEMS 17, 025003.

Topgaard, D., Soderman, O., 2001. Langmuir 17, 2694-2702.

Van der Westhuizen, J., Du Plessis, J.P., 1996. Compos Part a-Appl S 27, 263-269.

Van Engeland, C., Haut, B., Spreutels, L., Sobac, B., 2020. J Colloid Interf Sci 576, 280-290.

Van Genuchten, M.T., 1980. Soil science society of America journal 44, 892-898.

Veran-Tissoires, S., Marcoux, M., Prat, M., 2012. Epl-Europhys Lett 98.

Washburn, E.W., 1921. Phys Rev 17, 273-283.

WitkowskaNery, E., Santhiago, M., Kubota, L.T., 2016. Electroanalysis 28, 2245-2252.

Wyllie, M.R.J., Gregory, A.R., 1955. Ind Eng Chem 47, 1379-1388.

Xu, P., Qiu, S., Yu, B., Jiang, Z., 2013. Int J Heat Mass Tran 64, 829-837.

Xu, P., Yu, B.M., 2008. Adv Water Resour 31, 74-81.

Zhmud, B.V., Tiberg, F., Hallstensson, K., 2000. J Colloid Interf Sci 228, 263-269.

4. CONCLUSIONS

Paper-based microfluidic devices are an extremely promising for the design of affordable, rapid diagnostic tools. They have the potential to rapidly expand healthcare infrastructure, especially in resource-limited settings. Since the seminal work of Martinez *et al.* nearly 15 years ago, the field has evolved from basic, colorimetric assays into multistep analytical devices that are capable (in some cases) of replacing conventional benchtop assays. Paper has many advantages as an ASSURED diagnostic, including low cost, easy fabrication and ability to wick fluids through capillary action. To increase the penetration of paper-based devices into the greater scientific community, these devices must be able conduct more complex assays; specifically, those requiring multiple fluids and timed incubation steps (i.e., ELISA).

Performing more complicated assays requires precision control of multiple fluids on the paper chip; ideally this needs to be achieved without frequent user intervention. The key is to deliver fluids sequentially at specified intervals. Historically, flow control was achieved by slowing fluid down. This was achieved mainly using geometry changes or adding dissolvable barriers to the paper. Modern flow-control strategies have developed rapidly, incorporating user-actuated components, chemical modification of the paper, or active control of fluid using electricity/magnetism. A recent development is engineering ways to accelerate flow on paper, instead of slowing it down. In general, faster wicking is achieved by letting fluids wick outside the paper. Our investigation showed that etching grooves onto paper using a CO_2 laser is a facile way to rapidly improvement wicking speeds in paper.

Equally important is a better understanding of fluid behavior within the paper. Knowing more precisely how changes to the paper will influence wicking behavior will facilitate direct translation of *in-silico* models to functioning devices. The widely-used Lucas-Washburn equation is easy to use but makes several key assumptions about wicking in paper that are inaccurate. Models like Richards equation take into account the saturation of the medium when calculating pressure and permeability. Our findings show that Richards equation can be used to accurately simulate fluid imbibition in untreated paper and paper etched with grooves. These studies will provide the basis for future studies where more complex analytical devices are designed using novel control strategies and as well as aid in developing more accurate simulations for more complex channel networks.

5. SUGGESTED FUTURE WORK

Applying laser-etched grooves to more complex μPAD designs

We demonstrated the utility of laser-etched grooves in conjunction with a paper-based chemiresistive sensor, which required the delivery of two different fluids. Further development should be done to incorporate laser-etched grooves for more complicated assays, which may require more than two fluids.

Simulate dynamics of sealing with different types of adhesives

Our previous findings showed that wicking speed is highly dependent on how the paper channels are sealed. The construction of the tape plays a significant role. The issue is with low-strength tapes, which tend to lift off the paper once it is wetted by the incoming fluid. This creates hollow pockets between the tape and paper, which can act as capillaries for the incoming flow. This means that flow occurs between the tape and paper instead of inside the paper, which makes the channel significantly faster than expected. Incorporating this phenomenon into simulation would provide more accurate data on the behavior of sealed channels, especially for common sealing methods.

6. APPENDICES

Appendix A. Setup for wicking experiments

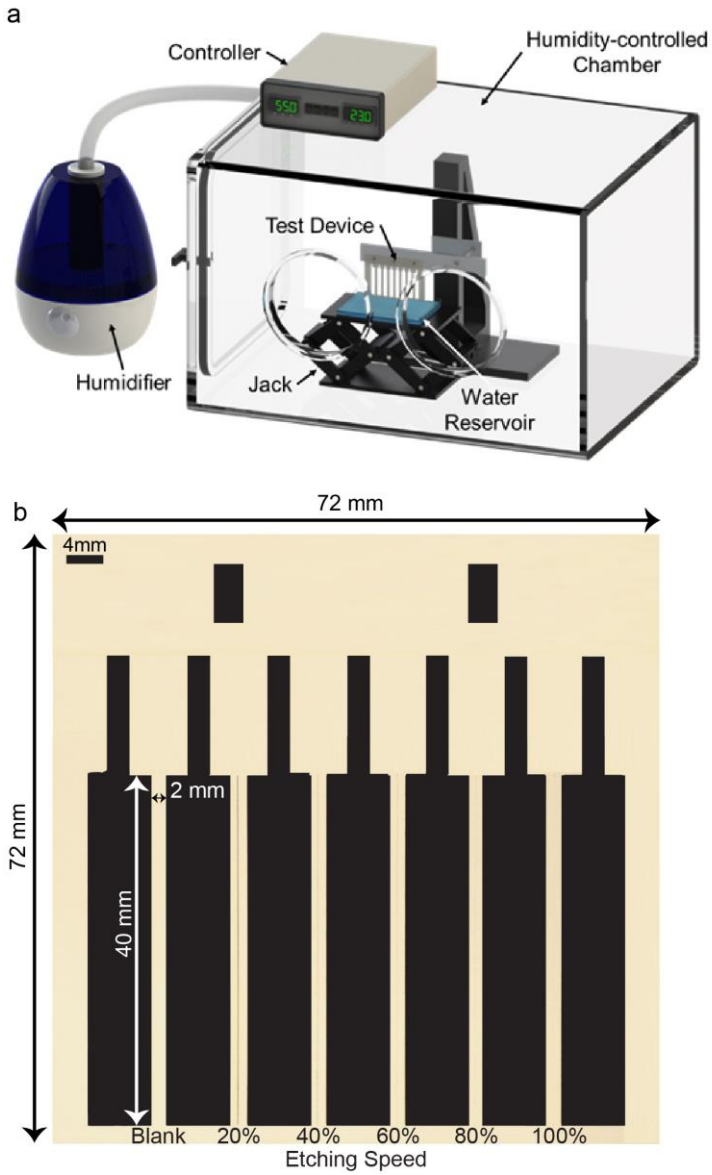

Fig. A1 Summary of experimental setup. (a) Image of the humidity-controlled chamber that was used for vertical wicking experiments. Samples were mounting on the rig seen inside the chamber. A fluid reservoir was placed underneath the rig on a jack, which was raised to immerse the paper into the reservoir. The glove ports were sealed with rubber gloves (not shown) during experiments. (b). Example of a single paper strip. Each strip had six channels; one blank and one with a single groove etched at a different speed. The scale bar in the bottom left was 4mm.

Appendix B. Whatman 4. – Groove cross-section/Mass-loss analysis

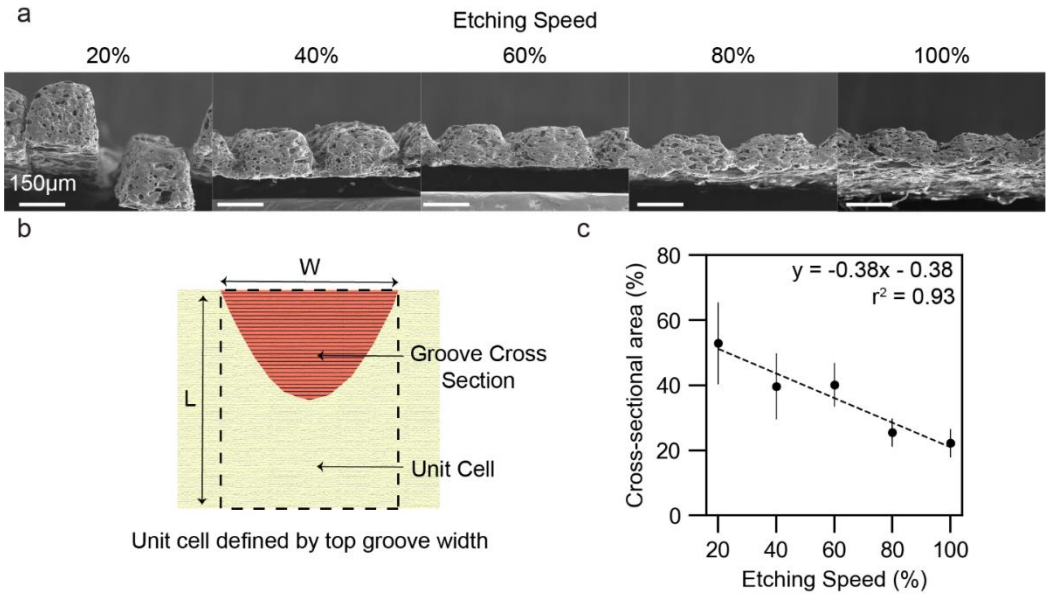

Fig. B1 Whatman 4 groove cross-section analysis. (a) SEM cross-sectional images of grooves etched at different laser speeds. As laser speeds increased, the grooves became shallower. (b) Attempts to characterize groove depth were made by measuring the area of the groove cross-section relative to the area of a unit cell with width (W) equal to the width of the groove and length (L) equal to the thickness of the paper. (c) The through-cut grooves occupied ~60% of the cross-section of the paper. Data presented as mean ± SD. N=3.

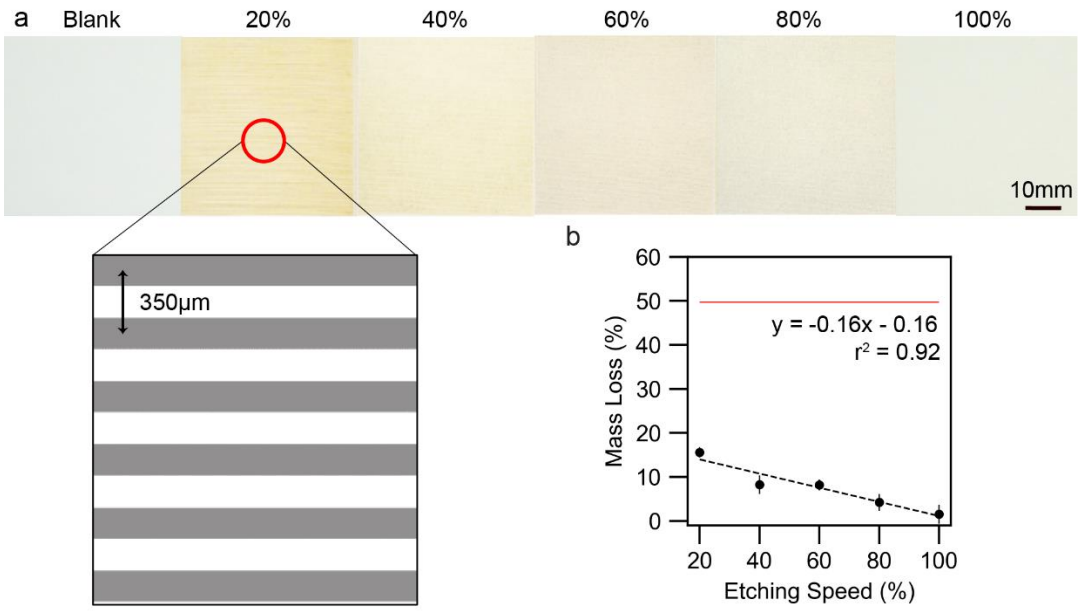

Fig. B2 Groove mass-loss analysis. (a) Image of paper samples that were used in mass loss experiments. Each sample consisted of a 50mm x 50mm strip of paper that was etched with grooves at different speeds. Grooves were spaced 350 µm apart (center-to-center), giving 138 grooves per strip. The scale bar in the upper right is 10mm. (b) Total mass loss for each etching speed follows a linear relationship, varying between 15% and 3%. The red horizontal line denoted the theoretical mass loss for rectangular through-cut grooves with width of 175µm and depth of 180µm. Data presented as mean ± SD. N=10.

Appendix C. Whatman 4. – Dist. vs. Time - Channels sealed with 3M Tape

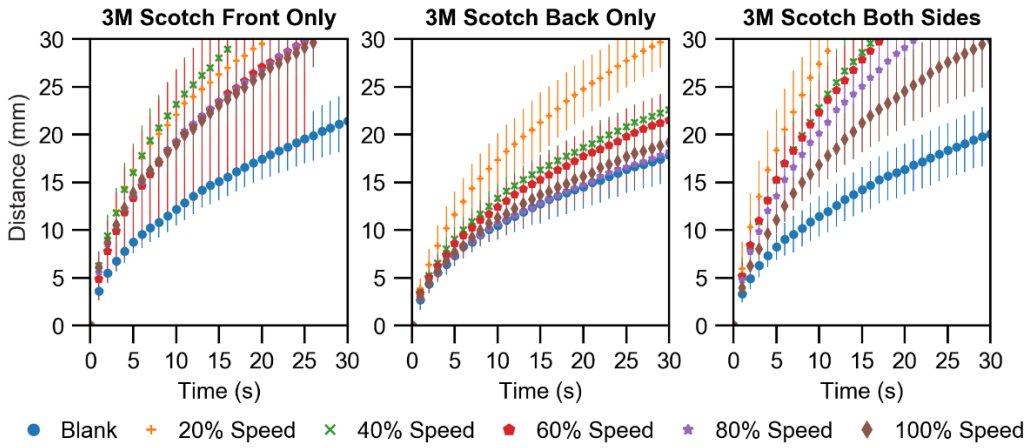

Fig. C1 Distance vs. time plots for grooves etched at different speeds and sealed with 3M Scotch Packing Tape. This tape provided the fastest wicking channels. However, the tendency of the tape to lift off when wetting resulted in a high degree of variability. Data presented as mean ± SD. N=10.

Appendix D. Static contact angle measurements for different tapes

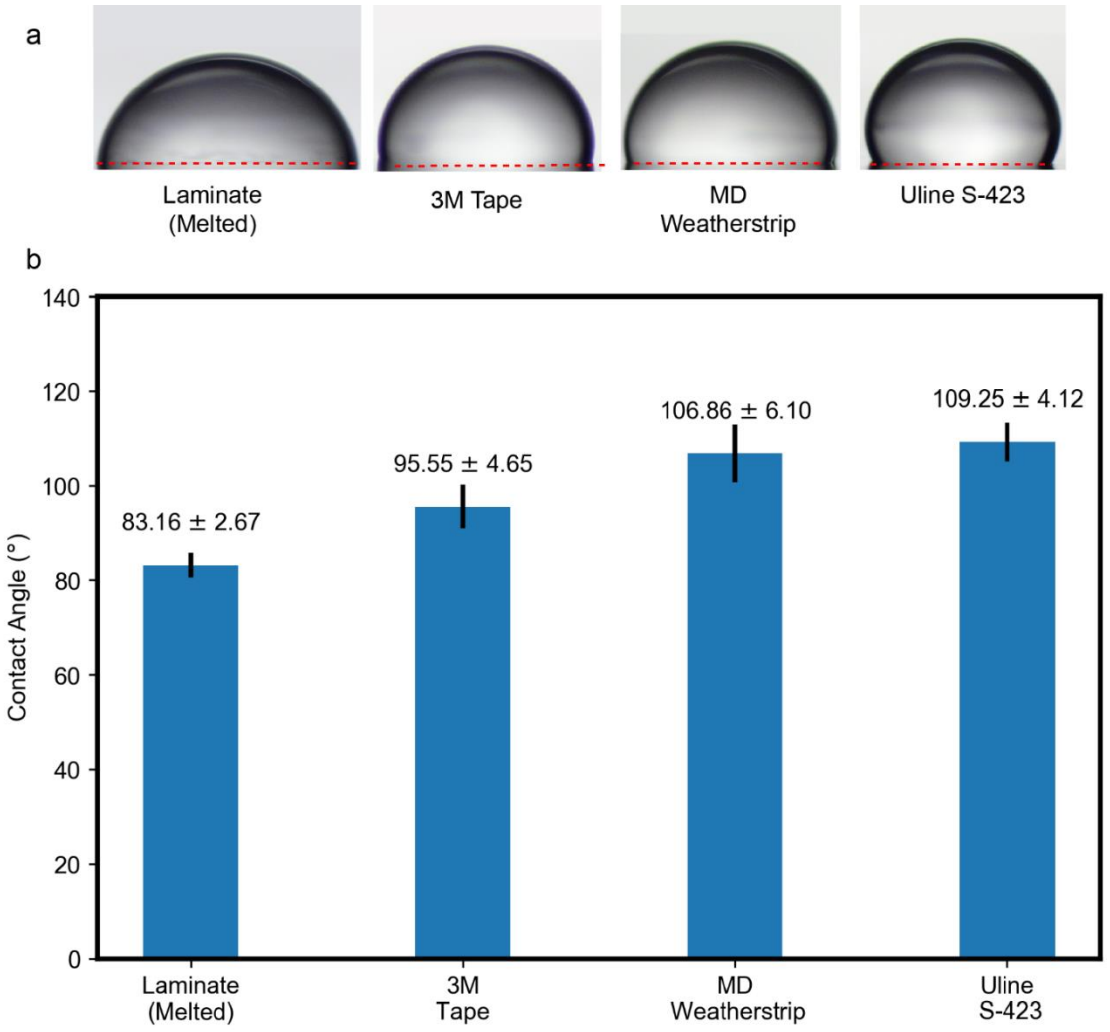

Fig. D1 Contact angle analysis for the different tapes used. (a) Images of droplets used in contact angle measurements. (b) Contact angle measurements for each type of adhesive used. Laminate measurements were made after the laminated was heated at 150°C for 3 minutes. Despite the tapes being hydrophobic, sealed channels generally wicked much faster than unsealed channels. Data presented as mean ± SD. N=5.

Appendix E. Theoretical capillary rise in grooves of various geometries

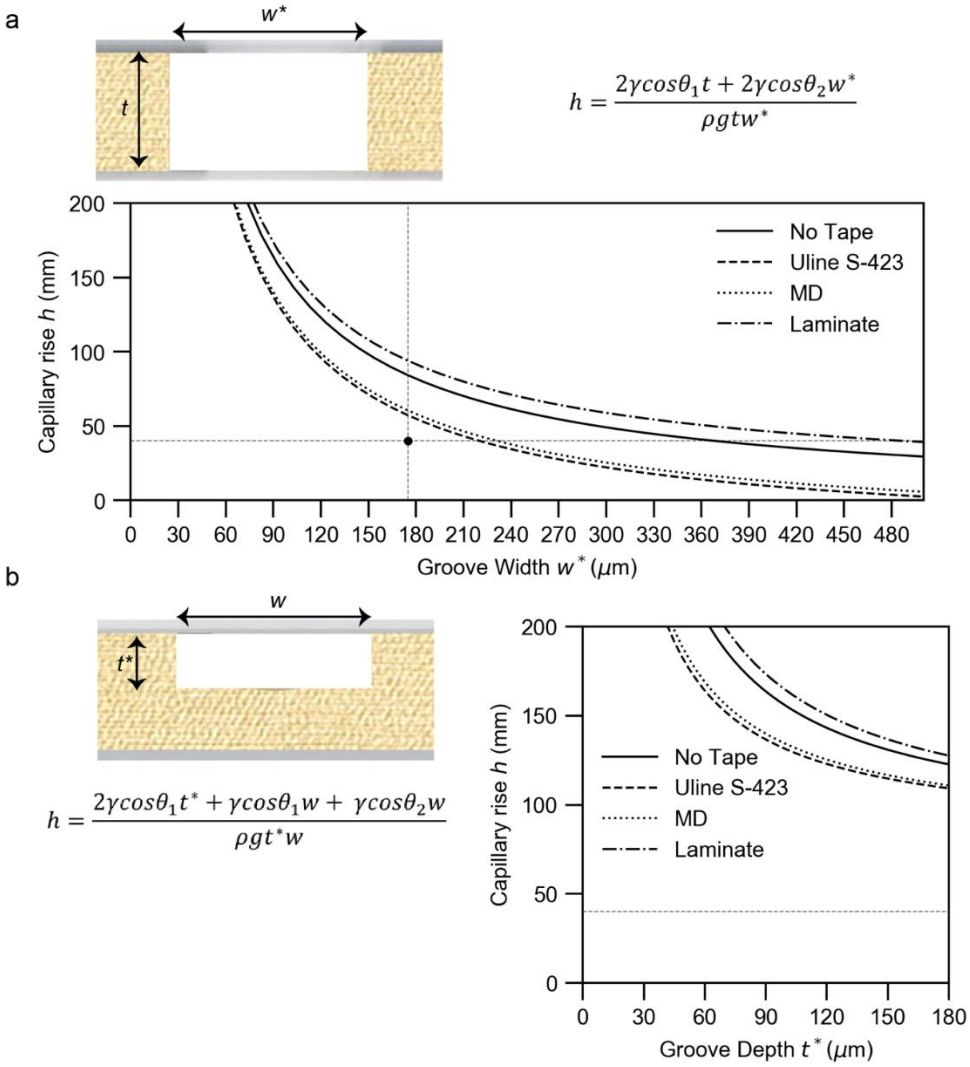

Fig. E1 Analysis of theoretical capillary rise in model rectangular grooves. (a) Theoretical capillary rise for through-cut grooves (corresponding to 20% speed) at different widths, assuming impermeable walls. Contact angles were assumed to be at paper surfaces θ_1 = 0°, and at tape surfaces θ_2 = 109.25°, 106.86°, and 83.16°, for Uline S-423, MD Weatherstrip, and Laminate, respectively. γ was surface tension of water (0.072 N/m), and g was gravitational acceleration (9.81 m/s^2) The dot in the graph was the actual top groove width (175μm) and the full channel length (40mm) used in our experiments. Even with a hydrophobic tape sealing the channels, the fluid in the capillary should theoretically be able to reach the top of the channel. (b) Theoretical capillary rise for partially cut grooves (corresponding to > 20 % speed) at different groove depths. The narrower capillaries created by these grooves should theoretically rise higher/faster than through-cut grooves. However, experimental data contradicted this, possibly due to factors such as permeable walls and loss of fluid mass to surrounding paper matrix.

Appendix F. Whatman 4. – Dist. vs. Time for high viscosity fluids

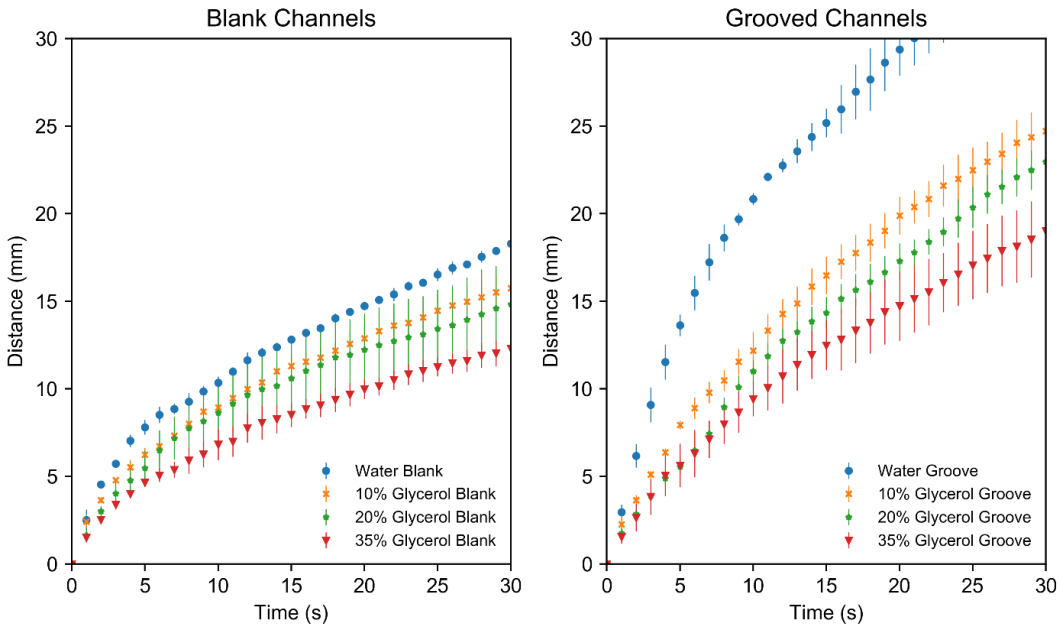

Fig. F1 Distance vs. time plots for blank and 20% etched groove channels (Whatman 4 Filter Paper) imbibing DI H_2O, 10%, 20% and 35% v/v glycerol solutions. All channels were sealed on both sides with Uline S-423 Packing Tape. Increasing the viscosity of the fluid had a dramatic effect on the performance of the channels. This highlights the importance of taking fluid viscosity into consideration when designing paper-based devices. Data presented as mean ± SD. N=3.

Appendix G. Chemiresistive Sensor timelapse + detection data

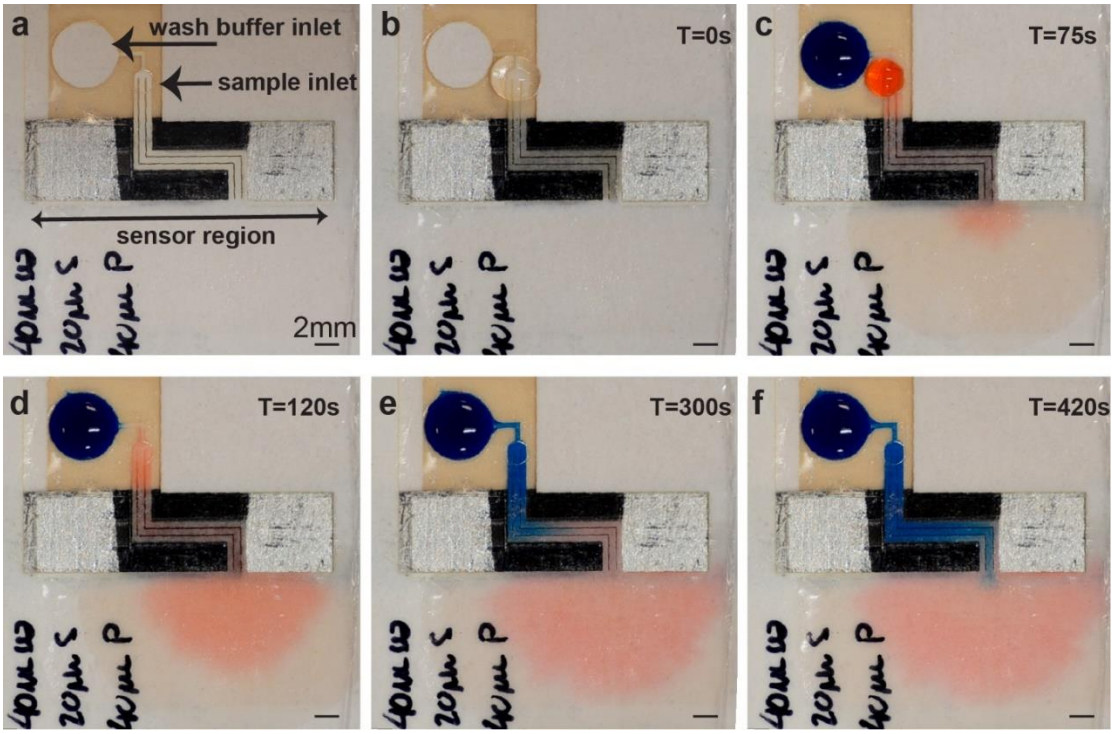

Fig. G1 Time-lapse of sequential fluid delivery in paper-based chemiresistive sensor device (a). After a priming buffer was added to the channel (b), a sample and wash buffer were simultaneously deposited (red and blue dye respectively) (c). The grooves in the channel drove the sample towards the sensor rather than towards the wash buffer (d). The presence of the sample droplet prevented the dye from wicking until the sample was completely gone (e). After that, the wash buffer flowed across the sensor (f). Scale bar = 2mm.

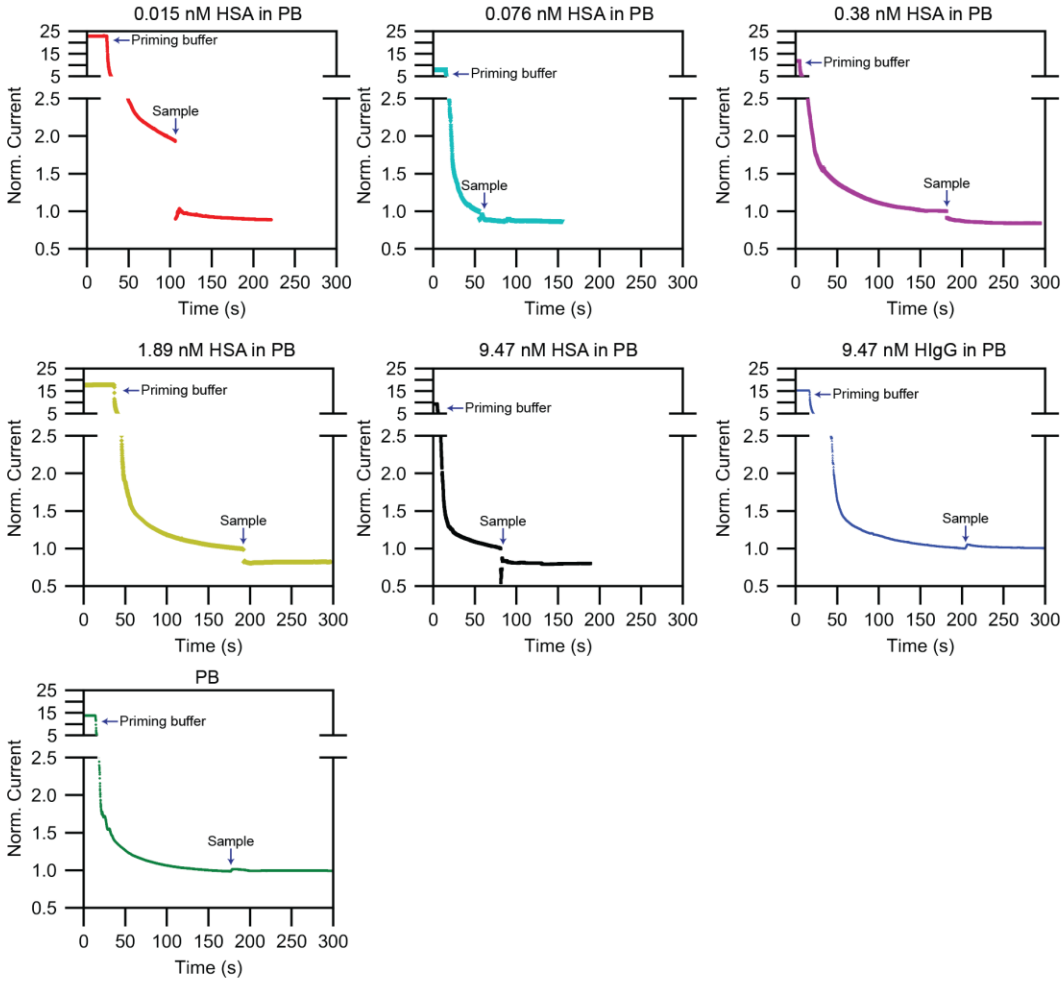

Fig. G2 Normalized current vs. time plots for different concentrations of HSA in PB and controls. Controls consisted of PB with no sample and 9.47 nM HIgG. After a priming buffer was added to the channel, a sample was deposited. The grooves in the channel drove the sample towards the sensor rapidly and distributed it over the surface of the sensor. N=3.

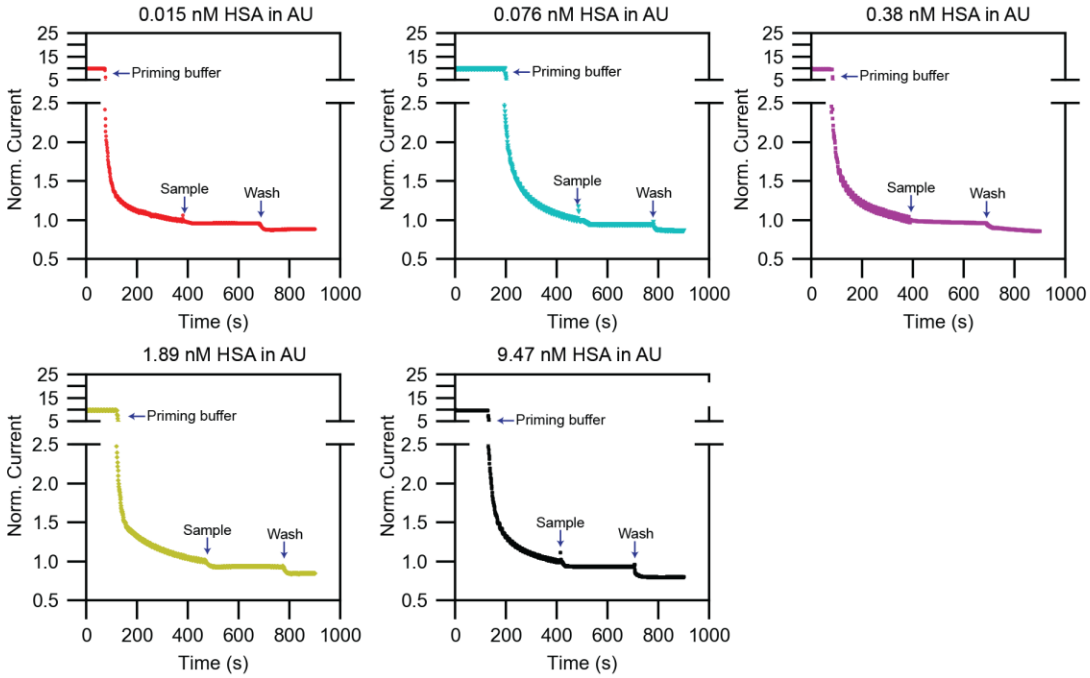

Fig. G3 Normalized current vs. time plots for different concentrations of HSA in artificial urine. After a priming buffer was added to the channel, a sample and wash buffer were deposited. The grooves in the channel drove the sample/wash buffer towards the sensor rapidly and distributed it over the surface of the sensor. The wash buffer is needed to recover sensitivity when using a complex matrix. N=3.

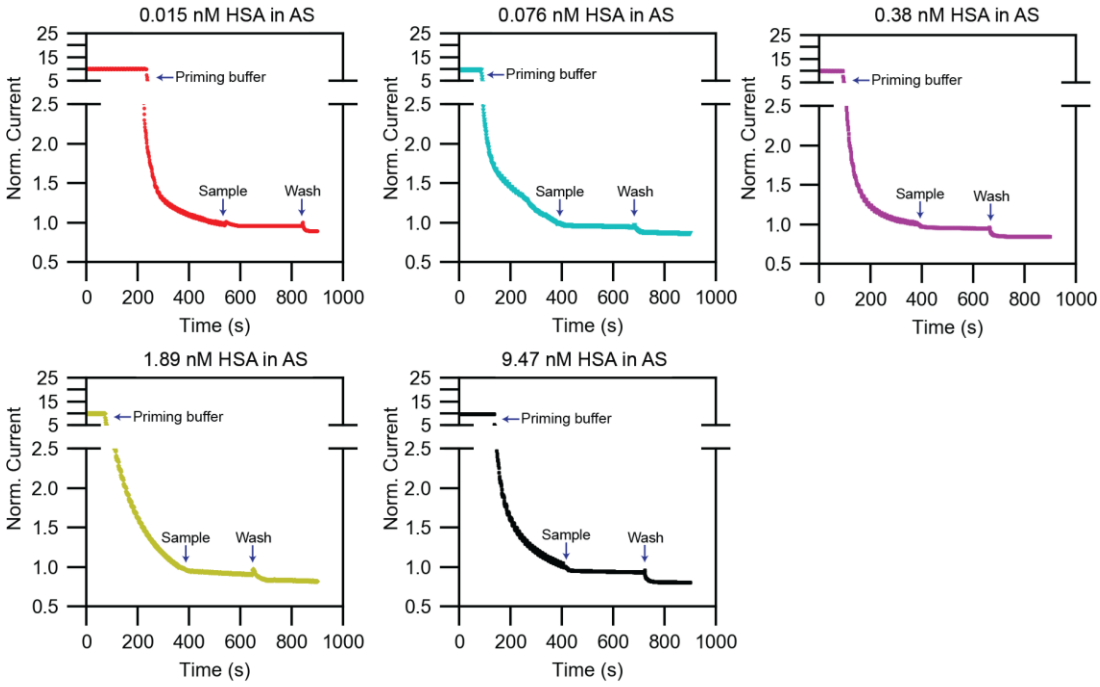

Fig. G4 Normalized current vs. time plots for different concentrations of HSA in artificial saliva. After a priming buffer was added to the channel, a sample and wash buffer were deposited. The grooves in the channel drove the sample/wash buffer towards the sensor rapidly and distributed it over the surface of the sensor. The wash buffer is needed to recover sensitivity when using a complex matrix. N=3.

Appendix H. Time-step derivation for MATLAB simulations

$$\frac{\partial \theta}{\partial t} = \nabla \cdot (D(\theta) \nabla \theta) \quad \text{(eq. H1)}$$

$$D(\theta) = \frac{k(\theta)}{\mu} \frac{\partial P(\theta)}{\partial \theta} \quad \text{(eq. H2)}$$

Define:

$$k(\theta) = k_0 \theta^a \quad \text{(eq. H3)}$$

$$P(\theta) = P_0 \theta^b \quad \text{(eq. H4)}$$

$$\frac{\partial P}{\partial \theta} = P_0 b \theta^{b-1} \quad \text{(eq. H5)}$$

Substitute H3 and H5 into H2:

$$D(\theta) = \frac{k_0 \theta^a}{\mu} P_0 b \theta^{b-1} \quad \text{(eq. H6)}$$

$$D(\theta) = \frac{b P_0 k_0}{\mu} \theta^{a+b-1} \quad \text{(eq. H7)}$$

$$D_0 = \frac{b k_0 P_0}{\mu} \quad \text{(eq. H8)}$$

$$D(\theta) = D_0 \theta^{a+b-1} \quad \text{(eq. H9)}$$

Substitute H9 into H1

$$\frac{\partial \theta}{\partial t} = \nabla \cdot (D_0 \theta^{a+b-1} \nabla \theta) \quad \text{(eq. H10)}$$

Rewrite H10 (assume 1D)

$$\frac{\partial\theta}{\partial t} = \frac{\Delta(D_0\theta^{a+b-1}\frac{\Delta\theta}{\Delta x})}{\Delta x} \qquad \text{(eq. H11)}$$

$$\frac{\partial\theta}{\partial t} = \frac{D_0}{(\Delta x)^2}\Delta(\theta^{a+b-1}\Delta\theta) \qquad \text{(eq. H12)}$$

$$\theta_w = dt\frac{D_0}{(\Delta x)^2}\Delta(\theta^{a+b-1}\Delta\theta) \qquad \text{(eq. H13)}$$

Set coefficient term equal to 1 and solve for dt

$$dt\frac{D_0}{(\Delta x)^2} = 1 \qquad \text{(eq. H15)}$$

$$dt = \frac{(\Delta x)^2}{D_0} \qquad \text{(eq. H14)}$$

Appendix I. Relative position of groove and paper during wicking

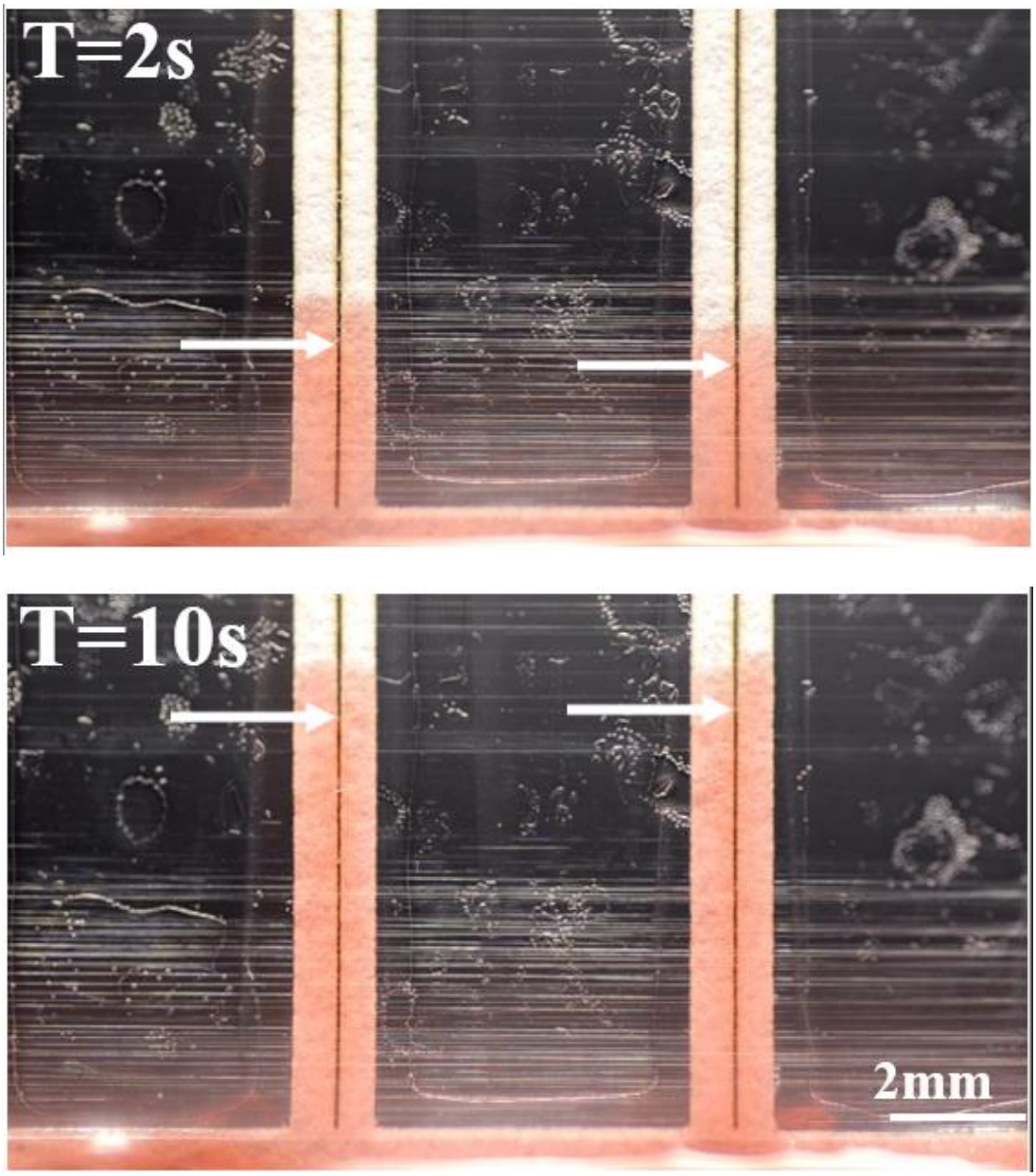

Fig. I1 Comparison of imbibition height in paper and groove during vertical wicking experiments in 20%-speed etched channels (5% Allura Red dye was used for easier visualization). The fluid within the groove lags behind the paper, despite the much higher permeability within the groove. It is suspected that the majority of the fluid within the groove is transferred into the paper, slowing it down.

Appendix J. Final capillary-rise height for fluid inside laser-cut grooves

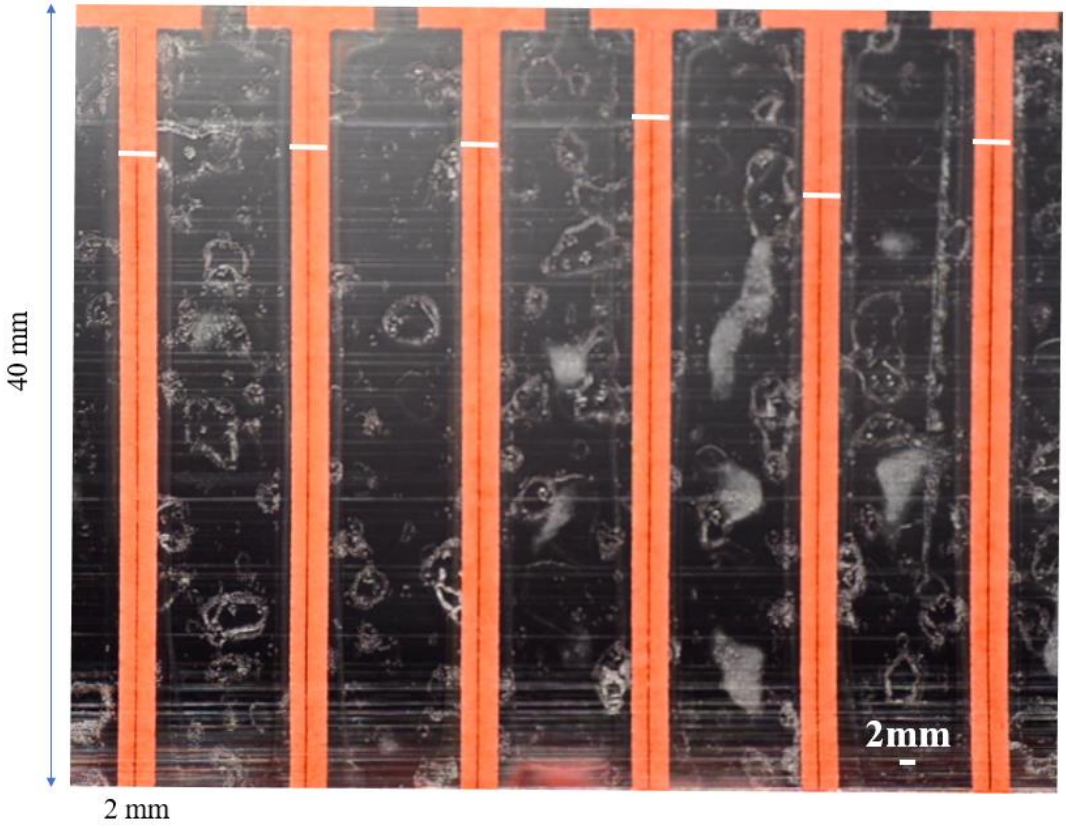

Fig. J1 Final capillary-rise heights for 20%-speed etched paper channels used in vertical wicking experiments (5% Allura Red dye was used for easier visualization). Images were taken ~5 minutes after the wetting front in the paper reached 40mm. It was observed that fluid within the groove did not rise to 40mm. Instead, the meniscus stopped at roughly 35mm.